

AD

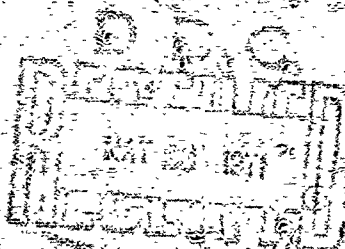
GMRC CR-71-3

## CHARACTERIZATION OF THREE ALUMINUM ALLOYS

JANUARY, 1971

S. G. Schock	T. E. Michaels
J. J. Logan	F. L. Schlegel
D. B. Harvey	S. J. Green

MATERIALS AND STRUCTURES LABORATORY  
MANUFACTURING DEVELOPMENT  
GENERAL MOTORS CORPORATION  
GENERAL MOTORS TECHNICAL CENTER  
Warren, Michigan 48090



FINAL REPORT - CONTRACT DAAG 46-63-C-0127

This document has been approved for public release and sale; its distribution is unlimited.

prepared for  
ARMY MATERIALS AND MECHANICS RESEARCH CENTER  
Watertown, Massachusetts 02172

**Best  
Available  
Copy**

UNCLASSIFIED  
Security Classification

AD 724 195

DOCUMENT CONTROL DATA - R & D

(Security classification of title, body of abstract and indexing annotation must be entered when the overall report is classified)

1. ORIGINATING ACTIVITY (Corporate author) Manufacturing Development, General Motors Corporation, General Motors Technical Center, Warren, Michigan 48093	2a. REPORT SECURITY CLASSIFICATION UNCLASSIFIED
	2b. GROUP ---

3. REPORT TITLE

CHARACTERIZATION OF THREE ALUMINUM ALLOYS

4. DESCRIPTIVE NOTES (Type of report and inclusive dates)

Final Report

5. AUTHOR(S) (First name, middle initial, last name)

S. G. Babcock, J. J. Langan, D. B. Norvey, T. E. Michaels  
F. L. Schierloh and S. J. Green

6. REPORT DATE

January 1971

7a. TOTAL NO. OF PAGES

121

7b. NO. OF REFS

29

8a. CONTRACT OR GRANT NO.

DAAG46-69-C-0127

b. PROJECT NO.

D/A Project ITO 62105 A 331

c.

AMCMS Code 5025.11.297

d.

9a. ORIGINATOR'S REPORT NUMBER(S)

AMMRC CR 71-3

9b. OTHER REPORT NO(S) (Any other numbers that may be assigned this report)

MSL-70-12

10. DISTRIBUTION STATEMENT

This document has been approved for public release and sale; its distribution is unlimited.

11. SUPPLEMENTARY NOTES

---

12. SPONSORING MILITARY ACTIVITY

Army Materials and Mechanics  
Research Center  
Watertown, Massachusetts 02172

13. ABSTRACT

✓ The dynamic behavior of three aluminum alloys; 6061-T6, 2014-T6 and 2024-T3, is described from experimental tests in three areas: (1) Effect of prestraining on the subsequent yield surface in biaxial stress, (2) Effect of heating rate or time-at-temperature on the yield and flow stress behavior in uniaxial stress, and (3) Shock wave response where elastic constants, hugoniot equation of state, wave profiles, and spallation thresholds were determined. Experimental techniques are fully described with emphasis on data interpretation within the limitations of the experiments. Results are presented with analysis and discussion related to current theoretical formulations.

14.	KEY WORDS	LINK A		LINK B		LINK C	
		ROLE	WT	ROLE	WT	ROLE	WT
	Strain Rate Yield Point Spalling Aluminum Alloys Shock Waves Equations of State						

AMMRC 71-3

CHARACTERIZATION OF THREE ALUMINUM ALLOYS

January, 1971

S. G. Babcock	T. E. Michaels
J. J. Langan	F. L. Schierloh
D. B. Norvey	S. J. Green

Materials and Structures Laboratory  
Manufacturing Development  
General Motors Corporation  
General Motors Technical Center  
Warren, Michigan 48090

Final Report - Contract DAAG 46-69-C-0127

D/A Project ITO 62105A331  
AMCMS Code 5025.11.297  
Reduction of Vulnerability: ABM Systems

This document has been approved for public release and sale;  
its distribution is unlimited.

Prepared for

ARMY MATERIALS AND MECHANICS RESEARCH CENTER  
Watertown, Massachusetts 02172

MSL-70-12

## FOREWORD

This report was prepared by the Materials and Structures Laboratory, Manufacturing Development, General Motors Corporation, General Motors Technical Center, Warren, Michigan, under Contract DAAG46-69-C-0127 from the Army Materials and Mechanics Research Center, Watertown, Massachusetts. The work was performed during the period 30 June 1969 to 15 May 1970 and was technically monitored and administered by Mr. J. Dignam and Dr. S. C. Chou of AMMRC.

The objective of this program was to examine the behavior of three aluminum alloys, 2024-T3, 2014-T6, and 6061-T6, in tests related to those needed to evaluate the vulnerability of interceptor missiles by carrying out the following programs:

- TASK A Study the elastic behavior of 2014-T6 aluminum using ultrasonic techniques for temperatures up to 400°F. The effect of pressure up to 8 kilobars was investigated.
- TASK B Study the yield surface of 2024-T3 aluminum by biaxially stressing thin wall tubular specimens. The effect of prestraining on the subsequent yield surface was investigated in conjunction with a contract from the Sandia Laboratories, No. 53-0204.
- TASK C Study the high heating rate properties of 2014-T6 and 6061-T6 aluminum at temperatures up to 700°F. Uniaxial stress tensile tests were conducted after heat up at rates up to  $3 \times 10^3$ °F/second.
- TASK D Hugoniot equations of state and wave profile tests were conducted at room temperature on 2014-T6 aluminum.
- TASK E Spallation threshold measurements on 2014-T6 aluminum were conducted at room temperature.

This report is divided into four sections based on the type of information discussed. Section I discusses the bi-axial subsequent yield study, Section II discusses the high

heating rate results, and Section III discusses the shock wave data including elastic constants, hugoniot and wave profile results, and spallation results. Section IV contains conclusions drawn from the program.

The program was supervised and managed by Mr. S. J. Green. Principal investigators were Mr. S. G. Babcock and Mr. W. M. Isbell while project scientists included Messrs. J. D. Leasia, J. J. Langan, F. L. Schierloh, D. B. Norvey, D. R. Christman and T. E. Michaels.

The authors would like to acknowledge the following individuals for their competent assistance in the fulfillment of this program: Mr. M. C. Klewicki and Mr. L. A. Seltz for their work on the biaxial testing, Mr. J. E. Bonner for his work on the high heating rate testing, and Mr. J. R. Havens and Mr. C. E. Woodcock for their work in the shock wave testing. In addition, special recognition is extended to Dr. Arfon H. Jones for his technical comments and assistance in this program.

MSL-70-12

TABLE OF CONTENTS

	<u>Page</u>
ABSTRACT	iii
FOREWORD	iv
LIST OF ILLUSTRATIONS	vii
INTRODUCTION	1
SECTION I - SUBSEQUENT YIELD SURFACE OF 2024-T3 ALUMINUM	3
SECTION II - HEATING RATE STUDIES OF TWO ALUMINUM ALLOYS, 6061-T6 AND 2014-T6	29
SECTION III - SHOCK PROPAGATION AND FRACTURE CHARACTERISTICS OF 2014-T6 ALUMINUM	53
SECTION IV - CONCLUSIONS	101
APPENDIX A - MATERIAL DESCRIPTION	104
REFERENCES	109
DISTRIBUTION LIST	112
ABSTRACT CARDS	117
DD FORM 1473, DOCUMENT CONTROL DATA - R&D	121



## LIST OF ILLUSTRATIONS

<u>Figure</u>		<u>Page</u>
1	GM Biaxial Strain-Rate Machine	4
2	Schematic Diagram of GM Biaxial Strain-Rate Machine	5
3	Sectional View of Specimen Package for Axial Tension and Circumferential Tension	8
4	Sectional View of Specimen Package for Axial Compression and Circumferential Tension	9
5	Photograph of a Test Package for Metal Specimens	10
6	Block Diagram of Data Measurement and Reduction for Biaxial Machine	13
7	Second, Third, and Fourth (see text) Stress Quadrant Specimens on the Left, First Quadrant Specimen to the Right	15
8	Yield Surface for 2024-T3 Aluminum in As-Received Condition (Virgin)	19
9	Yield Surface for 2024-T3 Aluminum Pre-Strained by 8% Axial Compression	20
10	$\pi$ -Plane Yield Surface for 2024-T3 Aluminum in As-Received Condition (Virgin)	21
11	Comparison of Hardening Laws, or Subsequent Yield Theories	23
12	Illustrations of Cross-Effects and the Bauschinger Effect	24
13	Comparison of Virgin and Prestrained Yield Surfaces	27
14	Schematic of Ultra-High Temperature Strain-Rate Machine	30

MSL-70-12

## LIST OF ILLUSTRATIONS (Continued)

<u>Figure</u>		<u>Page</u>
15	Test Specimens and Grip Details	33
16	Standard Deviation Coefficient, C, as a Function of Number of Samples and Desired Confidence Interval	37
17	2014-T6 Aluminum Alloy, Average Stress- Strain Behavior at Various Heating Rates	39
18	2014-T6 Aluminum Alloy, Yield Stress vs. Heating Rates at Various Tempera- tures	40
19	2014-T6 Aluminum Alloy, Ultimate Stress vs. Heating Rates at Various Tempera- tures	41
20	6061-T6 Aluminum Alloy, Yield Stress vs. Heating Rates at Various Tempera- tures	42
21	6061-T6 Aluminum Alloy, Ultimate Stress vs. Heating Rates at Various Tempera- tures	43
22	Elongation to Fracture vs. Heating Rate for 2014-T6 and 6061-T6 Aluminum	44
23	Artificial Aging Characteristics of 2014 and 6061 Aluminum Alloys Sub- sequent to Solution Hardening (Reference 15)	46
24	Normalized Yield Stress vs. Test Tem- perature for 6061-T6 Aluminum After Various Times at Temperature	47
25	Normalized Yield Stress vs. Test Tempera- ture for 2014-T6 Aluminum After Various Times at Temperature	48

## LIST OF ILLUSTRATIONS (Continued)

<u>Figure</u>		<u>Page</u>
26	Metallography Study of 6061-T6 Aluminum	51
27	Metallography Study of 2014-T6 Aluminum	52
28	Pulse Superposition Technique Schematic	56
29	Static High-Pressure Apparatus Schematic	57
30	63.5 mm Compressed Gas Gun Schematic	58
31	Room Temperature Spall Test Schematic	59
32	Schematic of Direct Impact Technique	60
33	Schematic of Buffered Direct Impact Technique	61
34	102 mm Compressed Gas Gun Schematic	62
35	Laser Velocity Interferometer Schematic	64
36	Projectile and Velocity Interferometer Target	65
37	Stress Inputs for Wave Profile Studies	66
38	Schematic of Spall Wave Profile Shots	67
39	Isotherm, Adiabatic and Shock Hydrostat Calculated for 2014-T6 Aluminum	74
40	Metallographs of Spall Fracture in 2014-T6 Aluminum, 0.6 mm Impactor	76
41	Metallography of Spall Fractures in 2014-T6 Aluminum, 1.6 mm Impactor	77
42	Spall Results for 2014-T6 Aluminum	78
43	Results from Direct Impact Shots	79
44	Results from Buffered Direct Impact Shots	80

MSL-70-12

## LIST OF ILLUSTRATIONS (Continued)

<u>Figure</u>		<u>Page</u>
45	Hugoniot of 2014-T6 Aluminum to 50 Kilobars	84
46	Wave Profiles in 2014-T6 Aluminum at a Propagation Distance of $\sim 3$ mm (Fused Quartz Impactors)	86
47	Wave Profiles in 2014-T6 Aluminum for an Average Impact Velocity of 0.284 mm/ $\mu$ sec and Propagation Distances of $\sim 1, 3, 6.5,$ and 12 mm (Fused Quartz Impactors)	87
48	Compressive and Rarefaction Waves Characteristics for a Peak Stress of 20 Kilobars and $\sim 1.5$ mm (Fused Quartz Impactor)	88
49	Wave Profiles in 2014-T6 Aluminum for a Propagation Distance of $\sim 3$ mm and Two Peak Stress Levels (Tungsten Carbide Impactors)	90
50	Elastic Precursor Decay in 2014-T6 Aluminum for a 20 Kilobar Impact Stress	91
51	Wave Interactions at Spall Plane and Resultant Velocity-Time and Stress-Time Histories at Free Rear Surface	92
52	Spall Wave Profiles for 0.6 mm Impactor Series	93
53	Spall Wave Profiles for 1.6 mm Impactor Series	94
54	Hugoniot Hydrostats Calculated for 2014-T6 and 6061-T6 Aluminum Using Eqs. (III-19), (III-20), (III-21), and (III-22) (29)	97
55	Spallation Threshold Results for 2014-T6 Aluminum Compared to 6061-T6 Aluminum (28)	98
56	Hugoniot for 2014-T6 Aluminum Compared to Hugoniot for 6061-T6 Aluminum (29)	99

MSL-70-12

## LIST OF ILLUSTRATION IN APPENDIX

<u>Figure</u>		<u>Page</u>
A-1	Photomicrograph of 6061-T651 Aluminum 0.25 Inch Rod Specimen Material	105
A-2	Photomicrograph of 2024-T351 Aluminum 3.0 Inch Rod Specimen Material	106
A-3	Photomicrograph of 2014-T651 Aluminum 0.5 Inch Plate Specimen Material	107

## LIST OF TABLES

<u>Table</u>		<u>Page</u>
I	Student t Distribution	35
II	Results of Ultrasonic Measurements on 2014-T6 Aluminum	69
III	Elastic Constants for 2014-T6 Al (P = 0, T = 25°C)	72
IV	Spall Results for 2014-T6 Aluminum	75
V	Hugoniot Data for 2014-T6 Aluminum	82
VI	Summary of Elastic Precursor Amplitudes	91
VII	Comparison of Elastic Constants for 2014-T6 and 6061-T6 Aluminum	96
VIII	Comparison of Precursor Amplitude for 2014-T6 and 6061-T6 Aluminum at ~ 20 Kilobars Impact Stress (29)	100

## TABLE LISTING IN APPENDIX

	<u>Page</u>
A-I Chemical Composition	108

MSL-70-12

## INTRODUCTION

In the vulnerability assessment of reentry and interceptor vehicles, the response of the vehicle materials and structure to stress wave and momentum loading must be determined. An analysis of stress wave propagation is carried out first to determine the kinetic energy distribution among the fractured, spalled, and/or debonded materials in the structure. Following this is an analysis of loading on the structure due to the momentum imparted by the stress wave interaction. Computer codes are used to assist in the mathematical simulation of these responses, and laboratory or underground tests are employed to check the validity of the computations.

Inputs to these codes require material properties in the form of constitutive equations derived from controlled laboratory experiments. This program was directed towards determining the material properties required in the computer codes mentioned above. Four areas of experimental work were covered. Three areas, elastic property measurements using ultrasonic techniques, shock wave experiments to determine hugoniot equation of state, complete wave profiles and spallation thresholds, as well as subsequent yield surface determination are familiar to investigators and have been used in past studies. One area, high heating rate response, was not well developed prior to the beginning of this program, and techniques had to be developed to the stage of obtaining valid data on the materials of interest.

Section I deals with the determination of the virgin and subsequent yield surfaces of 2024-T3 aluminum, as determined by quasi-static biaxial stress tests yielding data in the four quadrants of the axial stress-circumferential stress plane. The General

MSL-70-12

Motors Biaxial Strain-Rate Machine is described, along with the corresponding variable input and data reduction operations. Specimen configurations are detailed, and the prestraining process for the subsequent yield specimens is outlined. Following the data presentation is a short discussion of the literature and a comparison, which leads to the conclusions for the section.

Section II describes the technique developed to study the heating rate and/or time-at-temperature behavior of two aluminum alloys: 6061-T6 and 2014-T6. Temperatures up to 700°F were attained using a direct resistance heating technique at heating rates up to  $2.5 \times 10^3$  °F/second. Constant strain rate ( $\sim 10$ /sec) uniaxial stress tensile tests were conducted to determine yield and ultimate strengths at various test temperatures and heating rates.

Section III describes the results of measurements made on 2014-T6 aluminum to determine the elastic constants up to 400°F and 8 kilobars pressure. Ultrasonic techniques were employed to gather this information. In addition, room temperature hugoniot equation of state and several complete wave profile measurements were made and the spallation threshold was determined.

Section IV contains the conclusions drawn from these areas of study. An Appendix is provided to describe the physical and chemical makeup of the three aluminum alloys.

## SECTION I

SUBSEQUENT YIELD SURFACE OF  
2024-T3 ALUMINUM

## INTRODUCTION

The effect of previous loading history on a material's subsequent behavior has been a subject of great interest. In this study the General Motors Biaxial Machine, a unique dynamic loading apparatus, was employed in obtaining the virgin and subsequent yield surfaces of 2024-T3 aluminum. The subsequent yield data was gathered following the application of an 8% axial compressive strain to the material. A description of the machine, specimens, and data handling techniques are included in this section. The data itself is reviewed in regard to the effect of the prestraining on the behavior of the yield surface.

## BIAXIAL TESTING TECHNIQUE

The General Motors Biaxial Strain-Rate Machine,<sup>(1)</sup> pictured in Figure 1 and shown schematically in Figure 2, develops a biaxial state of stress by independently applying an axial load and a circumferential load (by fluid pressure) on a tubular specimen through two independent gas-operated cylinders. Strain rates from  $10^{-4}$  to  $10^2$ /sec are obtainable and may be held constant within a factor of two for the elastic range with a slightly higher variation for plastic strains.



MSL-70-12

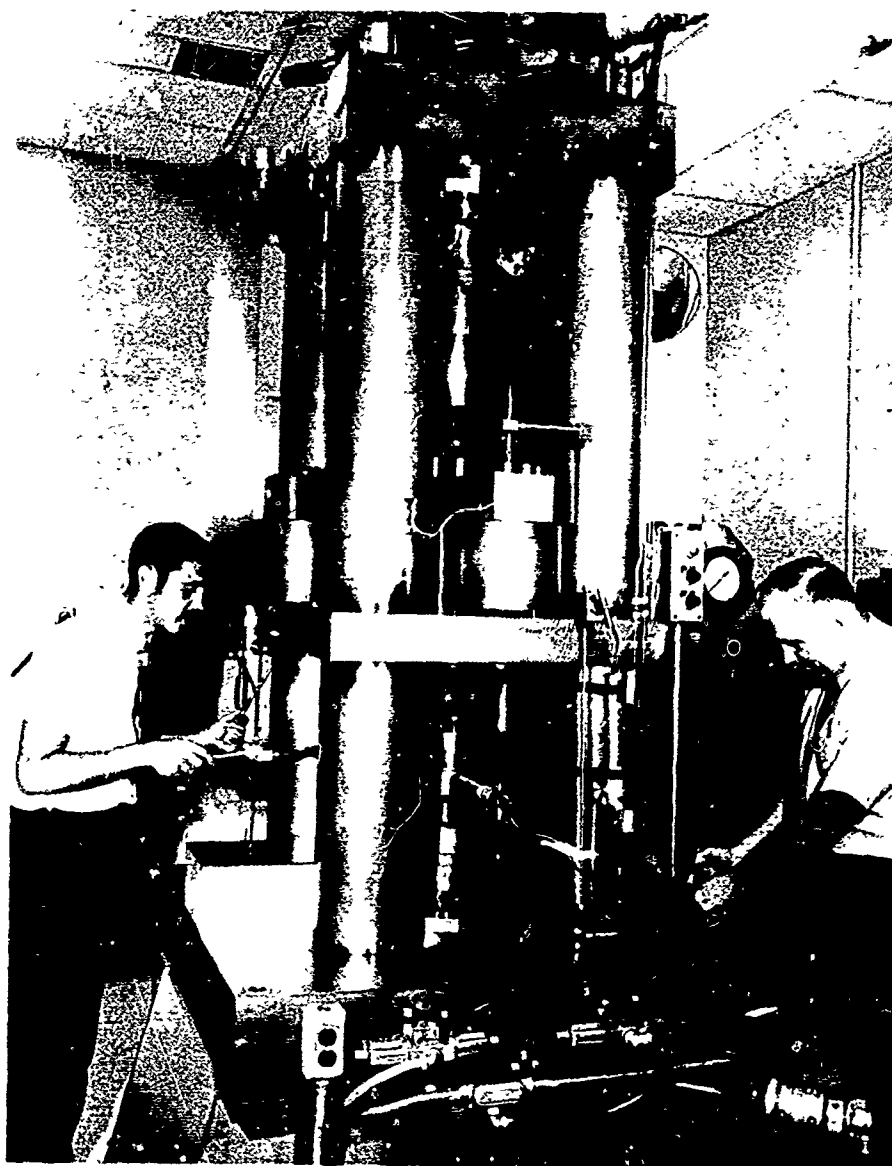


Figure 1 GM Biaxial Strain-Rate Machine

MSL-70-12

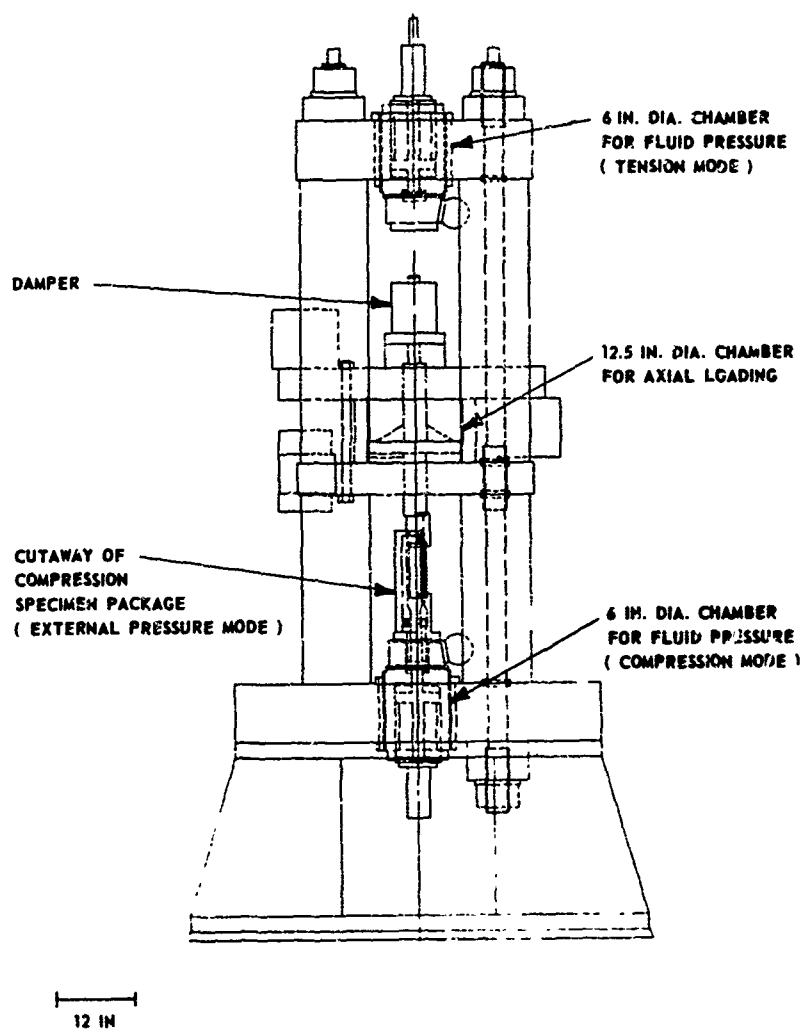


Figure 2 Schematic Diagram of GM Biaxial Strain-Rate Machine

MSL-70-12

Axial load to the specimen is provided by a 12.5 inch bore cylinder with a piston constructed of titanium, for high strength-to-mass ratio, and designed to operate in one direction only. The piston is braced between the stem and the flange to increase its stiffness, the stem being hollow to allow a means of egress for instrumentation cables. Because of the unidirectional movement of the piston, the axial compression is obtained on the lower end of the piston and axial tension on the upper end. Either end of the piston rod may be attached to the specimen for axial loading, with a variable hydraulic damper assembly connected on the other end to damp undesirable piston oscillations.

A six inch bore cylinder is used to load an auxiliary piston which, in turn, pressurizes a fluid for circumferential loading of the specimen. The specimen is pressurized internally for circumferential tension, and externally for circumferential compression. The six inch pistons are not braced and may be operated in either direction. However, because of the unidirectional nature of the axial loading piston, two six inch cylinder assemblies are utilized, one for circumferential loading during axial tension (upper half) and one for circumferential loading during axial compression (lower half).

Fast acting valves are connected to the front reservoir of each cylinder to provide a means of evacuating the reservoir in minimum time. Between the reservoir and the fast acting valve is an interchangeable orifice plate which meters the flow of gas from the front reservoir, and thus acts as the primary control of the piston velocity.

The machine frame is designed to resist separating forces of  $400 \times 10^3$  lbs. by using prestressed column tie-rod construction.

MSL-70-12

The construction is essentially that of two frames with a common middle plate. As only one end of the machine is used at a time, threading the tie rods through the middle plate allows each end of the tie rod to be stressed separately. Calculations show deflections of the order of 0.002 inch under maximum loading ( $340 \times 10^3$  lbs.).

Specimen packages were designed and constructed for biaxially testing tubular specimens in each of the four stress quadrants in the circumferential stress--axial stress plane. A package serves to support and seal the tubular specimen, to provide a closed pressure chamber, and to provide support for pressure transducers and strain gage seals. Each package consists of a piston rod adapter, load cell, tubular specimen with adapter, base, ring piston, actuating pins, base plug, and pressure transducer.

Figures 3 and 4 show cross sections through two packages, which differ primarily in the means of gripping the specimen due to the nature of loading. The package in Figure 4 is photographed in Figure 5. Both of these packages are for circumferential tension and thus show a core rod through the center which serves to align the assembly and reduce the volume of pressurizing fluid required to stress the specimen. Reduction of fluid volume reduces allowable fluid compressibility, thereby reducing oil piston stroke requirements. The housing to contain the fluid in the circumferential compression package serves the same purpose as the core rod. Note that the nose of the ring piston has a land that cushions the end of its stroke by metering fluid flow between the base and the core rod. The metering arrangement reduces the possibility of catastrophic piston impact if premature failure of the specimen occurs during a test.

MSL-70-12

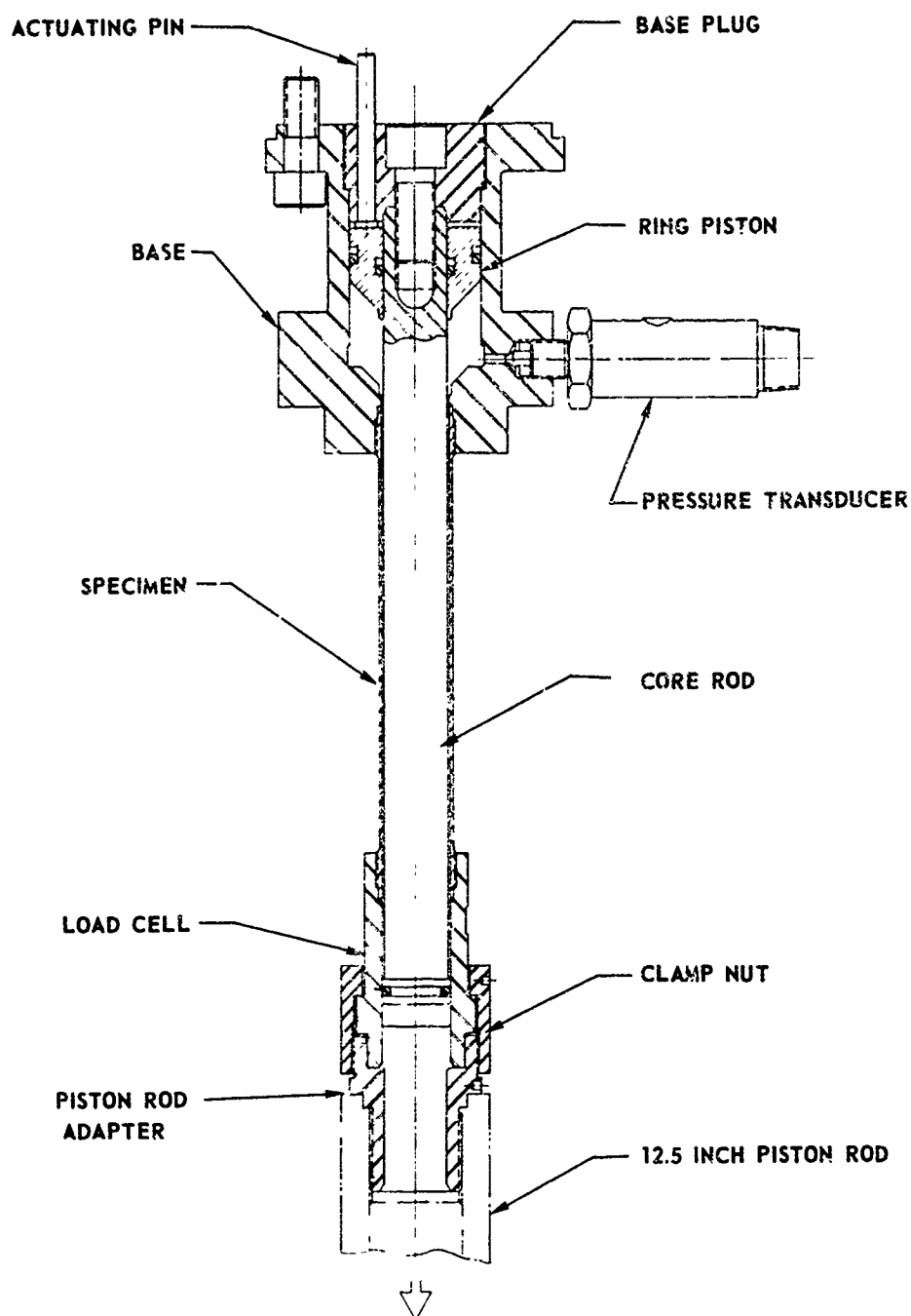


Figure 3 Sectional View of Specimen Package for Axial Tension and Circumferential Tension

MSL-70-12

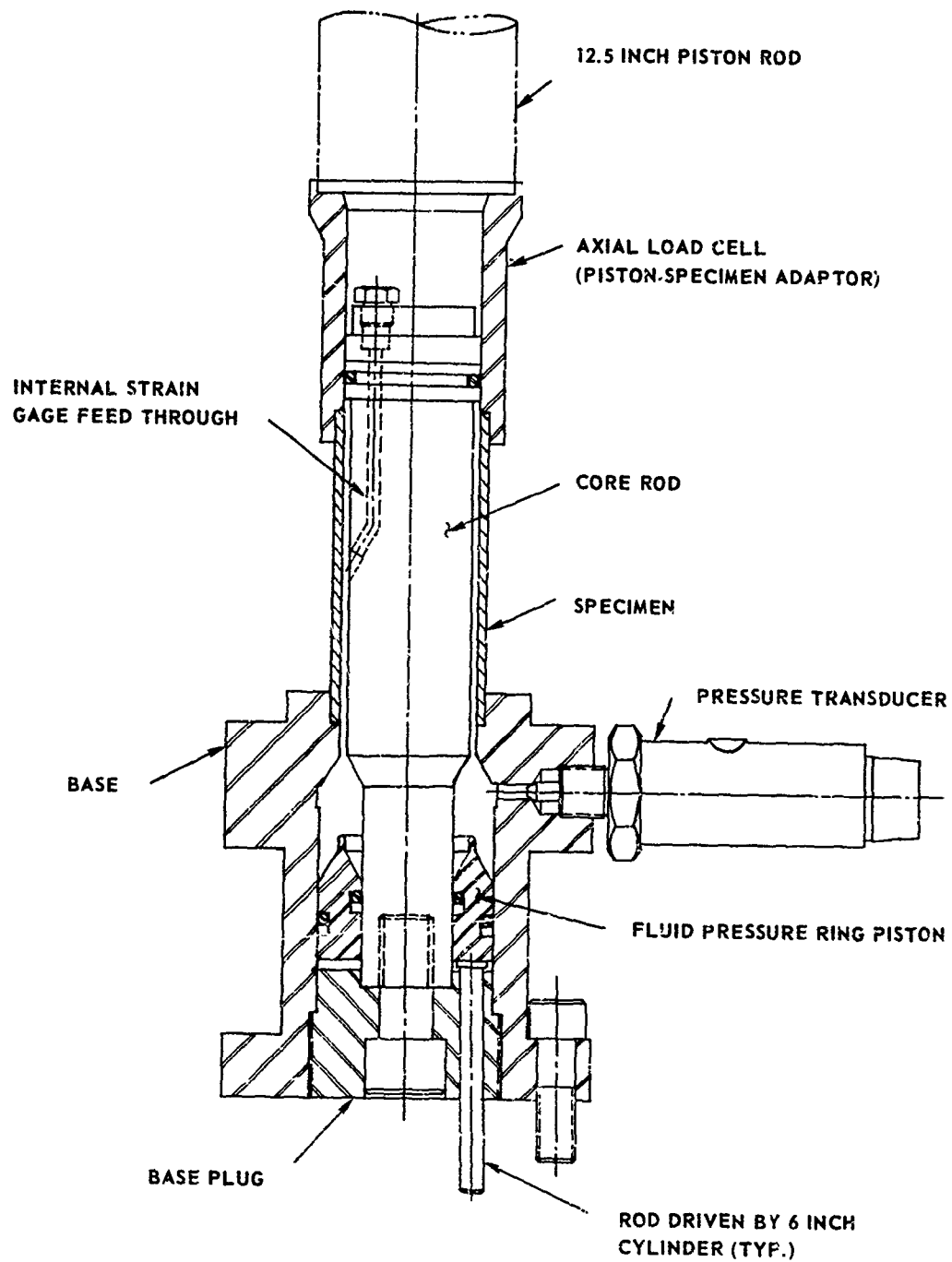


Figure 4 Sectional View of Specimen Package for Axial Compression and Circumferential Tension

MSL-70-12

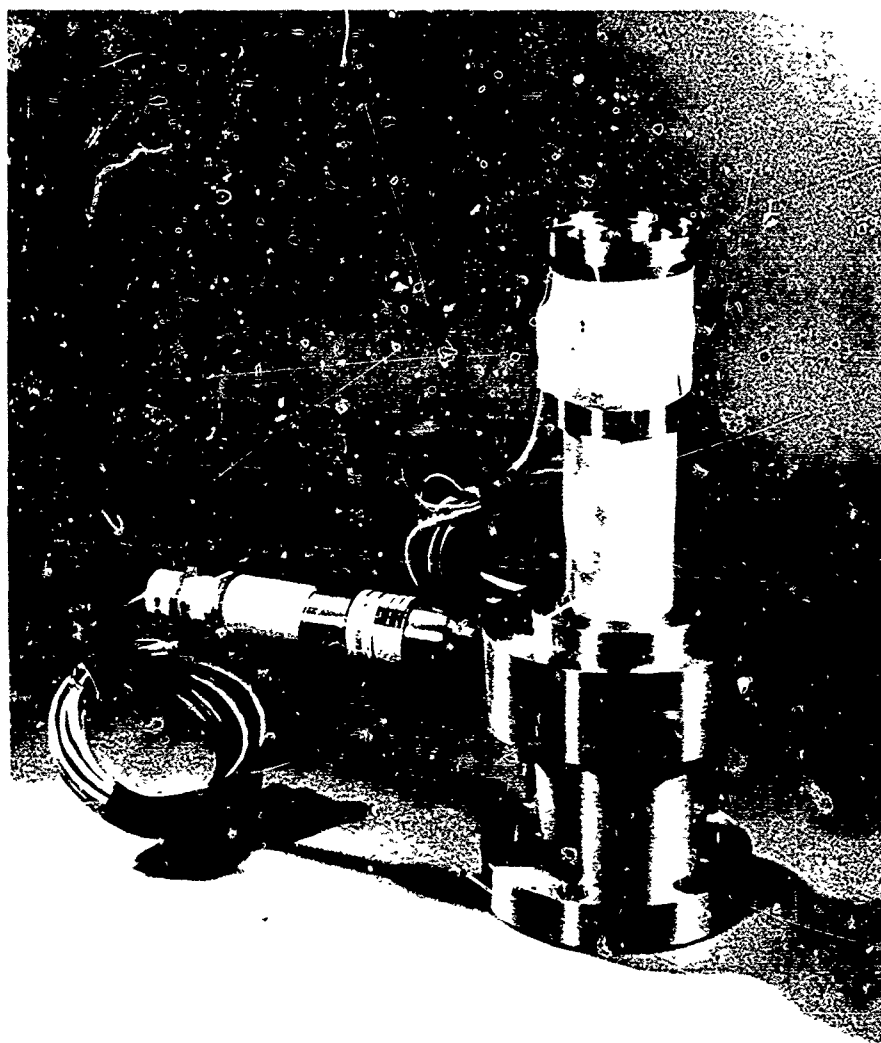


Figure 5 Photograph of a Test Package for Metal Specimens

The machine is operated by charging each cylinder with gas (air, nitrogen, or helium) introduced at equal pressure into a large reservoir in back of the piston and into a small reservoir in front of the piston. The piston moves forward when the small reservoir is exhausted by flow through an orifice. Exhaust is initiated through the opening of the downstream fast acting valve. Piston velocity, and hence the rate of loading, is controlled by the type of pressure of the working gas, the orifice size, and to some extent, the specimen.

A computer program of the piston motion, described in detail in Reference 1, is used to determine the initial conditions of the driving gas, the gas pressure required, orifice size, and amount of viscous damping necessary to biaxially load a specimen at a predetermined stress ratio. Briefly, the procedure is as follows. Uniaxial stress data for the specimen material is used to produce an effective stress-strain curve (from the octahedral stress-strain relations) for the material, with the uniaxial stress tensile and compressive fracture stresses as boundary conditions, if appropriate. Through a short iteration program the individual stress-strain data for a given stress ratio are obtained for each direction of loading. The equations of continuous curves fitted to these data are used in the specimen reaction calculations in the piston motion study.<sup>(1)</sup> In this program, the input parameters of gas pressure, orifice size, and damping coefficients are iterated upon until the desired constant strain rate is obtained. These final parameters are then the machine settings used in the actual experiment. Through this programming, efficient use is made of machine time and specimens by virtually eliminating trial and error adjustment in the system.



MSL-70-12

Upon firing, the test specimen tube is subjected to axial load by displacement of the main piston rod of the Biaxial Machine. Displacement of the six inch cylinder piston rods exerts a force on the actuating pins of the package, and these in turn drive the ring piston in the package which compresses the fluid in the oil chamber. The pressurized fluid develops the circumferential stresses in the tubular walls.

Instrumentation for the Biaxial Machine consists of an axial load cell and a pressure transducer for loading measurement, and axially and circumferentially oriented strain gages to record the strain on both the inside and outside surfaces of the specimen. The output from each transducer is continuously monitored in analog form on a fourteen channel, wide band (400 KHz), frequency modulated tape recorder. Between the tape recorder and the transducer is a system of bridge and balance units, signal amplifiers and shunt calibration resistors.

An IBM 1800 computer is used as a central processor to reduce the measured data after it has been converted from analog to digital form. This conversion technique, coupled directly to the computer, omits all intermediate steps required for manual digitizing, reducing the cumulative system error to approximately  $\pm 0.5\%$  of full scale. The particular processor used has a  $16 \times 10^3$ , sixteen bit word storage as well as an associated  $10^6$  word two disk storage unit. This flexible system, shown schematically in Figure 6, has the capability to digitize, store, manipulate with the proper scale factors, print and plot the various reduced data. More complete details are presented in References 1 and 2.

MSL-70-12

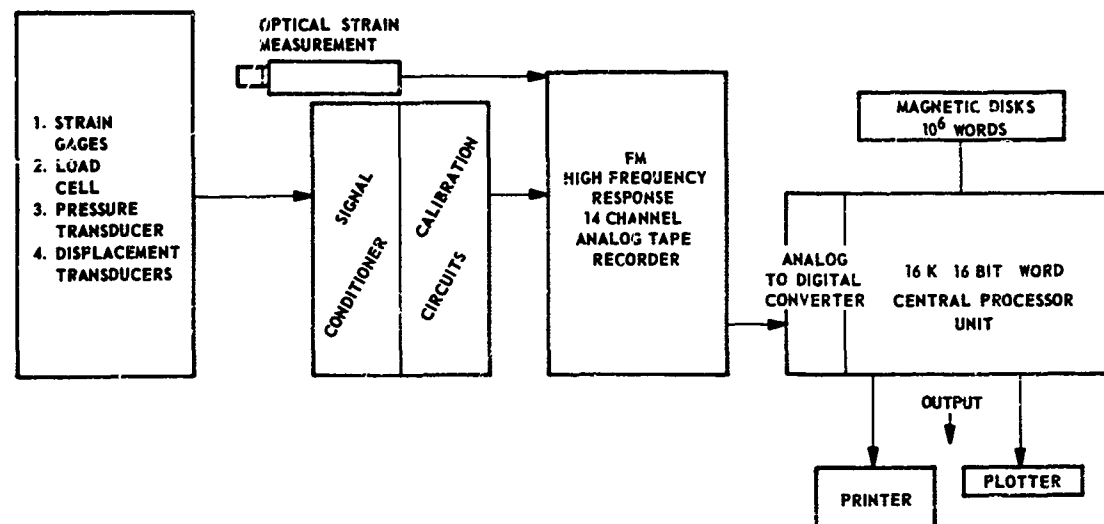


Figure 6 Block Diagram of Data Measurement and Reduction for Biaxial Machine

#### SPECIMENS

All specimens reported were machined from three inch rod stock 2024-T3 aluminum obtained from the same mill run. A complete description of the material appears in Appendix A. Separate specimen configurations were used for obtaining data in each of the four stress quadrants. The same configurations, however, were used for both the virgin and pretrained material in each quadrant, with the exception of the first, or tension-tension, quadrant where shorter specimens were used for the pretrained material. In machining all specimens, diameters were held to within  $\pm 0.0005$  inch, concentricity of inside outside diameter was held to 0.001 T.I.R., and the lengths were held to within 0.03 inch with parallel ends.

For the virgin material in the tension-tension quadrant, the specimens were 10.5 inches in length, with a 1.5 inch I.D. and

MSL-70-12

a wall thickness of 0.050 inches. The ends were threaded externally to provide a grip for transmitting the axial load. This left an effective gauge length of approximately seven inches. To avoid column buckling in the compressive prestrain, an explanation of which follows, billets 9.250 inches in length had to be used, necessitating a shorter specimen of 8.0 inches in length with a 5.0 inch effective gauge length. All specimens for the second, or axial compression-circumferential tension quadrant, were 2.5 inch O.D., 2.25 inch I.D. tubes 5.0 inches in length. No threads were necessary due to the compressive axial load. The same specimen dimensions are used for the compression-compression or third quadrant. The size of the fourth quadrant specimen was the same; however, this specimen was threaded internally to provide an axial grip, and then had the outer diameter reduced to 2.4 inches over a central 3 inch section of the cylinder to reduce the strength requirements on the threaded ends. Figure 7 shows two of the specimens, both tension-tension and compression-tension, to add visual representation to the above discussion.

Additional tests were made using an Instron uniaxial testing machine to define the yield surface intercepts on the axes of the stress plane. For the axial stress axis the specimens were cut parallel to the axis of the aluminum rod, while for the radial stress axis the specimens were cut in the transverse direction, perpendicular to the rod's longitudinal axis. Compression tests were made using a specimen 0.375 inches in diameter and 0.50 inches in length. Threaded specimens with an overall length of 2.625 inches, gauge diameter of 0.25 inches, and a gauge length of 1.0 inches were used for tensile tests.

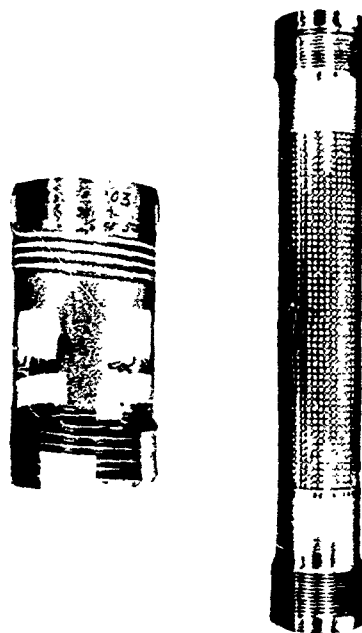


Figure 7 Second, Third, and Fourth (see text)  
Stress Quadrant Specimens on the Left,  
First Quadrant Specimen to the Right

All prestraining of the specimens was done by upsetting billets cut from the 3.0 inch diameter rod in a 2000 ton mechanical press equipped with parallel flat platens. "Barreling" of the specimens was minimized by coating the platens with a Teflon based metalworking lubricant. Variation of diameter along the billet axis did not exceed 0.015 inch with the maximum variation occurring near the ends, which were subsequently removed during machining. For the second, third, and fourth quadrant prestrained specimens, 6.0 inch long billets were given an axial compressive prestrain of 8.2% by subjecting the ends to an axial load of 225 tons. Billets 9.25 inches in length were compressed to 8.5 inches to give an axial compressive strain of 8.1% for the pre-strain specimens used in the tension-tension quadrant. Following the upsetting process, specimens were machined according to the configurations previously outlined.

MSL-70-12

## DATA REDUCTION AND RESULTS

The tubular specimens with  $d/t < 20$  were strain gauged on the inner and outer surfaces with  $90^\circ$  rosettes to measure both axial and circumferential strains. Tubes having  $d/t \geq 20$ , those used in the tension-tension quadrant, were gauged on the outside surface only, because variation of strains through the thickness is small. Data was recorded from the strain gauges, the calibrated axial load cell, and the fluid pressure monitoring transducer. These data were later played back through the analog to digital converter into the computer.

A complete description of the data analysis technique is given in Reference 3, however, a short synopsis follows here. The data interpretation is based on the assumptions of homogeneous materials following conventional elasticity and plasticity. The subscripts a, t, and r refer to axial, circumferential, and radial respectively; all stresses are true stress values, and all strains are natural or logarithmic strains which are given by:

$$\begin{aligned}\epsilon &= \ln(e + 1) & e &= \text{engineering strain} \\ \epsilon &= \text{natural strain} & & \text{(I-1)}\end{aligned}$$

For  $d/t \geq 20$ , thin walled tube equilibrium relations were used to obtain  $\sigma_t$ , with  $\sigma_a$  being calculated as  $F/A$  (force/instantaneous area). In the case of  $d/t < 20$ , variation in the stresses through the thickness need be considered and Lamé's elasticity relations were used to calculate  $\sigma_r$  and  $\sigma_t$ . A discussion of the error involved in calculating stresses is given in Reference 3. The stresses were used to calculate the octahedral shear stress, which is:

MSL-70-12

$$\tau_o = 1/3 \sqrt{(\sigma_a - \sigma_t)^2 + (\sigma_t - \sigma_r)^2 + (\sigma_r - \sigma_a)^2} \quad (I-2)$$

For the thicker walled cylinders,  $d/t < 20$ , the radial strain at a given radius,  $r$ , was computed as:

$$\epsilon_r = \epsilon_o + \frac{2(\epsilon_{t_i} - \epsilon_{t_o}) r_o^2 r_i^2}{r^2(r_i^2 - r_o^2)} \quad \begin{array}{l} i = \text{inner radius values} \\ o = \text{outer radius values} \end{array} \quad (I-3)$$

which is strictly an elastic calculation, although it is a good approximation (errors of about 10%)<sup>(3)</sup> when extended into the plastic region for a few percent plastic strain. On the thin walled specimens, where  $\epsilon_t$  and  $\epsilon_a$  were not measured on the inside surface,  $\epsilon_r$  was calculated from:

$$\epsilon_r = \frac{1-2\nu}{E} (\sigma_a + \sigma_t + \sigma_r) - (\epsilon_t + \epsilon_a) \quad (I-4)$$

where  $\nu$  = Poisson's Ratio

$E$  = Young's Modulus

This relationship assumes that:

- (A) The strains are separable into elastic and plastic parts.
- (B) The sum of the plastic strains is zero.
- (C) Elastic strains are given by Hooke's law.
- (D) Strains and displacements are small.

MSL-70-12

The strains were used to calculate octahedral shear strain, which in terms of the principal normal strain is:

$$\gamma_o = 2/3 \sqrt{(\epsilon_a - \epsilon_t)^2 + (\epsilon_t - \epsilon_r)^2 + (\epsilon_r - \epsilon_a)^2} \quad (I-5)$$

The pressures, loads, stresses and strains were plotted out automatically after computation, with the variables as the ordinate and time as the abscissa. In addition, plots were made of one variable against another. The yield surface was generated by the use of an offset technique on the octahedral shear stress-shear strain plot. Yield was defined as the intercept on the stress-strain curve of a straight line, offset on the strain axis at 0.25% strain (equivalent to a 0.2% strain on a uniaxial test), and drawn parallel to the linear portion of the curve. On the octahedral curves, the slope of this elastic portion is equal to the shear modulus,  $G$ , defined as:

$$G = E/[2(1 + \nu)] \quad (I-6)$$

$$\tau_o = G\gamma_o \text{ in the elastic range.} \quad (I-7)$$

The shear stress value determined in this manner was referred to the shear stress vs. time plot to find the time of yielding. This time was then used to find the value of all other variables at yield.

Plots were made of the circumferential stress vs. the axial stress to determine the yield locus. A least squares, elliptical fit of the data was made and the results are shown in Figure 8 for the virgin material and in Figure 9 for the prestrained aluminum. Note that the virgin data ellipse closely approximates

MEL-70-12

$A_3$  would equal a negative one, the von Mises yield criterion, where  $A_1$  and  $A_2$  would equal one,  $A_3$  would be a negative one,  $A_4$  and  $A_5$  would be zero and  $A_6$  would equal a negative  $Y^2$ , where  $Y$  is yield. The two constants  $A_4$  and  $A_5$  differ most from the von Mises criterion, which has the effect of translating the ellipse center slightly away from the origin. For the pre-strained data, the constants differ significantly from von Mises, particularly  $A_3$ , which changes the elliptical shape, and  $A_4$  and  $A_5$ , which translate the ellipse. This is to be expected as pre-straining produces anisotropy in aluminum. All data points represent quasistatic behavior, the testing having been carried out at strain rates approximately  $10^{-4}$ /second. Figure 8 and 9 will be discussed subsequently.

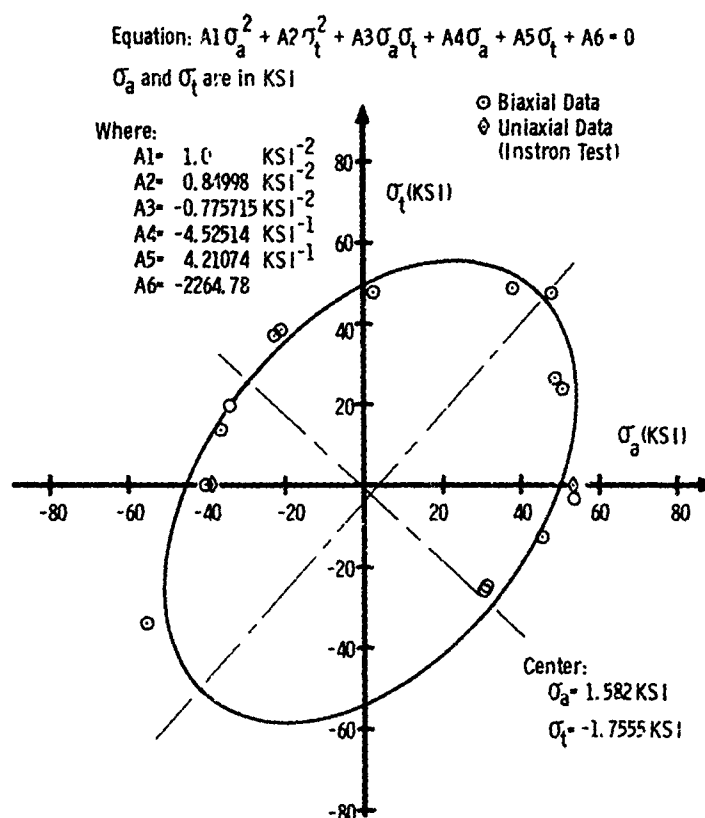


Figure 8 Yield Surface for 2024-T3 Aluminum in As-Received Condition (Virgin)



MSL-70-12

$$\text{Equation: } A1\sigma_a^2 + A2\sigma_t^2 + A3\sigma_a\sigma_t + A4\sigma_a + A5\sigma_t + A6 = 0$$

$\sigma_a$  and  $\sigma_t$  are in KSI

Where:

$A1 = 1.0 \text{ KSI}^{-2}$   
 $A2 = 1.20065 \text{ KSI}^{-2}$   
 $A3 = -0.46547 \text{ KSI}^{-1}$   
 $A4 = 24.3366 \text{ KSI}^{-1}$   
 $A5 = -15.4228 \text{ KSI}^{-1}$   
 $A6 = -3755.01$

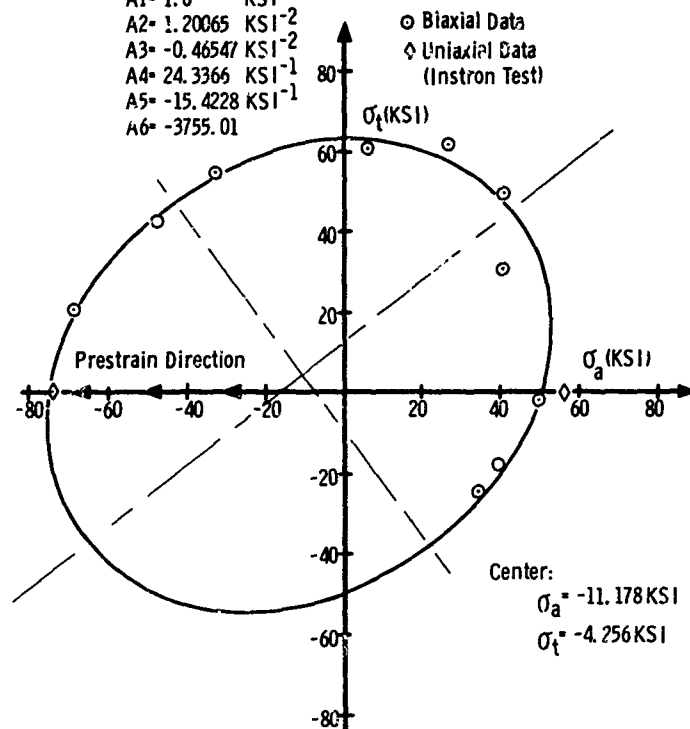


Figure 9 Yield Surface for 2024-T3 Aluminum  
Pre-Strained by 8% Axial Compression

To incorporate radial stresses, which are an order of magnitude lower than the others, plots are made on the  $\pi$  plane, or the plane showing the deviatoric components of stress only. For isotropic materials following the von Mises yield criterion, the three dimensional yield surface is a cylinder, and all yield points, regardless of the hydrostatic component of stress, project back onto the  $\pi$  plane in a circle, its center being at the origin of the three Cartesian stress coordinates. Since the virgin yield data does not vary significantly from the von Mises criterion, a circle has been fit to the data, as

MSL-70-12

shown in Figure 10. In the case of an anisotropic material, the yield surface is no longer a cylinder, but takes on a more random shape, as shown by Hsu.<sup>(4)</sup> The deviatoric components of stress vary with the hydrostatic component, therefore the yield locus for each hydrostatic pressure projects back onto a unique curve on the  $\pi$  plane. Since the hydrostatic pressures for each of the prestrained specimen yield points are different, projection back to the  $\pi$  plane produces a series of random points not of the yield.

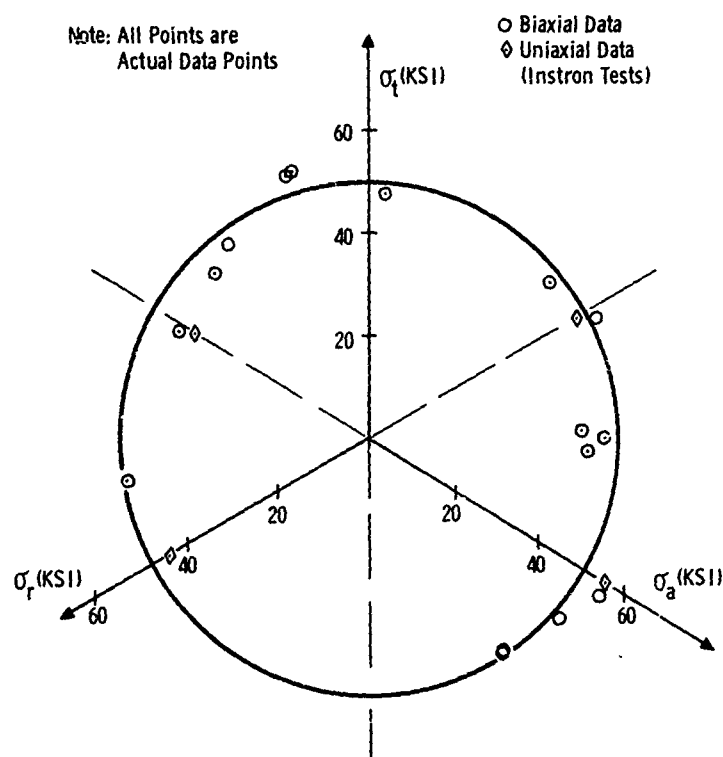


Figure 10  $\pi$ -Plane Yield Surface for 2024-T3 Aluminum in As-Received Condition (Virgin)

A note might be made of some of the difficulties experienced in obtaining the data. Buckling became a severe problem in the

MSL-70-12

third or compression-compression quadrant, with the specimens becoming unstable before bulk yielding was reached. One point was obtained for the virgin material, and none for the prestrained. Increasing the wall thickness to mean radius ratio of the specimen would have allowed higher stresses before buckling occurred, however, thicker specimens have greater variation of stresses and strains across the wall and reduce the resolution of yield and thus are undesirable. To insure a valid yield surface, additional points were obtained in the first and second quadrants and an existing specimen package was modified to obtain data in the fourth or axial tension-tangential compression quadrant.

#### DISCUSSION

Mair and Pugh<sup>(5)</sup> present four possible forms of subsequent yield surfaces, shown in Figure 11, due to different theories of work hardening. One of these is the isotropic hardening theory, which assumes that the subsequent yield surface is a uniform expansion of the initial surface about the same center point. Note that this theory allows for cross-effects, or cross hardening, wherein prestraining in one direction produces strain hardening in some other direction. This is exemplified by a change in the magnitude of a vector from the geometrical center of the yield surface to the surface itself following prestrain in another, generally orthogonal direction. Examples of cross-effects are shown in Figure 12. The isotropic strain hardening theory does not allow for the Bauschinger effect, e.g. the reduction in yield stress following stress reversal (see Figure 12). Another hardening theory, attributed to Batdorf and Budiansky, is the slip or independent loading surface theory, which states that the subsequent yield surface is the virgin yield surface enlarged to

MSL-70-12

include the prestrain point with the minimum amount of area. It leads to a corner on the yield surface and does not allow for cross-effects or fully for the Bauschinger effect. A third theory is the kinematic hardening theory which assumes that the subsequent yield surface is formed by rigidly translating the virgin surface, without expansion, in the direction of the pre-load. There is allowance for the Bauschinger effect but not for cross-effects. The final theory is one that Mair and Pugh attribute to Hodge, wherein the subsequent yield surface is explained by a combination of isotropic and kinematic hardening. Both cross-effects and the Bauschinger effect are covered by this general theory, which allows expansion and translation.

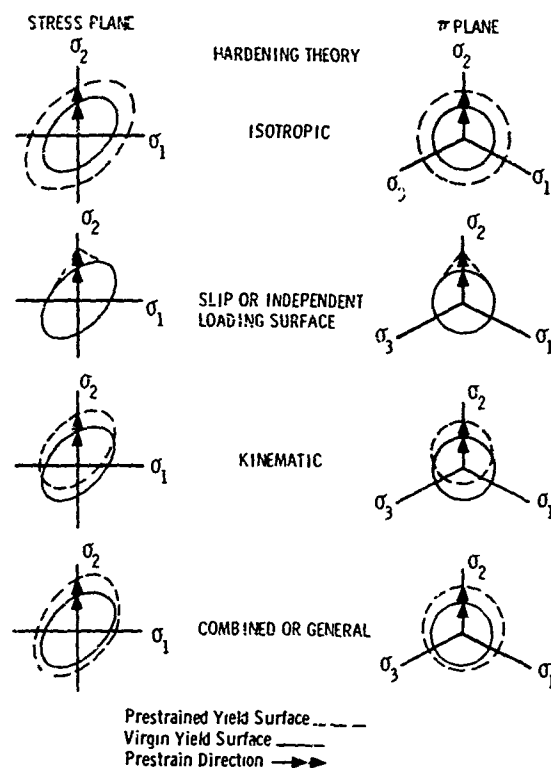


Figure 11 Comparison of Hardening Laws, or Subsequent Yield Theories

MSL-70-12

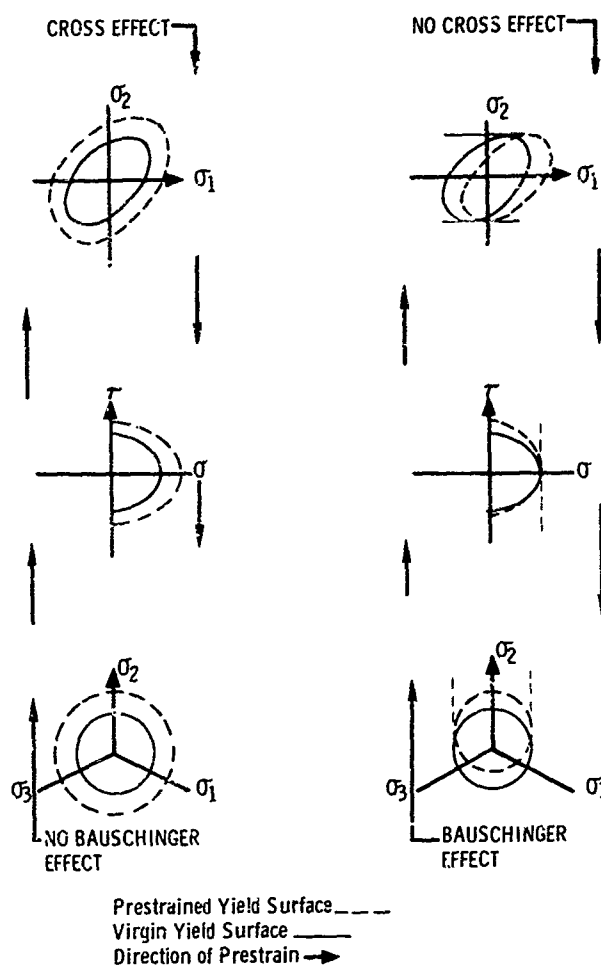


Figure 12 Illustrations of Cross-Effects and the Bauschinger Effect

The last theory appears to best represent much of the data gathered to date; however, available data does not clearly determine if corners exist. Naghdi, Essenburg and Koff<sup>(6)</sup> in tension-torsion tube tests on 24S-T4 aluminum found no cross effect, a definite Bauschinger effect, and that work hardening diminished toward the tension axis on a shear stress-axial

stress plot. They saw a high curvature near the shear stress axis which they felt was evidence of a corner. Ivey<sup>(7)</sup> in an investigation of several aluminum alloys obtained results similar to Naghdi, et al., except there was no indication of a corner. Both investigations found the yield surfaces to be convex although not necessarily enclosing the stress origin, and both found the initial yield surface to be closely approximated by the von Mises yield theory. From these it would appear that kinematic hardening was the best theory, but Szczepinski and Miastkowski<sup>(8)</sup> tried to fit the subsequent yield of an aluminum alloy with a pure kinematic hardening model and found great deviations for large plastic prestrains. Working with rectangular specimens, they also found that if they prestrained to various degrees in one direction and then loaded to a larger strain in the orthogonal direction, the yield surface was largely a function of the last leg of the prestrain path, the material "forgetting" its previous history. Among the studies that showed stronger evidence of corners was that of Bertsch and Findley<sup>(9)</sup> who experimentally were able to produce "rounded corners" by subsequent yielding under approximately equal biaxial stress. Shiratori and Ikegami<sup>(10)</sup> working with brass found that corners were evident for proportional stress loading paths but were not observed when the loading path was varied. Both investigations found that corners were not present under uniaxial stress prestrain conditions.

Aside from the varied materials tested by the investigators, the major cause of the differences in the reported data is the assortment of yield definitions employed. Mair and Pugh indicate this in discussing why they saw cross-effects in copper while Naghdi, et al. and Ivey did not. The latter studies define yield as the first departure from linearity, requiring

MSL-70-12

extremely sensitive transducers, while Mair and Pugh used both a "backward extrapolation" method and a "proof strain" method. The backward extrapolation method extrapolates the stress-strain curve back to the intersection of the elastic and plastic tangent lines, while a proof strain is a pre-selected offset plastic strain. Both the backward extrapolation method and the proof strain method require that the specimen be loaded into the plastic range, producing a yield stress greater than the linear limit value. The definition of yield, even the amount of offset in a proof method, plays a significant part in whether corners will be seen.<sup>(5)</sup> In the investigations above where proof strains or extrapolation methods were used, the amount of plastic strain to yield was approximately .01-.03%, an order of magnitude lower than the .2% generally employed in engineering analysis and used in this study for the generation of design data.

Returning to Figures 8 and 10, which represent the virgin yield surface of the 2024-T3 aluminum, note that the data could be well represented by the von Mises' yield criterion. The stress plane, Figure 8, shows the ellipse centered slightly away from the stress origin in the direction of the positive stress axis, and the major axis of the ellipse makes an angle of approximately 45° with the two stress axes; thus the variation from von Mises is small. In manufacturing the aluminum rod stock, the rod is stretched slightly along the axial axis accounting for the slight positive axial offset of the virgin material yield locus origin. The  $\pi$  plane representation, Figure 10, shows even less evidence of the origin being off center, and therefore, a circle, its center at the origin, has been fitted to the data.

Figure 9 provides evidence of the anisotropy produced by pre-straining. The center of the ellipse is significantly offset

MSL-70-12

in the direction of prestrain and the major axis has rotated away from the  $45^\circ$  line. The ratio of the minor to major diameters also increases indicating a general distortion of the shape of the von Mises ellipse. Neither an isotropic nor kinematic hardening theory would describe the yield surface of the prestrained aluminum.

Figure 13 shows the two yield surfaces plotted on the same stress plane for comparative purposes. Both yield surfaces are convex and enclose the stress origin. Recalling the previous discussion on yield criterion, note that the surface expands, translates in the direction of the compressive prestrain and also rotates slightly. Cross-effects do exist, which might be expected from the definition of yield used here, for Mair and Pugh show that

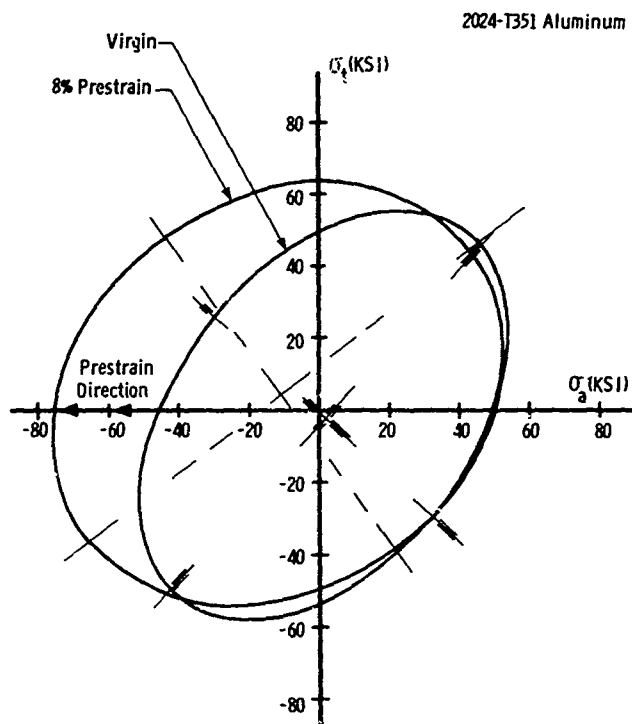


Figure 13 Comparison of Virgin and Prestrained Yield Surfaces



MSL-70-12

the proof strain yield definition leads to cross-effects, where the departure from linearity definition does not produce them. Likewise, corners detectable using departure from linearity would not generally be discernible using the techniques incorporated in this study. Evidence of the Bauschinger effect is seen in the substantial difference in the compressive and axial yield stress following compressive axial prestrain.

The subsequent yield surface of this material is best represented by the general hardening theory attributed to Hodge. This can be seen by a comparison of the lower part of Figure 11 with Figure 13. The general theory is a combination of the isotropic and kinematic (segmentwise linear theory) hardening theories, which Hodge called the piecewise linear isotropic hardening theory. As stated previously it is the only one that accounts for both cross-effects and the Bauschinger effect, however to account for additional distortion, such as the rotation seen here, Mair and Pugh felt the general theory had to be expanded. Again, the general theory does provide a sufficiently accurate presentation of the subsequent yield phenomena to be of use for the 2024-T3 aluminum.

## SECTION II

HEATING RATE STUDIES OF TWO  
ALUMINUM ALLOYS, 6061-T6 AND 2014-T6

## INTRODUCTION AND TECHNIQUE DESCRIPTION

In many applications, structural materials are heated rapidly and either simultaneously or after some short period are loaded to high stress levels. In this study, yield and flow stress were measured for two aluminum alloys, 6061-T6 and 2014-T6 at elevated temperature (see Appendix A for complete material descriptions). The effect of heating rate was studied at temperatures from 400 to 700°F where uniaxial stress tests were conducted at a nearly constant strain rate. Prior work<sup>(11)</sup> led to expectations of increased tensile yield strength with decreased heating time (or increased heating rate).

The tests were conducted utilizing the General Motors Ultra-High Temperature Medium Strain-Rate Machine<sup>(12,13)</sup> where direct electrical resistance is employed to heat the test specimen (Figure 14). Nearly linear heating rates in the range of 0.25 to 2500°F/sec can be obtained by controlling the current through the specimen. Immediately (within several milliseconds) after reaching test temperature, the specimens were loaded in uniaxial stress at a strain rate of about 10/second. This strain rate was used for all tests in order to keep the loading time (0.005-0.010 sec) significantly smaller than the shortest heating time (0.100-0.200 sec).

MSL-70-12

At heating rates below  $0.25^{\circ}\text{F}/\text{sec}$ , it was necessary to use a variation of the linear heating method described above. These low rates required heating the specimen over a period of hours or days. For these rates, the specimens were first heated in a radiant oven to the test temperature, maintained at this temperature for the desired time, removed from the oven, placed in the testing machine, reheated at  $25^{\circ}\text{F}/\text{sec}$ , and tested as described above.

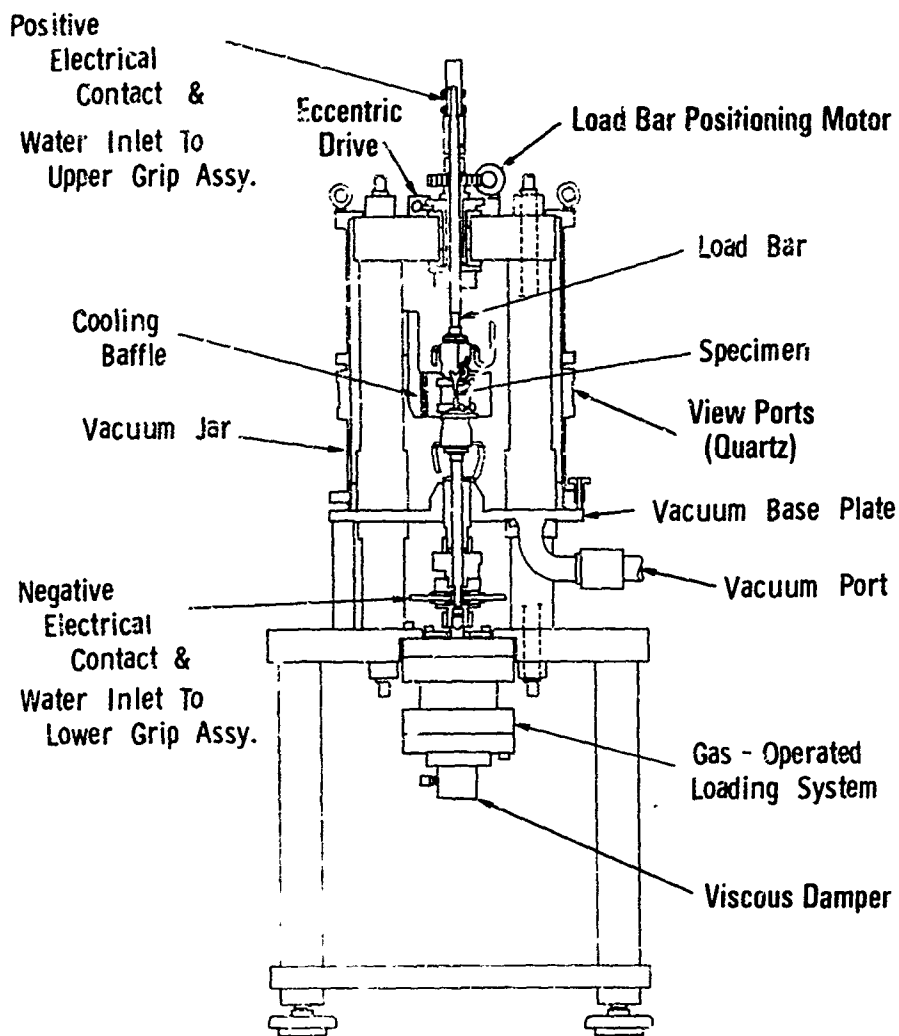


Figure 14 Schematic of Ultra-High Temperature Strain-Rate Machine

MSL-70-12

Manual control of the heating rate and machine firing proved satisfactory at rates up to 250°F/second. At higher rates, a simple open loop, timed-logic control was used. Consistent heating rates and test temperature was achieved after the proper equipment control settings were empirically determined.

Specimen load was measured from the output of semiconductor strain gages mounted on the test machine load cell, which were energized and monitored by an AC carrier oscilloscope plug-in module. Specimen strain in the reduced uniform gauge section was determined using two electro-optical trackers operated differentially. Dynamic load and gauge-section elongation data were observed on a dual beam oscilloscope and recorded photographically.

Specimen temperature at heating rates of 250°F/sec and below was measured with a 0.003 inch diameter chromel-alumel thermocouple. The thermocouple was mounted with a slight spring pressure contact on the specimen surface at the longitudinal center of the gauge length. The spring pressure was provided by the thermocouple leads. This technique along with the small thermocouple diameter provided adequate response at heating rates to 250°F/sec and minimized thermal gradients in the specimen due to sensor heating sinking. No embedding holes or bonding agents, which would create local stresses in the specimen, were required.

Thermocouple output voltage was observed on a chart recorder and tracked against a pre-determined graph to achieve a uniform heating rate. At rates above 250°F/sec the response limitations of the thermocouple and chart recorder required a change in technique for temperature measurement. A four microsecond time response infrared radiometric microscope, stati-

MSL-70-12

cally calibrated with a thermocouple reference on a typical test specimen, was used and observed on an oscilloscope.

The extremely low electrical resistance and high thermal conductivity of the aluminum alloy required minimizing the cross-sectional area of the test specimen to obtain rapid and uniform heating. A diameter of 0.100 inch was selected as a practical minimum to eliminate possible bending of the specimen during fabrication, handling, and insertion into the testing machine. In addition, this diameter was significantly greater than the mean grain size of the alloys. Machining of the specimens of the standard configuration (Figure 15a) with a gauge-section diameter of 0.100 inch was impractical. Therefore, a smaller specimen (Figure 15b) was designed along with re-usable adapters (Figure 15d) to fit the specimen to the test machine grips. Specimen blanks were cut parallel to the rolling direction, or x-axis (see Appendix A - Figure A3), of the 0.5 inch 2014-T6 plate by sawing and then lathe-turned to a cylindrical shape. Specimens (Figure 15b) were machined from these cylindrical shapes, and from the 6061-T6 rod stock, by precision centerless grinding. Diameter variations along the gauge length of any specimen were not measurable with a 0.0001 inch resolution micrometer, and variation from specimen to specimen was consistently less than 0.0005 inch. Concentricity along the specimen was within 0.001 inch TIR from end to end and surface finish was typically two to three microinches.

MSL-70-12

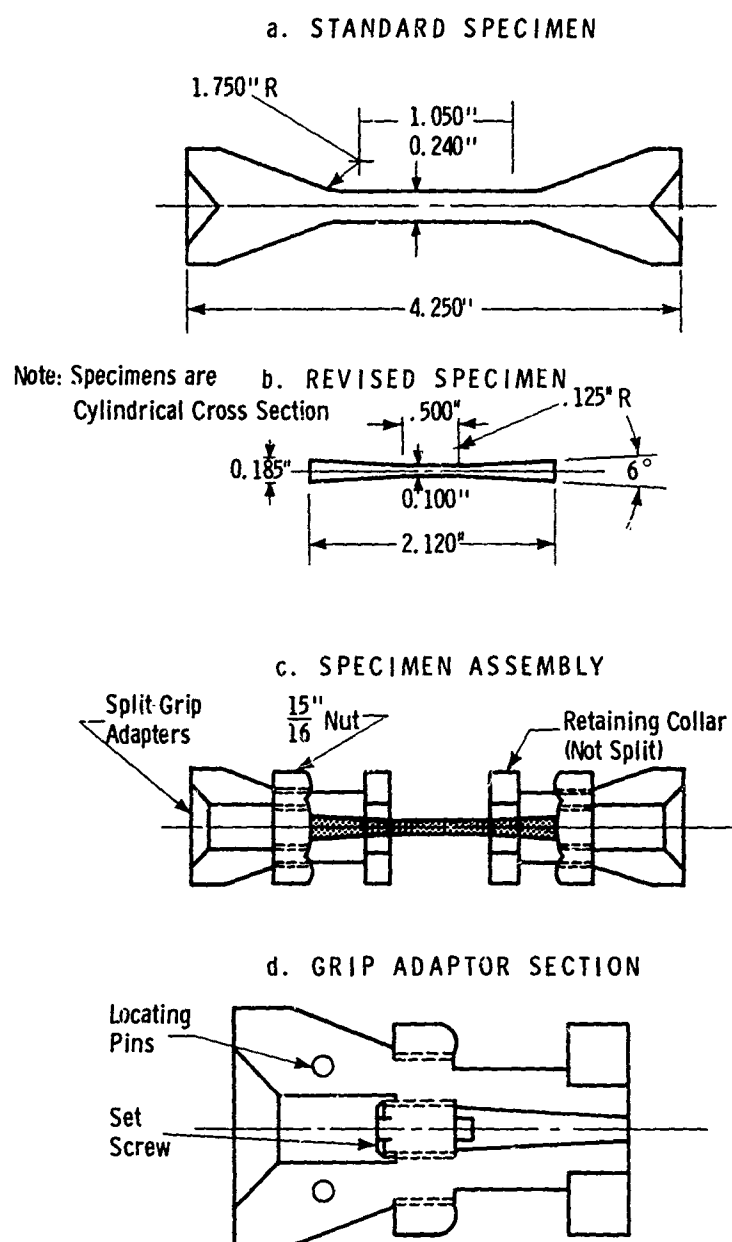


Figure 15 Test Specimens and Grip Details

MSL-70-12

## TEST RESULTS

Raw test data in the form of oscilloscope photographs and micrometer measurements of the specimen was reduced to tabular and graphic form with the aid of a digital computer. The photographs of load and displacement along with individual transducer calibration records were digitized by means of an optical tele-reader. This data, combined with the specimen dimensions, was used to obtain a graphic plot of engineering stress-strain. The uniaxial stress yield was obtained from these plots, where yield was defined as the first observed deviation from linearity in the elastic portion of the stress-strain curve. A minimum of three data points (and usually five or more) was obtained and used to calculate a mean value and standard deviation value for each heating rate/test temperature combination. Standard deviation values were computed according to the formula:

$$\sigma_x = \sqrt{\frac{\sum_{i=1}^n \sigma_i^2}{n-1}}$$

where

$\sigma_x$  = standard deviation

$n$  = number of stress values taken

$\sigma_i$  = deviation of  $i^{\text{th}}$  stress value from mean stress value.

This parameter was chosen as representing a conservative estimate of the probable error band for the measured stress values in view of the relatively small number of tests. (14)

A more rigorous analysis of the data would include modification of the "standard normal" distribution to encompass the extremely small ( $<30$ ) number of samples taken. The "student t distribution" may be used as such a modifier.

TABLE I  
STUDENT t DISTRIBUTION

	t <sub>0.100</sub>	t <sub>0.050</sub>	t <sub>0.025</sub>	t <sub>0.010</sub>	t <sub>0.005</sub>
1	3.078	6.314	12.706	31.021	63.657
2	1.886	2.920	4.303	6.965	9.985
3	1.638	2.353	3.182	4.541	5.851
4	1.533	2.132	2.776	3.747	4.604
5	1.476	2.015	2.571	3.365	4.032
6	1.440	1.943	2.447	3.143	3.707
7	1.415	1.895	2.365	2.998	3.499
8	1.397	1.860	2.306	2.896	3.355
9	1.383	1.833	2.262	2.821	3.250
10	1.372	1.812	2.228	2.764	3.169
11	1.363	1.796	2.201	2.718	3.106
12	1.356	1.782	2.179	2.681	3.055
13	1.350	1.771	2.160	2.650	3.012
14	1.345	1.761	2.145	2.624	2.977
15	1.341	1.753	2.131	2.602	2.947
16	1.337	1.746	2.120	2.583	2.921
17	1.333	1.740	2.110	2.567	2.898
18	1.330	1.734	2.101	2.552	2.878
19	1.328	1.729	2.093	2.539	2.861
20	1.325	1.725	2.086	2.528	2.845
21	1.323	1.721	2.080	2.518	2.831
22	1.321	1.717	2.074	2.508	2.819
23	1.319	1.714	2.069	2.500	2.807
24	1.318	1.711	2.064	2.492	2.797
25	1.316	1.708	2.060	2.485	2.787
26	1.315	1.706	2.056	2.479	2.779
27	1.314	1.703	2.052	2.473	2.771
28	1.313	1.701	2.048	2.467	2.763
29	1.311	1.699	2.045	2.462	2.756
Inf.	1.282	1.645	1.960	2.326	2.576



MSL-70-12

$$\text{Student } t \text{ Distribution} = f(t) \cdot c \left(1 + \frac{t^2}{v}\right)^{-\frac{v+1}{2}}$$

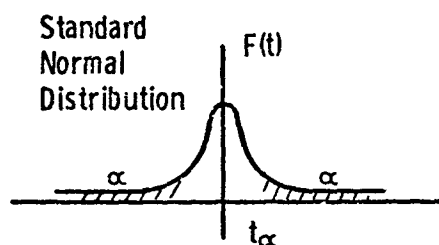
$f(t)$  = standard normal distribution

$c$  = constant

$v$  = degree of freedom of  $t$

=  $n-1$

$n$  = number of samples



This distribution modification is used to calculate a confidence interval,  $I$ , according to:

$$I = \bar{X} \pm \frac{t_{\alpha}}{\sqrt{n}} \sigma_x \quad (\text{II-1})$$

where

$\bar{X}$  = mean value (stress)

$\sigma_x$  = standard deviation

$n$  = number of samples

$t_{\alpha}$  = parameter given by "student  $t$  distribution".

The probability,  $P_{\sigma}$ , that  $x$ , the yield or ultimate stress, will be in the interval  $I$  for similar tests is given by:

$$P_{\sigma} = 1 - 2\alpha \quad (\text{II-2})$$

Equation (II-1) is of the form:

$$I = \bar{X} \pm C\sigma_x$$

where  $C = \frac{t_\alpha}{\sqrt{n}}$  modifies the standard deviation interval to include the statistical effect of small sample number.

Table I lists numerical values for the "standard t distribution" as a function of  $v$  and  $\alpha$ ; Figure 16 shows the standard deviation coefficient  $C$  as a function of the number of data samples for confidence levels between 80% and 99% ( $0.8 < P_\sigma < 0.99$ ).

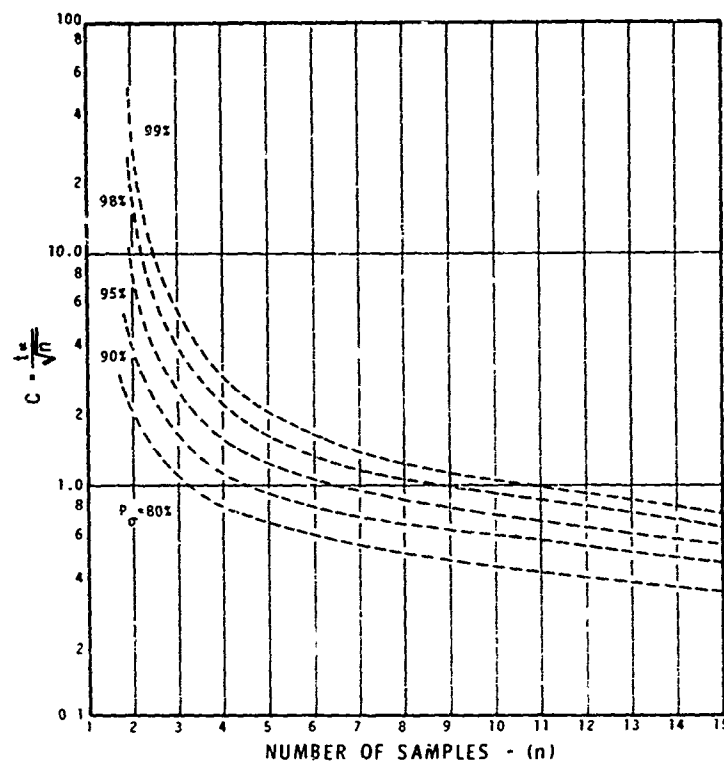


Figure 16 Standard Deviation Coefficient,  $C$ , as a Function of Number of Samples and Desired Confidence Interval

MSL-70-12

Thus, for design purposes, any required confidence interval for the experimental data may be expressed as the product of the standard deviation and the appropriate coefficient taken from Figure 16. It is obvious from this figure that for  $n \geq 3$  the standard deviation represents a conservative estimate of experimental error to a confidence of 80% at worst.

Typical stress-strain results for the 2014-T6 alloy at 500°F are shown in Figure 17. Yield and flow stress as well as elongation-to-fracture are all highly dependent on the heating rate. Figures 18 and 19 are plots of yield and ultimate stress as a function of heating rate from 400°F to 700°F. The smooth curves were drawn in general to represent the mean values of the data points. The error bands shown represent standard deviation from the mean. Similar results for the 6061-T6 alloy are shown in Figures 20 and 21, where yield and ultimate stress are plotted against heating rate at 500°F and 700°F test temperatures.

Elongation-to-fracture, defined as the total elongation of the gauge section divided by the initial gauge section length, for the two alloys after heating to 500°F at various heating rates is shown in Figure 22. In general, large scatter was observed primarily due to the effect of current flowing through the specimen during deformation which tended to heat up the material in the necked region. This current flow had a negligible effect on yield (and likewise ultimate) stress since little area reduction occurred at these points and since the time to reach these conditions was very short. A test was conducted to measure the temperature rise during necking of the specimen center for the most rapid heating test (2500°F/second). Results showed a temperature rise in excess of 100°F occurring at this rate between ultimate stress and fracture. Smaller temperature rises occurred at lower heating rates.

MSL-70-12

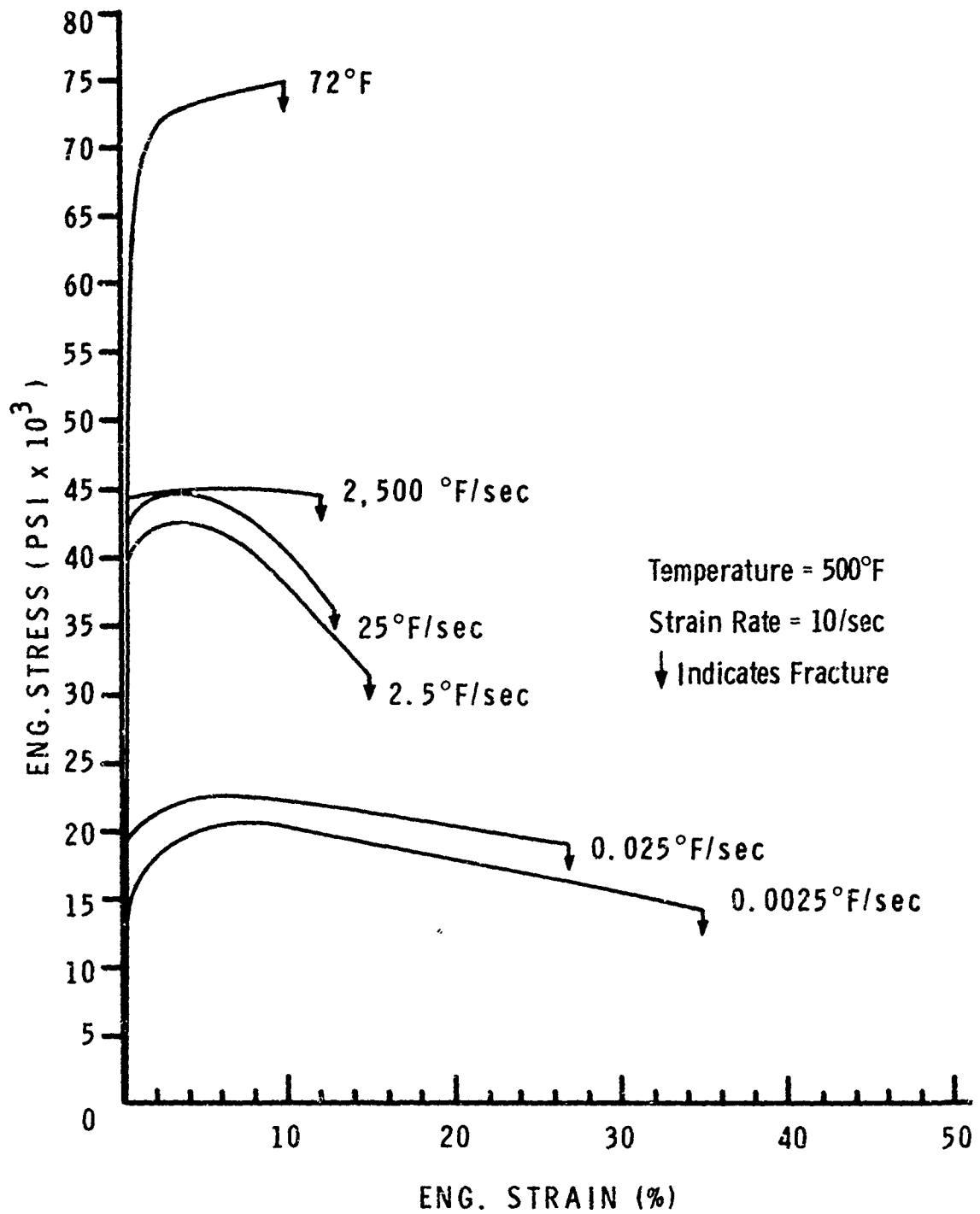


Figure 17 2014-T6 Aluminum Alloy, Average Stress-Strain Behavior at Various Heating Rates

MSL-70-12

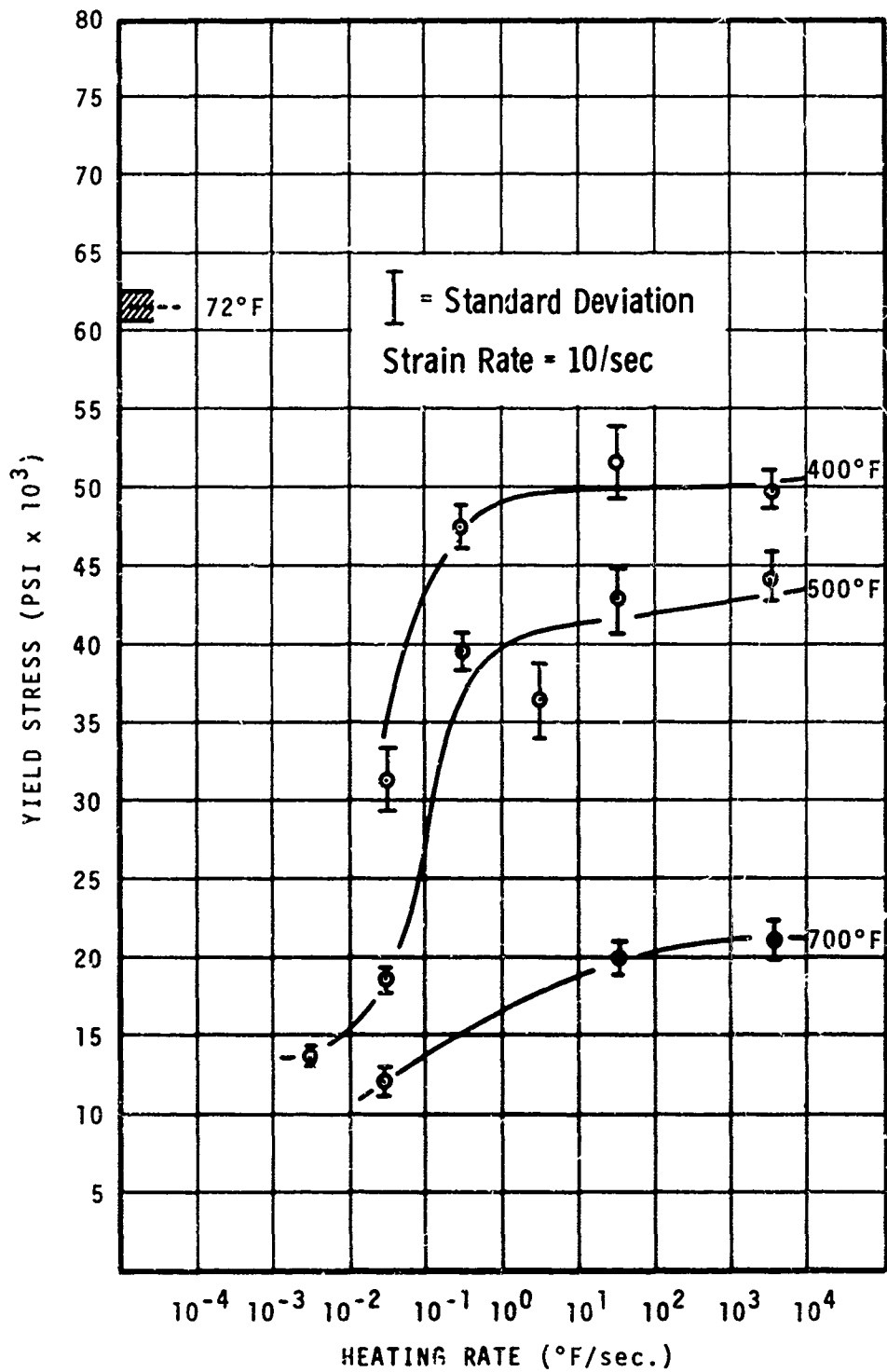


Figure 18 2014-T6 Aluminum Alloy, Yield Stress vs. Heating Rates at Various Temperatures

MSL-70-12

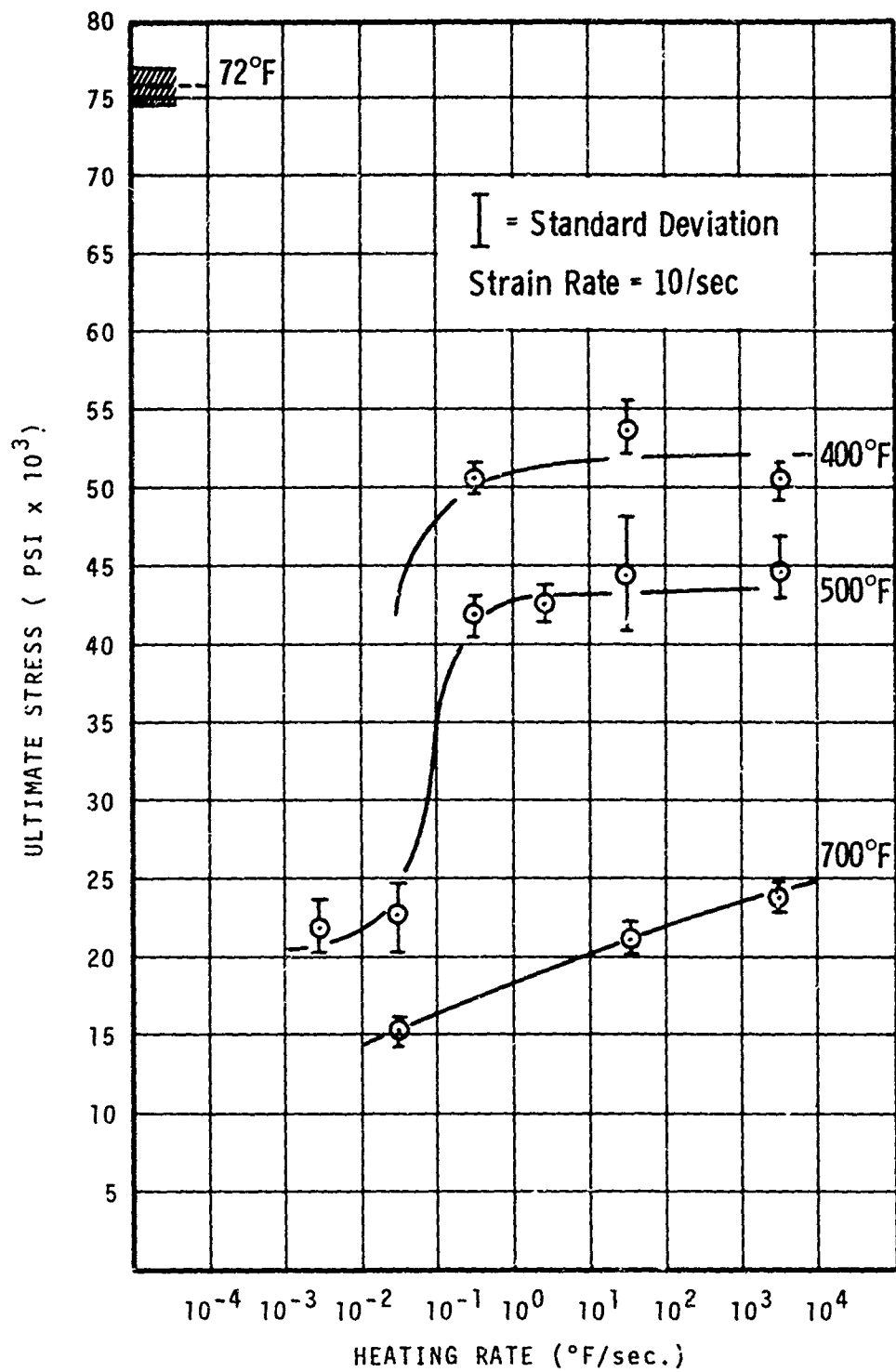


Figure 19 2014-T6 Aluminum Alloy, Ultimate Stress vs. Heating Rates at Various Temperatures

MSL-70-12

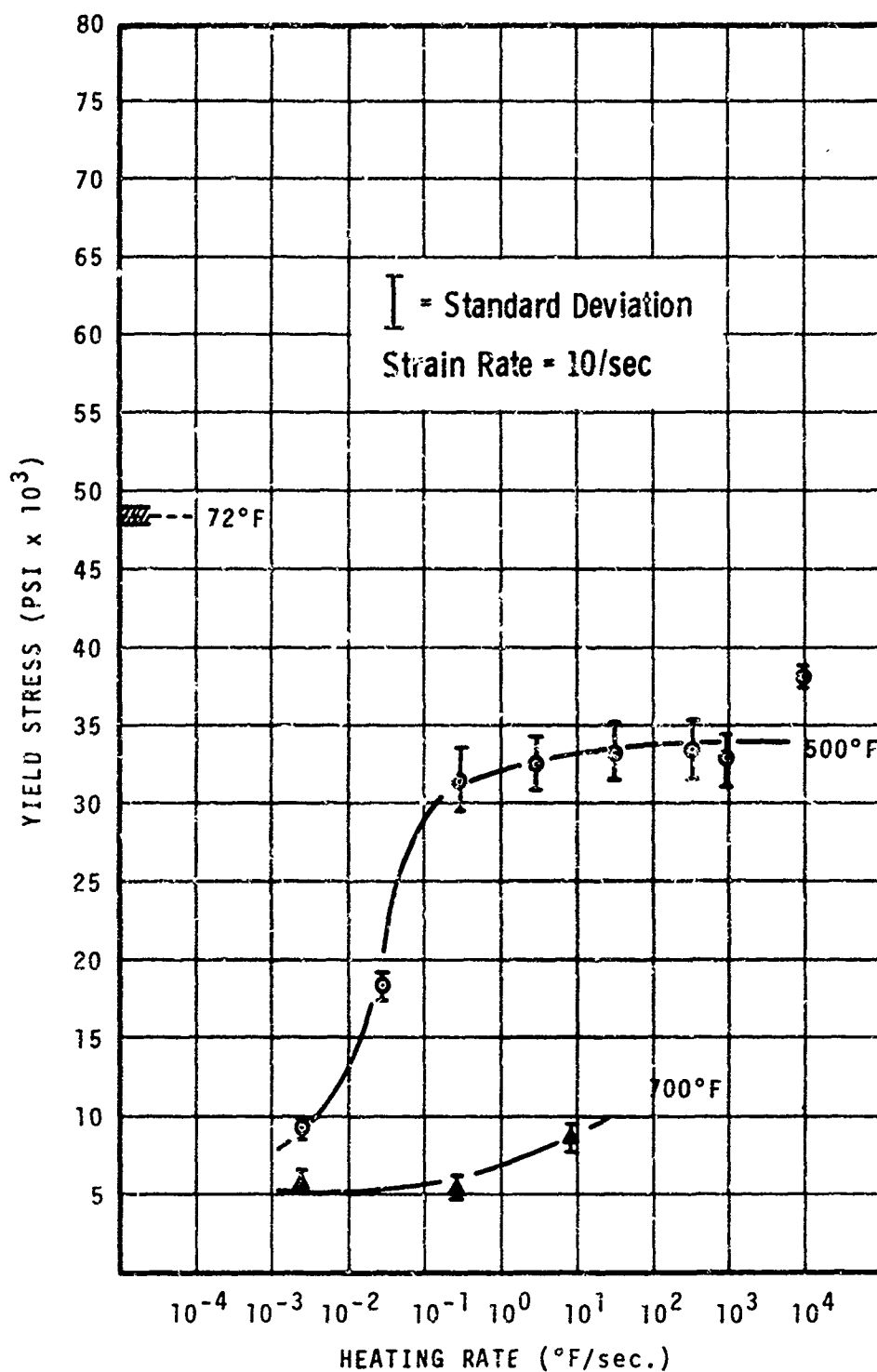


Figure 20 6061-T6 Aluminum Alloy, Yield Stress vs. Heating Rates at Various Temperatures

MSL-70-12

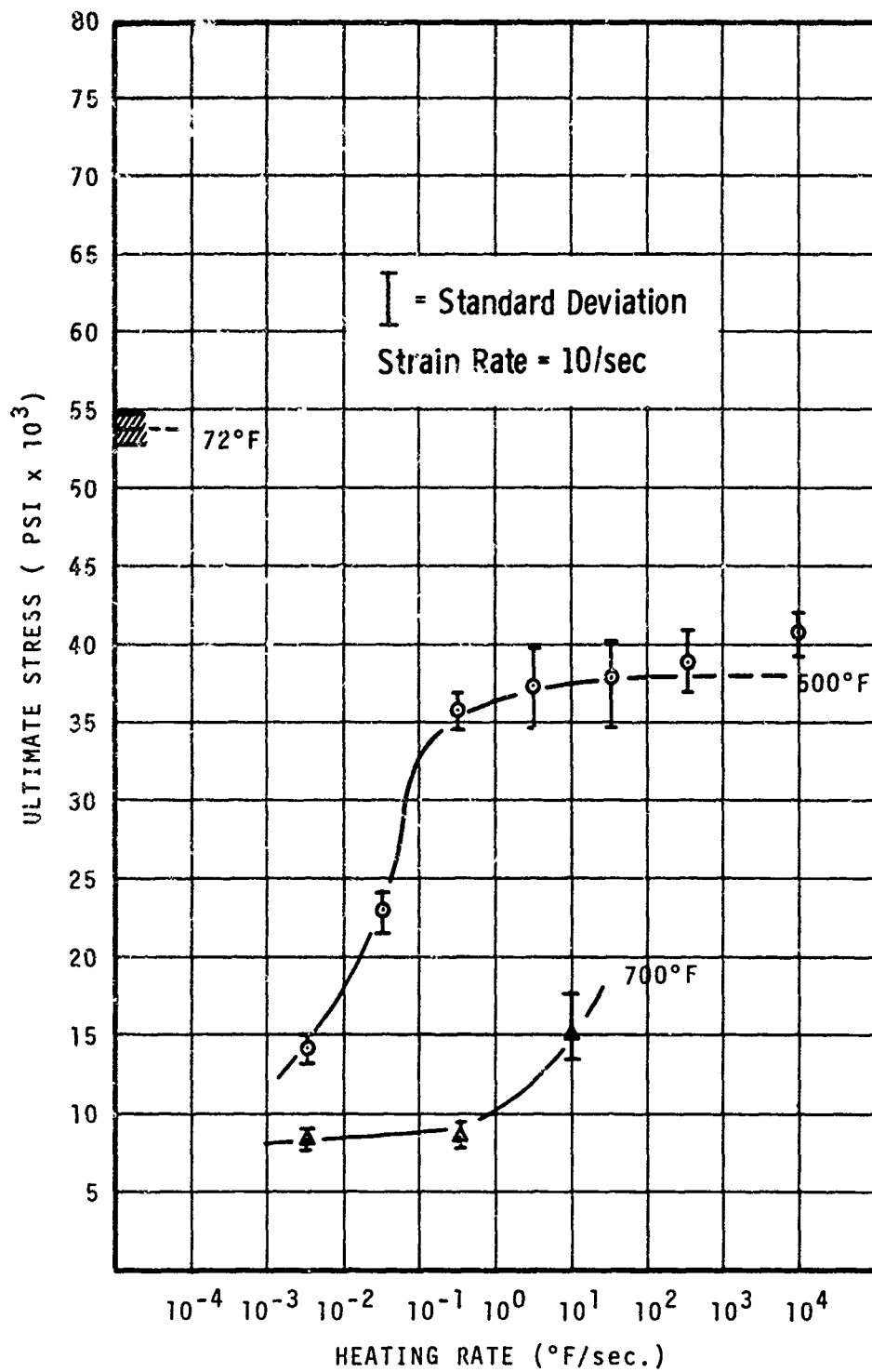


Figure 21 6061-T6 Aluminum Alloy, Ultimate Stress vs. Heating Rates at Various Temperatures



MSL-70-12

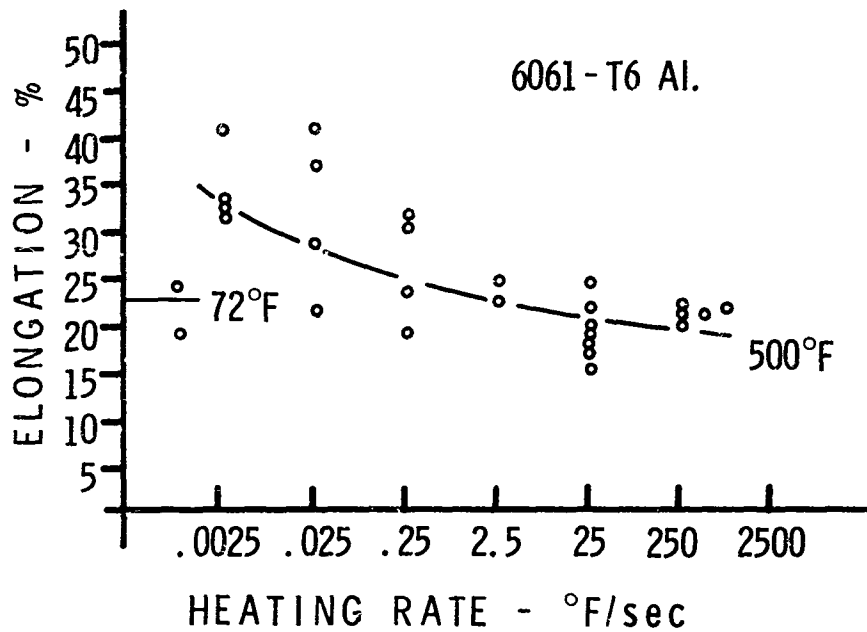
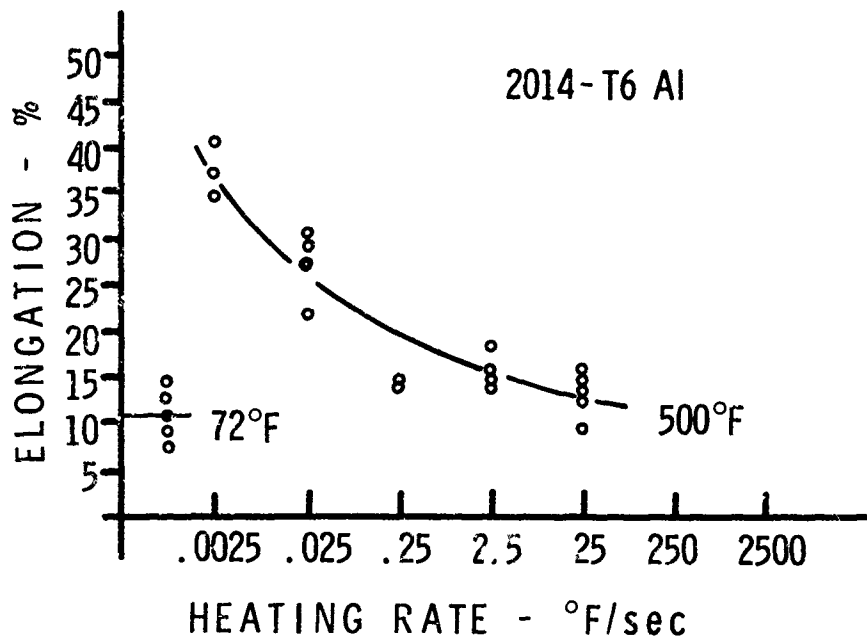


Figure 22 Elongation to Fracture vs. Heating Rate for 2014-T6 and 6061-T6 Aluminum

MSL-70-12

Some concern arose when it was observed that the data indicated the material to be most sensitive to heating rates between 0.025°F/sec and 0.25°F/sec where the method of heating was changed, as explained previously. To investigate the effect of these technique differences, control specimens were heated radiantly with a nearly linear temperature rise of 0.025°F/sec and then tested as described. The strength of the control specimens (heated linearly as a ramp function) was about 2 ksi (~10%) greater than the specimens heated at constant elevated temperatures (approximately a step function). This small discrepancy may be interpreted as arising from the increased time above the artificial aging temperature (~350°F) for the step function heating. This time above the critical temperature would be in error at most by a factor of two for the 700°F tests, which is insignificant when compared to the seven orders of magnitude of heating rate studied. Although this technique difference is evident, the resultant error is small and does not affect the trend of the data.

#### DISCUSSION

The principle process used to strengthen T6 alloys of aluminum involves artificial aging at approximately 350°F following solution hardening. This artificial aging accelerates precipitate hardening. The smaller percentage of alloying elements would tend to make the 6061 precipitation rate lower than the higher alloyed 2014.<sup>(15)</sup> Reactions of these two alloys to various heat treatments are shown in Figure 23 which indicates only a small difference in rates of precipitation of 6061 and 2014 alloys. The time required for a maximum hardening is slightly greater for 6061 at any given temperature than for the 2014 alloy, but the difference is not great.

MSL-70-12

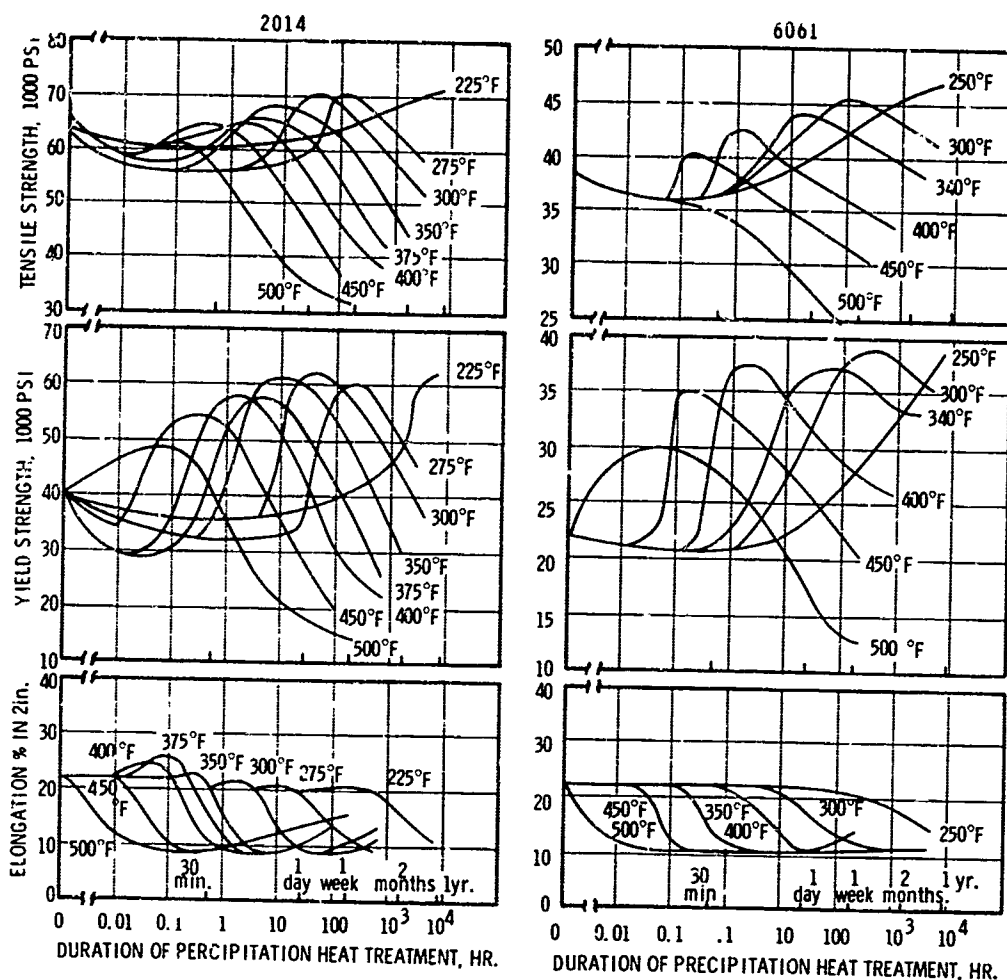


Figure 23 Artificial Aging Characteristics of 2014 and 6061 Aluminum Alloys Subsequent to Solution Hardening (Reference 15)

Since the materials were tested at elevated temperature, it is not possible to compare the data of the current study directly with the aging curves of Figure 23, as these aging curves are for the material behavior at room temperature. However, it is apparent that since the alloys tested in this study were originally near the fully hardened state, heating above the artificial aging temperature progressively changed the material to an overaged condition with increasing time at elevated temperature.

MSL-70-12

Figure 24 compares yield stress at temperature for various heating rates to published data for 6061-T6 (no cold work) held at elevated temperature for times between one half hour and 10,000 hours. (16) The strength at 500°F and 700°F for heating rates of 0.0025°F/sec and 0.025°F/sec is in general agreement with the published curves, which is meaningful in that the time to reach test temperature is of the order of 50 hours and 5 hours respectively at these rates. At heating rates above 0.25°F/sec, yield stress at temperature is significantly higher than the yield stress of material held at elevated temperature for 30 minutes, the difference being about 50% at 500°F. As is seen, the trends of the alloy strength at elevated temperature for all heating rates are similar to the published values for material held at constant elevated temperature for prolonged periods of time. Figure 25 shows similar results for the 2014-T6 alloy compared to curves representative to all aluminum alloys in the T6 temper.

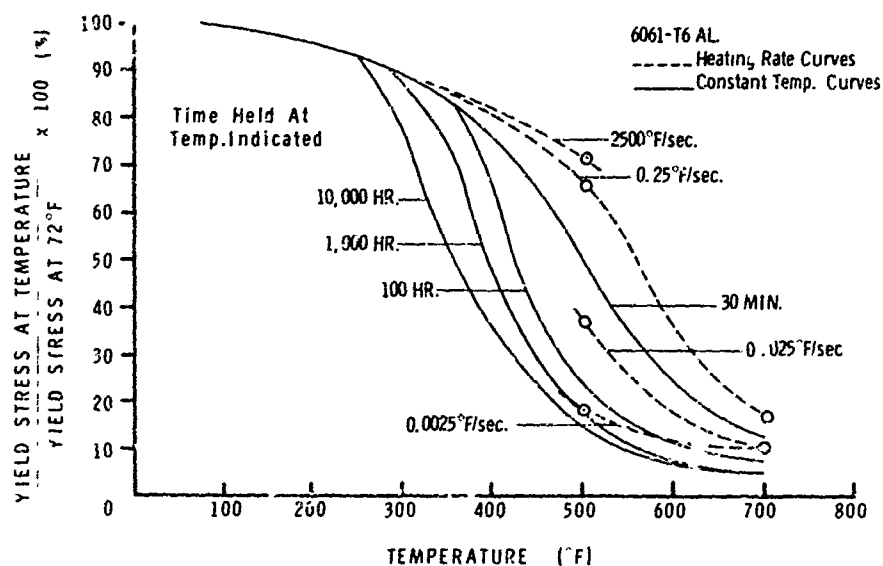


Figure 24 Normalized Yield Stress vs. Test Temperature for 6061-T6 Aluminum After Various Times at Temperature

MSL-70-12

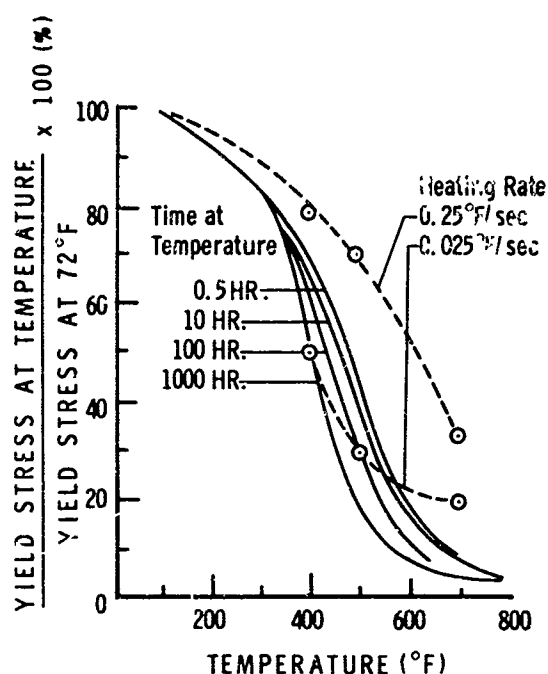


Figure 25 Normalized Yield Stress vs. Test Temperature for 2014-T6 Aluminum After Various Times at Temperature

Figures 26 and 27 illustrate the effect of temperature and heating rate on precipitation observed during this study. A specimen from each heating rate group\* at test temperatures of 500°F and 700°F was sectioned parallel to the cylindrical axis, mechanically polished, and chemically etched using Kellers etch<sup>(17)</sup> for 60-90 seconds to accentuate grain boundaries and precipitates. The prepared surface was examined optically and with an electron microscope. Photographs 3 through 7 of Figure 26 show the 6061-T6 alloy after heating of 500°F at rates from 0.0025 to 2500°F/second. Above 0.25°F/sec (Photos 5, 6, 7) the precipitates are dispersed so finely that they are not visible. At

\* These specimens were heated to temperature at nearly constant heating rate, and cooled to room temperature in air.

MSL-70-12

heating rates of 0.0025°F/sec (Photo 3) and 0.025°F/sec (Photo 4), relatively large precipitates appear distributed uniformly throughout the grains and along grain boundaries. Photographs 1 and 2 show the same trend at 700°F with the precipitates forming rather gross inclusions at a heating rate of 0.025°F/sec. Photos 8 through 12 are scanning electron microscope pictures of the same specimens showing the material texture becoming very coarse and porous for the longer heating times; the voids are believed to be precipitate locations with the precipitate removed during etching. Again, little change is observed at heating rates above 0.25°F/second. No evidence of grain growth or recrystallization is observed except perhaps for the 700°F tests at a 0.025°F/sec (Photo 1) heating rate. This is in good agreement with published observations of grain growth in aluminum alloys generally above 750°F but not below 650°F.<sup>(15)</sup> Little or no variations in precipitation size or density was seen between material before and after deformation as has been observed previously.<sup>(11)</sup>

Microscope examinations of the 2014-T6 alloy, Figure 27, shows the same trend toward precipitation coalescence with longer heating times although it is not as clear as the 6061 photos. The 2014, due to the high percentage (~4.4%) of alloying copper, contains relatively large particles of high copper precipitate in the T6 condition as evidenced by the large white spots in the photographs, point 1, Photo 11, Figure 27. These precipitates are seen to grow in size and number as heating time increases. The elemental compositions of the precipitates was measured in a relative way using secondary X-ray emissions in the scanning electron microscope. Point 1, in Photos 7 through 11 represents high copper precipitates (~6:1 ratio over surrounding area). Point 2, Photo 8, indicated high manganese content, as did point 2, Photo 9, while point 3, Photo

MSL-70-12

8 showed relatively high concentration of manganese, iron, copper and silicon. The other points indicated showed some traces of the alloying elements but were predominantly aluminum. X-ray analysis of the 6061-T6 alloy was thwarted by the small percentage of alloying elements (1.2% max) and by the closeness of the characteristic X-ray energies of the alloying elements--the X-ray spectrometer could not resolve the aluminum, silicon, and magnesium lines although some indication of silicon precipitation was seen at various precipitate spots as a broadening of the aluminum Ka X-ray line on the high energy side. The silicon Ka line (1.8 ev) is just slightly higher than the aluminum Ka line (1.5 ev).

The times at temperature required to soften the material are similar to the aging curves of Figure 23. This would suggest that in heating times shorter than about 15 minutes, little variation should be seen in the mechanical properties as a function of heating rate or time at temperature. Therefore, the mechanical properties at higher heating rates might be assumed equal to those between 0.25 and 2500°F/second. This assumption would simplify material modeling in high heating rate environments, but its validity is dependent on precipitation hardening being a predominant strengthening mechanism and reaction rates being too slow to proceed very far when the material is heated rapidly and for short periods of time.

MSL-70-12

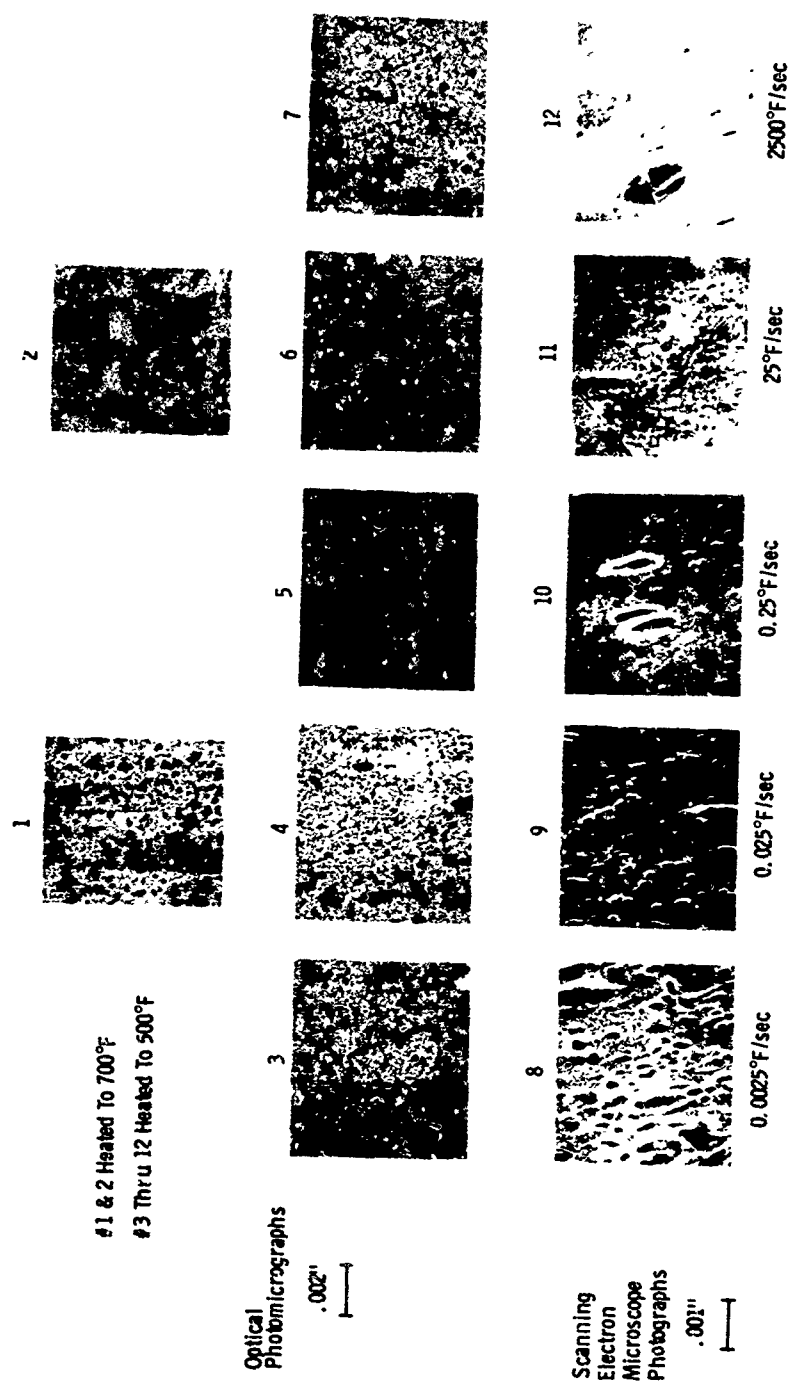


Figure 26 Metallography Study of 6061-T6 Aluminum



MSL-70-12

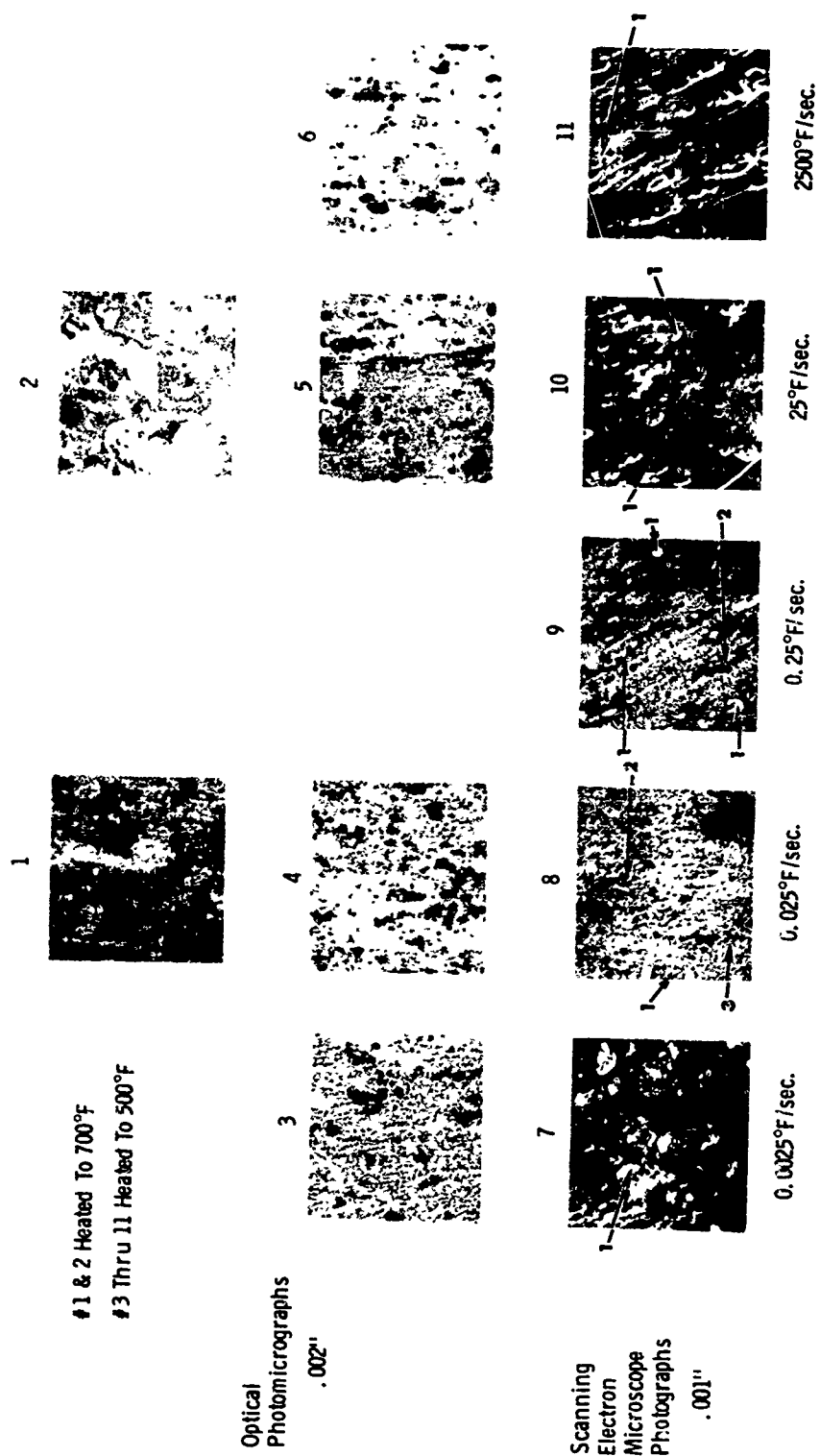


Figure 27 Metallography Study of 2014-T6 Aluminum

## SECTION III

SHOCK PROPAGATION AND FRACTURE CHARACTERISTICS  
OF 2014-T6 ALUMINUM

## INTRODUCTION

The prediction of the response of structures to impulsive loading has been studied extensively during the last decade. Out of these studies sophisticated computer codes have been developed which may be used to assess structural response.<sup>(18,19)</sup> These codes are designed to model both the initial phase of loading, when stress waves are propagated through the structure, and later time response, when large permanent deformations result. However, to use these computer codes effectively, input parameters must be determined for the structural materials of interest.

The purpose of the present study is twofold; (1) to provide these input parameters for an important structural aluminum alloy, 2014-T6, and (2) to provide basic understanding of the shock propagation and fracture characteristics of this alloy. The following often serve as input data for modeling of shock propagation and dynamic fracture (quasi-static inputs not listed): elastic constants, Hugoniot equation of state, precursor amplitude, and dynamic spall strength. Values for some or all of these quantities are usually sufficient for making preliminary code calculations of material response. However, if predicting early time shock propagation is of interest, time dependent models usually must be developed, and to assess their validity certain checks must be applied. Some

MSL-70-12

readily available checks are elastic precursor decay, compressive wave profiles, spall wave correlation profiles\*, and release paths.

In concluding this study, an effort was made to correlate the results to available data on another aluminum alloy, 6061-T6 aluminum. It is hoped that by such a comparison, users of these reported results on 2014-T6 might extend their understanding beyond the scope of this study to the wealth of available data on 6061-T6 aluminum.

#### EXPERIMENTAL TECHNIQUES

Experimental measurements made are separable into the following categories: elastic constants, hugoniot equation of state, wave profile studies, spall recovery tests, and spall wave profile measurements. Three different laboratory instruments were used in making these measurements: ultrasonic instrumentation for elastic constants measurements, a 63.5 mm bore compressed air gun for spall recovery studies, and a 102 mm bore compressed air gun for the hugoniot, wave profile and spall wave profile measurements.

##### 1. Elastic Constants Measurements

The three basic measurements made to determine elastic constants are density and dilatational and shear wave velocity. Density was determined by measuring the mass and volume of several cylindrically shaped specimens.

---

\* Spall wave correlation profiles refer to free surface velocity-time profiles recordable at a specimen free rear surface beneath which dynamic fracture occurs.

MSL-70-12

Wave velocities were determined by measuring wave transit times through specimens of known thickness. A pulse superposition technique was used for these transit time measurements.<sup>(20)</sup> This technique, which gives good accuracy ( $\sim 1$  part in  $10^4$ ), was also used for determining changes in transit time as a function of temperature and hydrostatic pressure. Measurements were made over a temperature range from 25 to 200°C, and a pressure range from 0 to 8 kilobars.

A block schematic of pulse superposition instrumentation is shown in Figure 28. The theory of operation is as follows. A transducer, either longitudinal or shear mode, is bonded to one side of a disk shaped specimen with parallel, flat, polished surfaces. A short radio frequency burst, matched in frequency to the resonant frequency of the transducer, is applied to the transducer. The transducer, which is both a transmitter and receiver, transmits an ultrasonic wave into the specimen. This wave reflects off the back surface of the specimen and is received as an echo by the transducer. If a second RF burst is applied at the time this first echo is received and a third at the time the second echo is received, etc, the echo amplitudes will add. In order to determine when addition occurs, it is necessary to interrupt the RF bursts to be able to observe the decaying echos. Then the repetition rate of the RF bursts, which determines the time between pulses, is adjusted to give maximum echo amplitudes, i.e., exact superposition. The wave transit time through the specimen is then one-half the reciprocal of the oscillator frequency (which controls the RF repetition rate). For the experimental setup used, the variable frequency oscillator is a General Radio Model 1163-A, the pulse generator is a Hewlett-Packard Model 214-A, the RF pulse oscillator is an Arenberg Model PG-650-C, the impedance matching transformer is an Arenberg Model WB-100, the wide band amplifier is an Arenberg Model WA-600-D and the frequency counter is a TSI Model PA-620.

MSL- 7-12

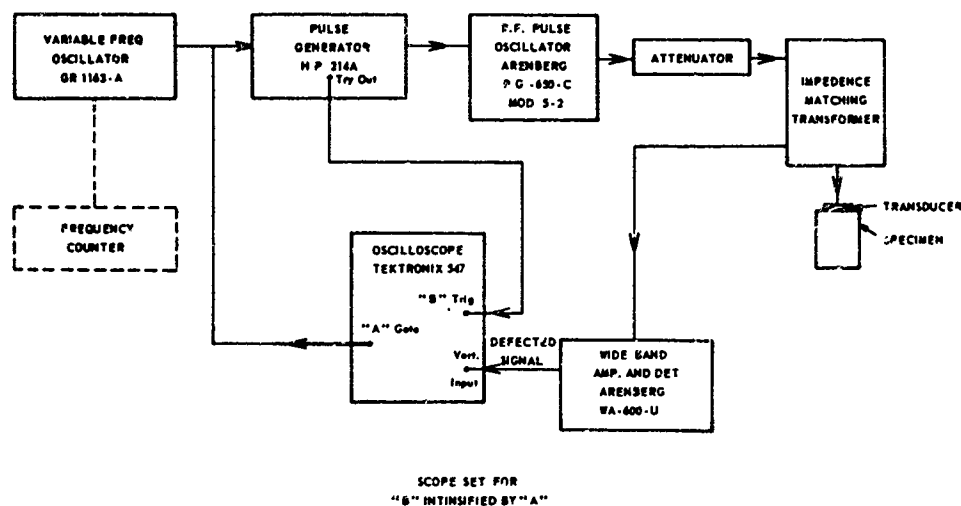


Figure 28 Pulse Superposition Technique Schematic

The pulse superposition technique was also used to determine the temperature and pressure dependence of the elastic wave velocities, however, changes in specimen length with temperature and pressure must be incorporated into results of transit time measurements in order to compute correct wave velocities.

The temperature dependence of elastic wave velocities is determined by immersing the specimen, with transducer attached, into a constant temperature bath. A Blue M Electric Co. Model 60 bath with HTF-100 UCON fluid was used for this purpose. Generally, the upper temperature limit is determined by the transducer/specimen bond material and is about 300°C for dilatational waves and 100°C for shear waves.

Measurement of the pressure dependence of wave velocities was made using a static high pressure apparatus illustrated in Figure 29. The hydraulic system consists of two parts; a low

MSL-70-12

pressure portion which transmits pressure to a high-pressure portion which transmits pressure to the vessel containing the specimen. The usable portion of the pressure vessel is 2.5 cm diameter by 15 cm long and the working fluid is Octoil-S. A pressure range from 0 to 8 kilobars was used for the measurements made on 2014-T6 aluminum. Pressure was measured with a manganin pressure cell monitored with a resistance measuring bridge. Since pressure dependence is determined under isothermal conditions, temperature of the working fluid was monitored.

Propagation direction was normal to the 12.7 mm plate stock for these wave velocity measurements.

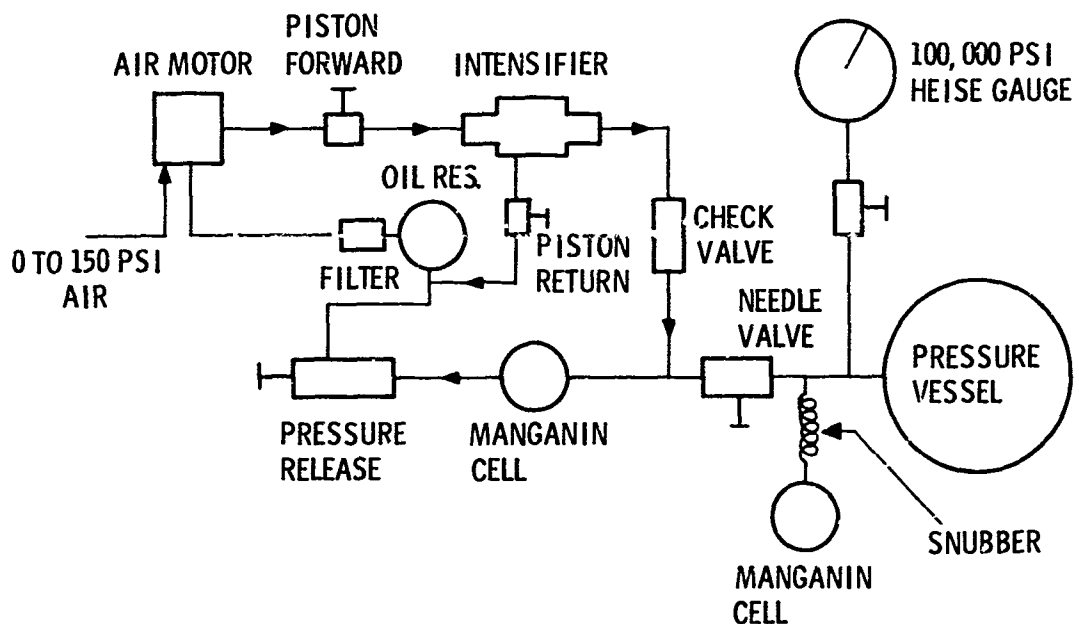


Figure 29 Static High-Pressure Apparatus Schematic

MSL-70-12

## 2. Spallation Threshold Measurements

For the spallation studies specimens were recovered after shock loading and examined to determine the extent of dynamic fracture. Spallation recovery tests were conducted using the 63.5 mm compressed air gun shown in Figure 30. These shots were instrumented to record only impact velocity. The velocity measurement system, ending 2 cm from the muzzle of the gun, includes a light source, a collimating lens, and five sets of equally spaced slits in the launch tube. The slits create five narrow, parallel light beams crossing the launch tube and emerging from holes on the opposite side, where they are focused by another lens onto the sensitive element of a photomultiplier tube. An opaque projectile passing through the launch tube successively interrupts these light beams, so that when the output of the photomultiplier is recorded with an oscilloscope, projectile velocity can be determined to within  $\pm 1\%$ .

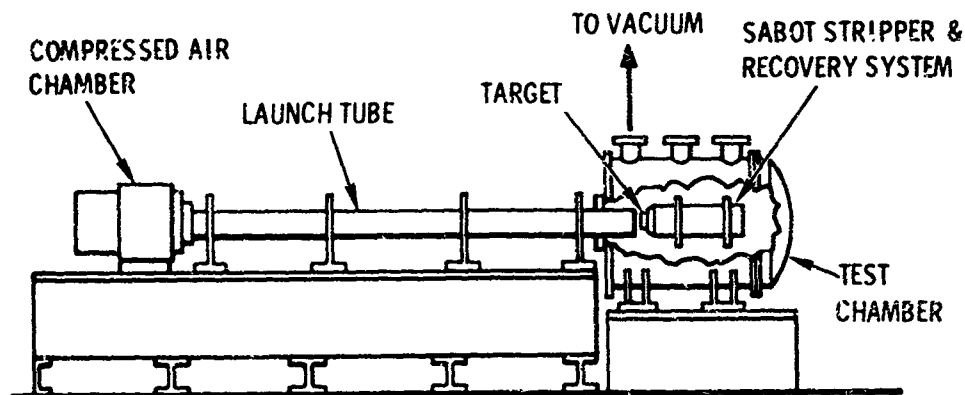


Figure 30 63.5 mm Compressed Gas Gun Schematic

MSL-70-12

The impactor and target are shown schematically in Figure 31. For the spallation threshold studies, the impactor and target were both 2014-T6 aluminum with the ratio of target thickness to impactor thickness  $\sim 1.8$ . Two impactor thicknesses were used, 0.6 and 1.6 mm. The extent of dynamic fracture was determined by sectioning recovered specimens across a diameter, polishing, etching, and examining optically at a magnification of 25 to 100X. Specimens were then graded according to the degree of fractures to complete material separation. The incipient spall threshold was defined as the impact velocity corresponding to cracking over 50% of the specimen on a projected length basis.

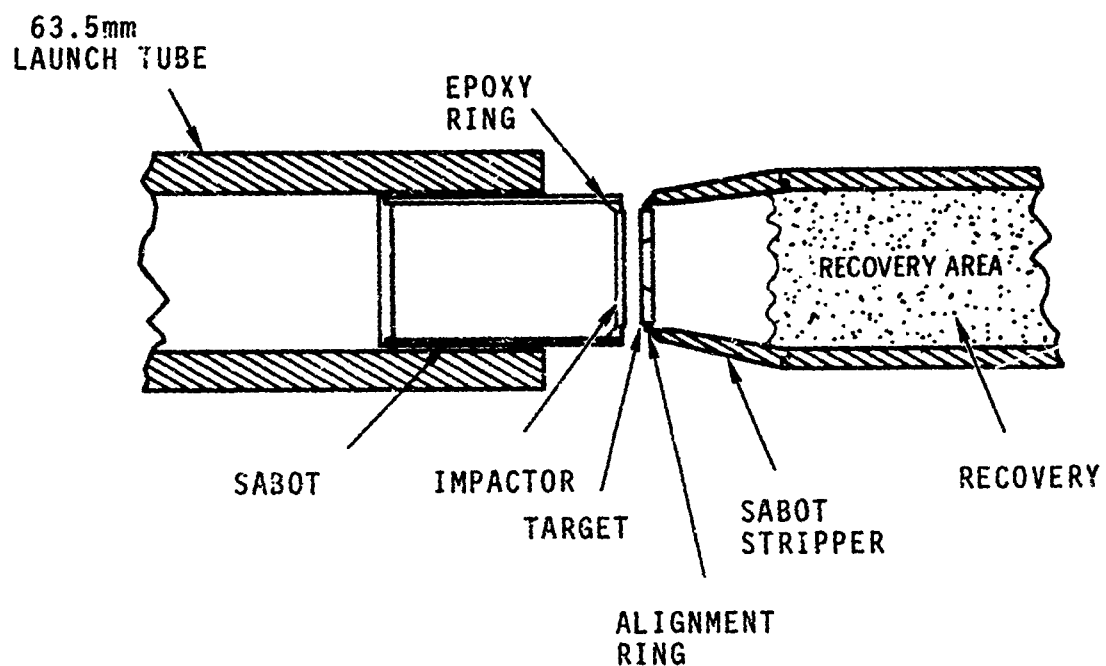


Figure 31 Room Temperature Spall Test Schematic



MSL-70-12

### 3. Hugoniot Measurements

Four shots were fired to determine the hugoniot of 2014-T6 aluminum to 50 kilobars. Two of these shots were a "direct impact" technique where an aluminum specimen was impacted directly upon a quartz gauge. The other two shots employed a "buffered direct impact" technique where a tungsten carbide disk was placed in front of the quartz gauge in the target. These two techniques are illustrated in Figures 32 and 33. The buffered technique was used for the higher stress shots ( $\sim 35$  and 50 kilobars between aluminum and tungsten carbide).

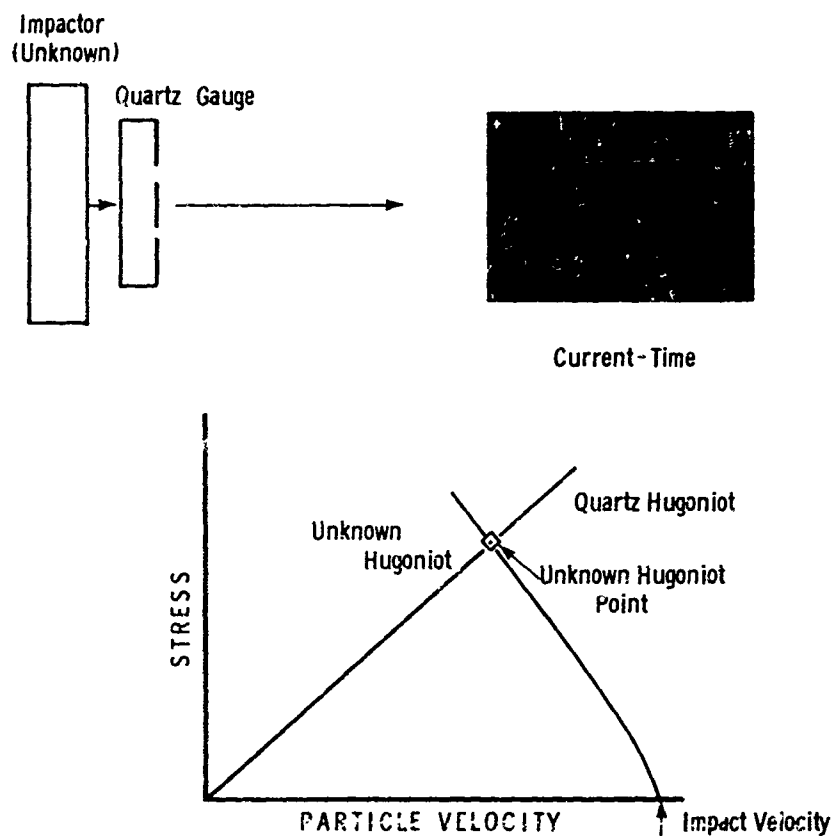


Figure 32 Schematic of Direct Impact Technique

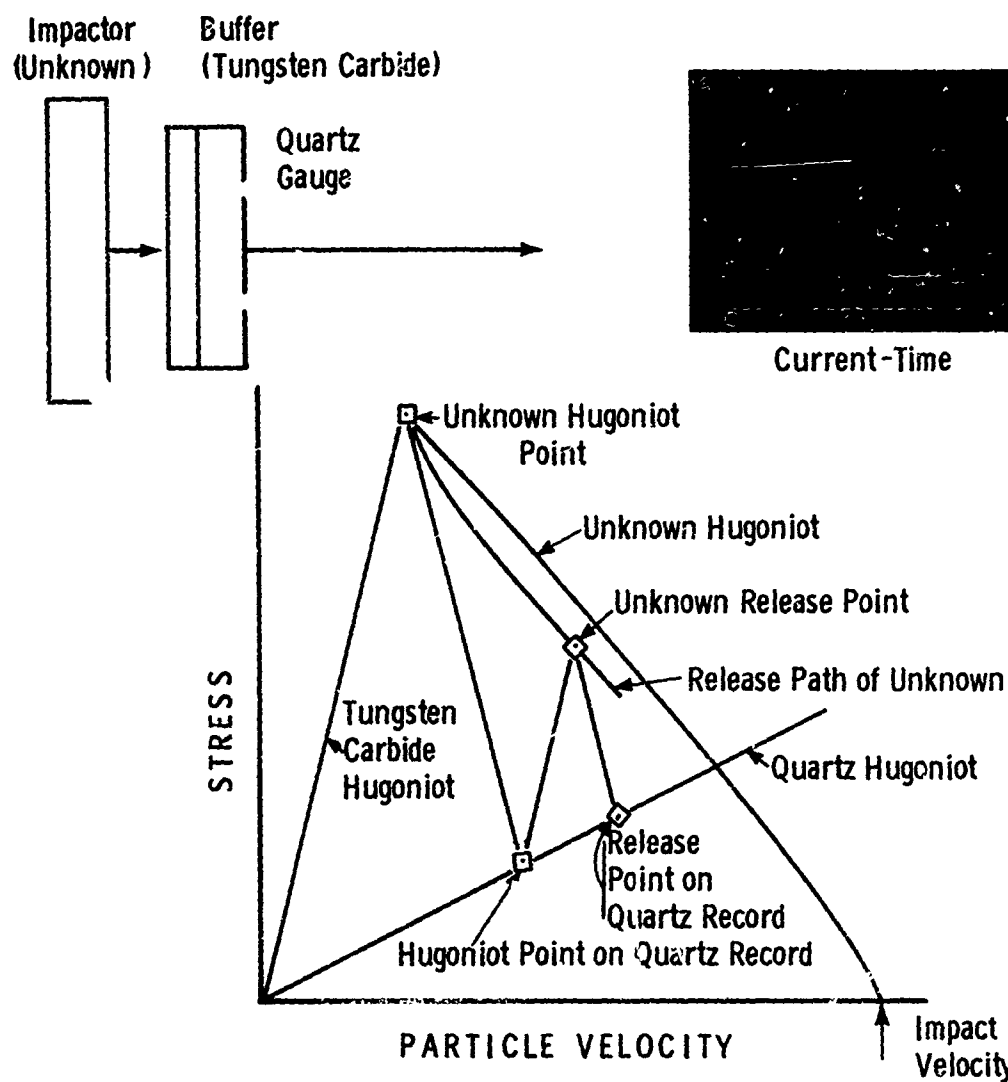


Figure 33 Schematic of Buffered Direct Impact Technique

The 102 mm bore compressed air gun, shown in Figure 34, was used in conducting hugoniot studies as well as wave profile and spall wave profile studies whose descriptions follow later. This gun is equipped with systems which measure projectile velocity and tilt angle between impactor and target at impact.

MSL-70-12

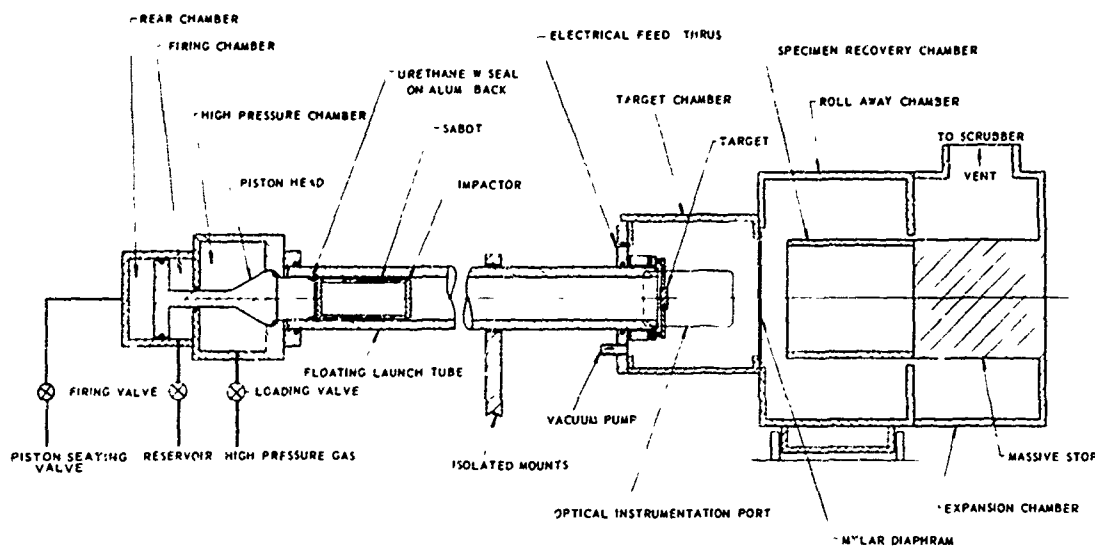


Figure 34 102 mm Compressed Gas Gun Schematic

Projectile velocity was measured by a pin shorting technique. As the impactor neared the target, five pins of accurately known distance separation were successively shorted. The shorting time of each pin was read out directly on a digital counter, from which impact velocity,  $V_I$ , was computed. Impact velocity measured this way is accurate to about 0.5%.

Tilt was not recorded for hugoniot shots but was measured on wave profile shots. Tilt was measured by means of a shorting pin technique. Four pins, all in the plane of the target, are shorted during impact by the face of the impactor which is grounded by a pin protruding ahead of the tilt pins. From tilt pin shorting times, recorded by digital counters, tilt angle at impact is computed. Tilt angles did not enter into data analysis

but were used only to determine planarity of impact for the purpose of screening out bad shots. Tilt angles less than one milliradian were, in general, judged acceptable for this study. In practice, tilt angles were typically 0.5 milliradians or less.

Quartz gauges used for stress measurements were  $1/4"$  X  $1 1/4"$  diameter disks with  $1/2"$  active electrode diameter. These gauges, obtained from Valpey Corporation and characterized by Graham<sup>(21)</sup>, produce a current proportional to stress at the front surface, for a recording time of one microsecond. The active electrode area of each gauge was connected to three oscilloscopes using low-loss foam dielectric instrumentation cables. The oscilloscopes were Tektronix, Type 547 and Type 454, with fast writing rate P-11 phosphor. Quartz gauge current-time data were recorded on Polaroid film along with time calibration marks and current calibration lines.

#### 4. Wave Profile Measurements

Wave profile measurements were made using a "transmitted wave" technique. A fused quartz (tungsten carbide for two shots) impactor was propelled against an aluminum target. After impact, stress waves propagated through to the target back surface, where they were recorded by measuring either stress with a quartz gauge, or interface velocity between the target and fused quartz. Interface velocity measurements were made with the laser velocity interferometer for which fused quartz was used as a "window" for the laser beam. It has been characterized for this purpose by L. Barker.<sup>(22)</sup>

MSL-70-12

The instrumentation system for the laser velocity interferometer is shown in Figure 35. This system consists of a Perkin-Elmer Model 5800 Laser, a series of mirrors directing the laser beam towards the target, a focusing lens to focus the beam at the specimen-fused quartz interface in the target, a silvered dot at this interface from which light is reflected, a series of mirrors to direct the reflected beam back to an optical bench, a beam splitter which splits the reflected light (half of which goes through a delay leg but then is combined later with the reflected beam), and an ITT Model F4034 photomultiplier tube.

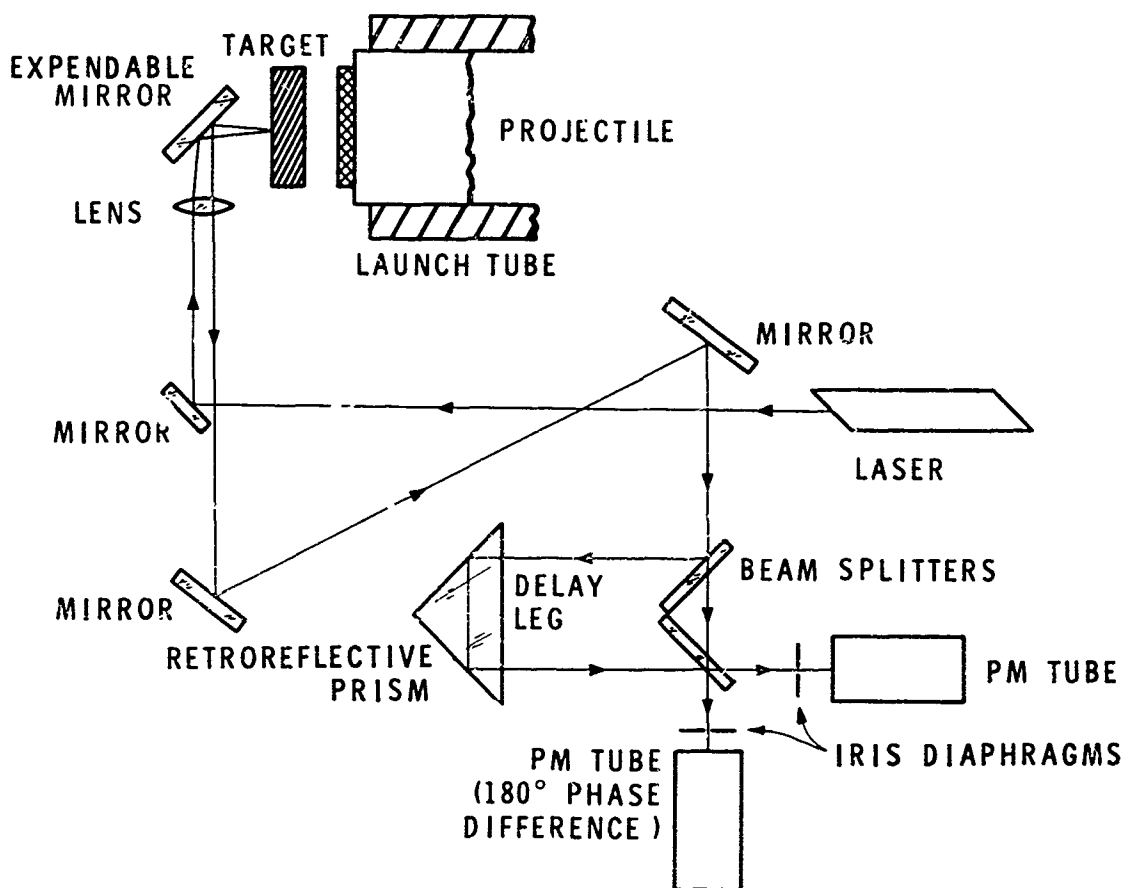


Figure 35 Laser Velocity Interferometer Schematic

MSL-70-12

The output of the photomultiplier tube is connected to Tektronix Type 519 and 454 oscilloscopes. A fringe pattern is developed by recombining the laser beam after the delay leg. This fringe pattern will change as the interface, from which the beam is reflected, moves. The number of fringes seen by the PM Tube per unit time is proportional to acceleration of this interface. The proportionality constant is controlled by the optical length of the delay leg. A target and projectile, instrumented for the laser velocity interferometer, is shown in Figure 36.



Figure 36 Projectile and Velocity Interferometer Target

MSL-70-12

Two shots were fired using quartz instrumentation and six using the laser velocity interferometer for wave profile measurement. Compressive wave behavior, release wave behavior, and wave attenuation in 2014-T6 aluminum were studied with these shots. On all but two shots the impactor was a fused quartz disk ( $\sim 1.5$  mm thick). A tungsten carbide impactor ( $\sim 1$  mm thick) was used for shots 9780 and 9781. The stress wave input into aluminum is shown schematically in Figure 37 for these two types of impactors. Fused quartz inputs a square stress pulse to the target, whereas tungsten carbide inputs a stepped stress pulse as the target is unloaded in discrete stress steps due to unloading waves reverberating back and forth in the impactor. This "reverberating buffer" technique has been described by Lysne.<sup>(23)</sup>

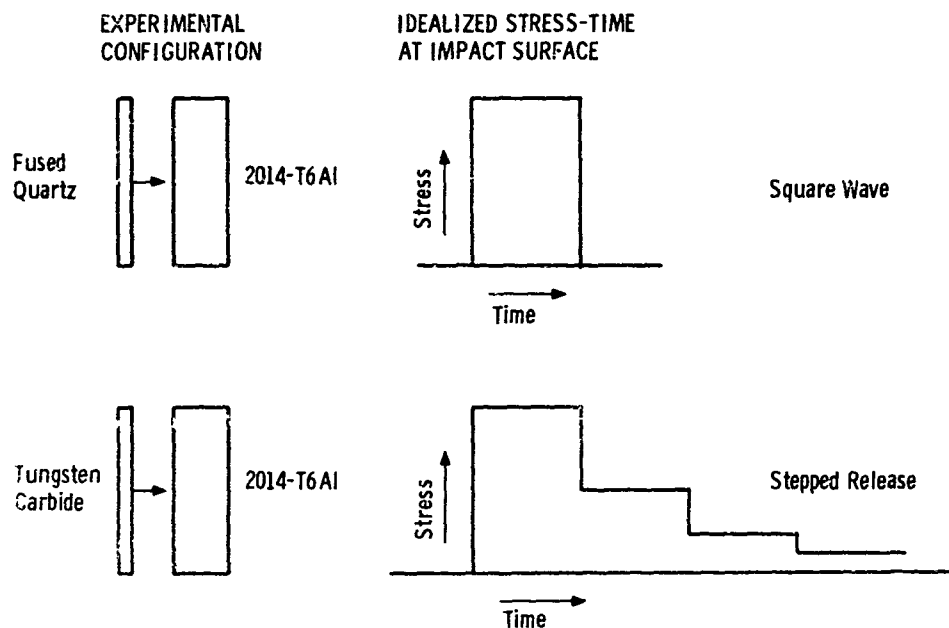


Figure 37 Stress Inputs for Wave Profile Studies

### 5. Spallation Wave Profile

Spall wave profile measurements were made on the 102 mm gun using the laser velocity interferometer. The configuration for these shots is shown in Figure 38. Aluminum was impacted onto aluminum with readout of free surface velocity at the rear surface of the target. Shots were fired below and above the incipient spall threshold for both loading times studied previously on the 63.5 mm gun. Impact velocity and tilt were recorded. Specimens were recovered and examined metallographically to determine the extent of fracture.

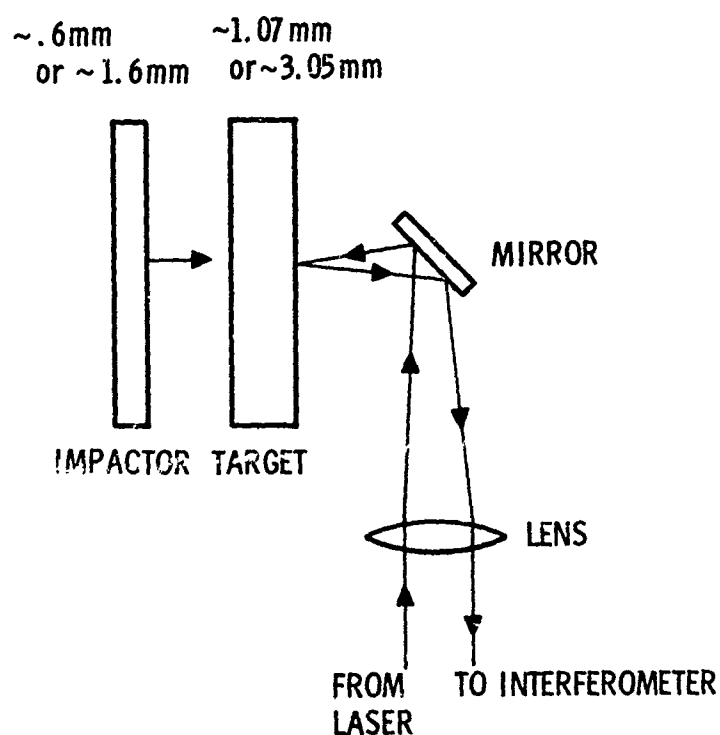


Figure 38 Schematic of Spall Wave Profile Shots



MSL-70-12

## RESULTS AND DISCUSSION

## 1. Elastic Constants

List of Symbols

$B^S$	Adiabatic bulk modulus
$B^T$	Isothermal bulk modulus
$C_L$	Longitudinal wave velocity
$C_p$	Heat capacity at constant pressure
$C_S$	Shear wave velocity
$P$	Hydrostatic pressure
$T$	Temperature
$\alpha$	Coefficient of linear expansion
$\beta$	Coefficient of volume expansion
$\gamma$	Gruneisen ratio
$\rho$	Density

Results of ultrasonic and density measurements on 2014-T6 aluminum, 12.7 mm stock, are listed in Table II. Pressure derivatives  $(\frac{\partial C_L}{\partial P})_T$  and  $(\frac{\partial C_S}{\partial P})_T$  have been corrected for length changes under hydrostatic pressure,  $(\frac{\partial C_L}{\partial T})_P$  and  $(\frac{\partial C_S}{\partial T})_P$  have been corrected to account for thermal expansion.

MSL-70-12

TABLE II  
RESULTS OF ULTRASONIC  
MEASUREMENTS ON 2014-T6 ALUMINUM

	UNITS	UNCORRECTED	CORRECTED *
$\left(\frac{\partial C_L}{\partial P}\right)_T$	$\frac{\text{mm}}{\mu\text{sec}} \cdot \frac{1}{\text{kbar}}$	0.0188	0.0158
$\left(\frac{\partial C_S}{\partial P}\right)_T$	$\frac{\text{mm}}{\mu\text{sec}} \cdot \frac{1}{\text{kbar}}$	0.0118	0.0103
$\left(\frac{\partial C_L}{\partial T}\right)_P$	$\frac{\text{mm}}{\mu\text{sec}} \cdot \frac{1}{^\circ\text{C}}$	$-10.6 \times 10^{-4}$	$-9.2 \times 10^{-4}$
$\left(\frac{\partial C_S}{\partial T}\right)_P$	$\frac{\text{mm}}{\mu\text{sec}} \cdot \frac{1}{^\circ\text{C}}$	$-7.8 \times 10^{-4}$	$-7.1 \times 10^{-4}$

	UNITS	WAVE VELOCITY AT 25°C AND 1 ATM
$C_L$	mm/ $\mu\text{sec}$	6.353
$C_S$	mm/ $\mu\text{sec}$	3.199
$\rho$	g/cm <sup>3</sup>	2.81

Derivatives evaluated at  
25°C and 1 atm.

\* Corrected for length changes.

MSL-70-12

Elastic moduli and their derivatives may be computed from quantities listed in Table II. This has been done for the bulk and shear moduli. The following equations were used for these calculations:

$$B^S = \rho (C_L^2 - \frac{4}{3} C_S^2) \quad (\text{III-1})$$

$$B^T = \frac{B^S}{1 + \beta \gamma T} \quad (\text{III-2})$$

$$\left(\frac{\partial B^S}{\partial P}\right)_T = 2\rho \left\{ C_L \left(\frac{\partial C_L}{\partial P}\right)_T - \frac{4}{3} C_S \left(\frac{\partial C_S}{\partial P}\right)_T \right\} + \frac{B^S}{B^T} \quad (\text{III-3})$$

$$\left(\frac{\partial B^S}{\partial T}\right)_P = 2\rho \left\{ C_L \left(\frac{\partial C_L}{\partial T}\right)_P - \frac{4}{3} C_S \left(\frac{\partial C_S}{\partial T}\right)_P \right\} - \beta B^S \quad (\text{III-4})$$

$$\left(\frac{\partial B^S}{\partial P}\right)_S = \left(\frac{\partial B^S}{\partial P}\right)_T + \left(\frac{\partial B^S}{\partial T}\right)_P \frac{T\gamma}{B^S} \quad (\text{III-5})$$

$$\left(\frac{\partial B^S}{\partial T}\right)_S = \frac{B^S}{T\gamma} \left(\frac{\partial B^S}{\partial P}\right)_T + \left(\frac{\partial B^S}{\partial T}\right)_P \quad (\text{III-6})$$

$$\begin{aligned} \left(\frac{\partial B^T}{\partial P}\right)_T &= \left(\frac{\partial B^S}{\partial P}\right)_T + \beta \gamma T \frac{B^T}{B^S} \left\{ 1 - \frac{2}{\beta B^T} \left(\frac{\partial B^T}{\partial T}\right)_P - 2 \left(\frac{\partial B^S}{\partial P}\right)_T \right\} \\ &\quad + \left(\beta \gamma T \frac{B^T}{B^S}\right)^2 \left\{ \left(\frac{\partial B^S}{\partial P}\right)_T - 1 - \frac{1}{\beta^2} \left(\frac{\partial \beta}{\partial T}\right) \right\} \end{aligned} \quad (\text{III-7})$$

$$\left(\frac{\partial B^T}{\partial T}\right)_P = \frac{B^T}{B^S} \left(\frac{\partial B^S}{\partial T}\right)_P - \left(\frac{B^T}{B^S}\right)^2 B^S \left\{ \gamma T \left(\frac{\partial \beta}{\partial T}\right)_P + \beta \gamma \right\} \quad (\text{III-8})$$

MSL-70-12

$$\left(\frac{\partial B^T}{\partial P}\right)_S = \left(\frac{\partial B^T}{\partial P}\right)_T + \left(\frac{\partial B^T}{\partial T}\right)_P \frac{T\gamma}{B^S} \quad (\text{III-9})$$

$$\left(\frac{\partial B^T}{\partial T}\right)_S = \frac{B^S}{T\gamma} \left(\frac{\partial B^T}{\partial P}\right)_T + \left(\frac{\partial B^T}{\partial T}\right)_P \quad (\text{III-10})$$

$$G = C_S^2 \rho = G^S = G^T \quad (\text{III-11})$$

$$\left(\frac{\partial G}{\partial T}\right)_P = G \left\{ \frac{2}{C_S} \left(\frac{\partial C_S}{\partial T}\right)_P - \beta \right\} \quad (\text{III-12})$$

$$\left(\frac{\partial G}{\partial P}\right)_T = G \left\{ \frac{2}{C_S} \left(\frac{\partial C_S}{\partial P}\right)_T + \frac{1}{B^T} \right\} \quad (\text{III-13})$$

$$\left(\frac{\partial G}{\partial P}\right)_S = \left(\frac{\partial G}{\partial P}\right)_T + \frac{T\gamma}{B^S} \left(\frac{\partial G}{\partial T}\right)_P \quad (\text{III-14})$$

$$\left(\frac{\partial G}{\partial T}\right)_S = \left(\frac{\partial G}{\partial T}\right)_P + \frac{B^S}{T\gamma} \left(\frac{\partial G}{\partial P}\right)_T \quad (\text{III-15})$$

Values for the above quantities are given in Table III, all derivatives listed were evaluated at  $T = 20^\circ\text{C}$  and  $P = 0$  kilobars. In calculating these quantities, values given below were used for  $\beta$  and  $\gamma$ . The volume coefficient of expansion,  $\beta$ , was taken as<sup>(24)</sup>

$$\beta = 3\alpha = (64.2 + 0.039T) \times 10^{-6}/^\circ\text{C} \quad (\text{III-16})$$

The Gruneisen ratio,  $\gamma$ , was calculated as

$$\gamma = 1.81 \quad (\text{III-17})$$

MSL-70-12

from the relation

$$\gamma = \frac{\beta B^S}{\rho C_P} \quad (\text{III-18})$$

with  $B^S$  taken from Table III and  $C_P = 0.23 \text{ cal/g-}^\circ\text{C}$ . (24)

TABLE III  
ELASTIC CONSTANTS FOR 2014-T6 AL  
( $P = 0$ ,  $T = 25^\circ\text{C}$ )

PARAMETER	VALUE
$B^S$	751 kbar
$(\frac{\partial B^S}{\partial P})_T$	4.23
$(\frac{\partial B^S}{\partial T})_P$	-0.207 kbar/ $^\circ\text{C}$
$(\frac{\partial B^S}{\partial P})_S$	4.08
$(\frac{\partial B^S}{\partial T})_S$	5.68 kbar/ $^\circ\text{C}$
$B^T$	725 kbar
$(\frac{\partial B^T}{\partial P})_T$	4.40
$(\frac{\partial B^T}{\partial T})_P$	-0.296 kbar/ $^\circ\text{C}$
$(\frac{\partial B^T}{\partial P})_S$	4.18
$(\frac{\partial B^T}{\partial T})_S$	5.82 kbar/ $^\circ\text{C}$
$G$	288 kbar
$(\frac{\partial G}{\partial P})_T$	2.25
$(\frac{\partial G}{\partial T})_P$	-0.147 kbar/ $^\circ\text{C}$
$(\frac{\partial G}{\partial P})_S$	2.15
$(\frac{\partial G}{\partial T})_S$	2.99 kbar/ $^\circ\text{C}$

MSL-70-12

Several different equations of state may be computed from the moduli and derivatives of moduli listed in Table III. In the discussion that follows, isotherm, adiabat and hugoniot calculations are made from the Murnaghan or logarithmic equation of state, for which pressure along an isotherm is given by

$$P_T = \frac{B^T}{\left(\frac{\partial B^T}{\partial P}\right)_T} \left\{ \left(\frac{V_0}{V}\right) \left(\frac{\partial B^T}{\partial P}\right)_T - 1 \right\} \quad (\text{III-19})$$

pressure along an adiabat is given by

$$P_S = \frac{B^S}{\left(\frac{\partial B^S}{\partial P}\right)_S} \left\{ \left(\frac{V_0}{V}\right) \left(\frac{\partial B^S}{\partial P}\right)_S - 1 \right\} \quad (\text{III-20})$$

and hydrostatic pressure along the hugoniot, i.e. shock hydrostat, is given by

$$P_H = P_S + \frac{\gamma_B^S}{12} \left\{ \left(\frac{\partial B^S}{\partial P}\right)_S + 1 \right\} \left(1 - \frac{V}{V_0}\right)^3 \quad (\text{III-21})$$

Equations of state, calculated from Eqs. (III-19), (III-20) and (III-21) are presented in Figure 39 for 2014-T6 aluminum.

For pressures up to 50 kilobars the hugoniot calculated from Eq. (III-21) lies within 0.2% of the adiabat, whereas the separation between the adiabat and isotherm is ~ 3%. The conversion to particle velocity from volume was made using

MSL-70-12

$$u = \left\{ \frac{\frac{P}{\rho} \frac{V_0 - V}{V}}{1 + \frac{V_0 - V}{V}} \right\}^{1/2} \quad (\text{III-22})$$

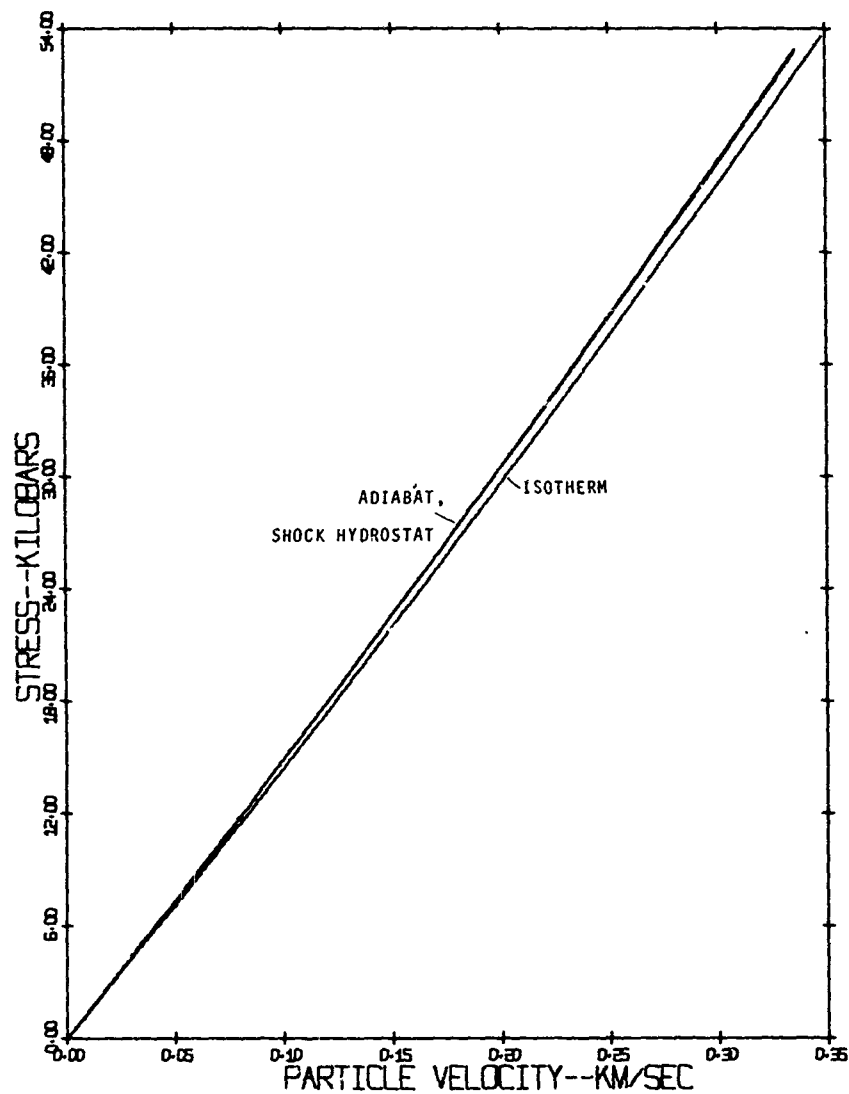


Figure 39 Isotherm, Adiabatic and Shock Hydrostat  
Calculated for 2014-T6 Aluminum

## 2. Spallation Threshold

Spall fracture characteristics of 2014-T6 aluminum are summarized in Table IV and shown in Figures 40, 41 and 42.

Two loading times were studied corresponding to impactor thicknesses of  $\sim 0.6$  mm (0.19  $\mu$ sec pulse duration) and  $\sim 1.6$  mm (0.5  $\mu$ sec pulse duration). Spall fracture characteristics are shown in Figure 40 for the 0.6 mm impactor series and in Figure 41 for the 1.6 mm impactor series. Spall fractures for each follow the direction of grain elongation although there is a tendency for cracks to link up at right angles to this direction. Incipient spall thresholds were estimated as 0.216 mm/ $\mu$ sec and 0.180 mm/ $\mu$ sec respectively for these two impactor series.

TABLE IV  
SPALL RESULTS FOR 2014-T6 ALUMINUM

Shot No.	Velocity (mm/ $\mu$ sec)	Spall	Projectile Thickness (mm)	Target Thickness (mm)
115	.237	○	1.59	3.04
102	.200	●	1.57	3.06
107	.183	○	1.58	3.03
106	.180	⊗	1.57	3.04
104	.170	●	1.57	3.05
105	.164	○	1.59	3.05
114	.270	●	0.605	1.067
109	.247	●	0.597	1.072
110	.242	●	0.597	1.069
111	.216	⊗	0.607	1.069
112	.190	○	0.605	1.072
113	.170	○	0.605	1.067

- Complete Separation
- Above Incipient
- ⊗ Incipient Spall Threshold
- Below Incipient
- No Spall Fracture Visible at 40X



MSL-70-12

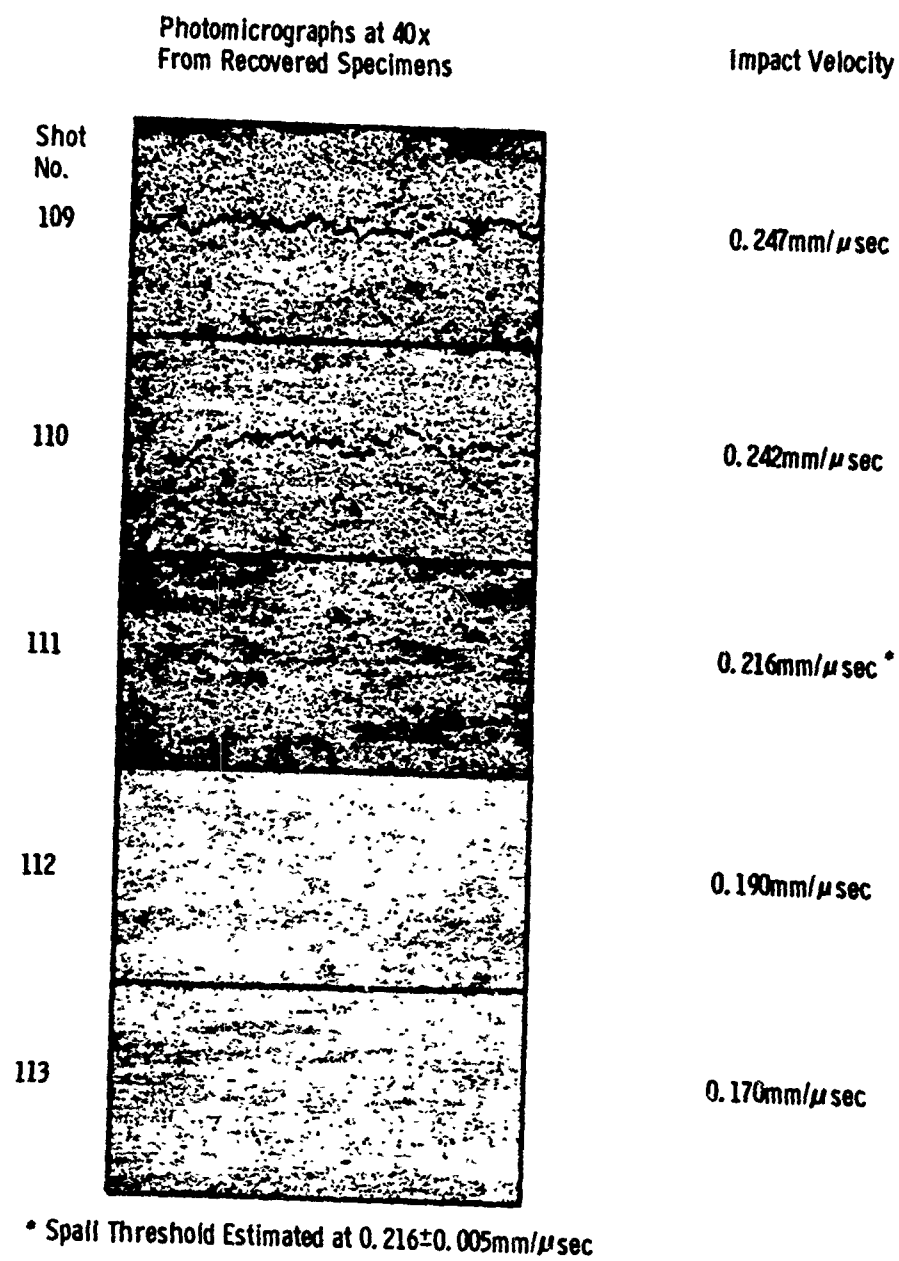


Figure 40 Metallographs of Spall Fracture in  
2014-T6 Aluminum, 0.6 mm Impactor

MSL-70-12

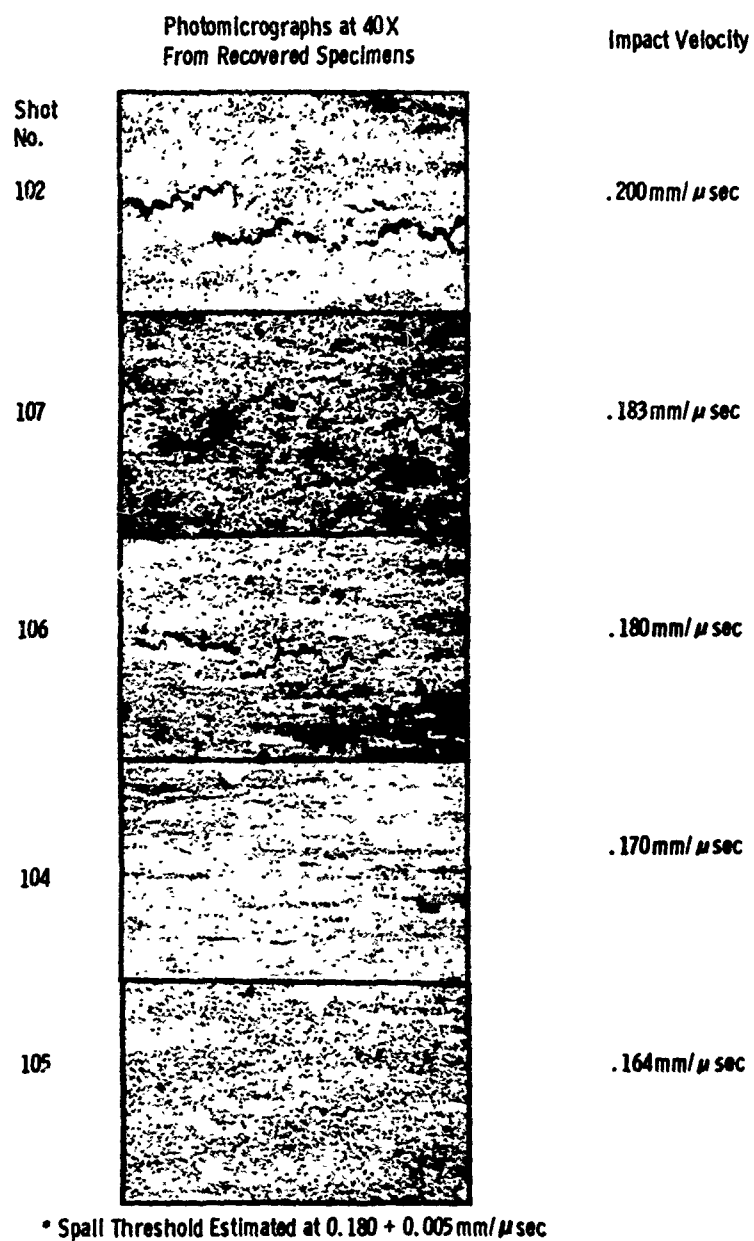


Figure 41 Metallography of Spall Fractures in  
2014-T6 Aluminum, 1.6 mm Impactor

MSL-70-12

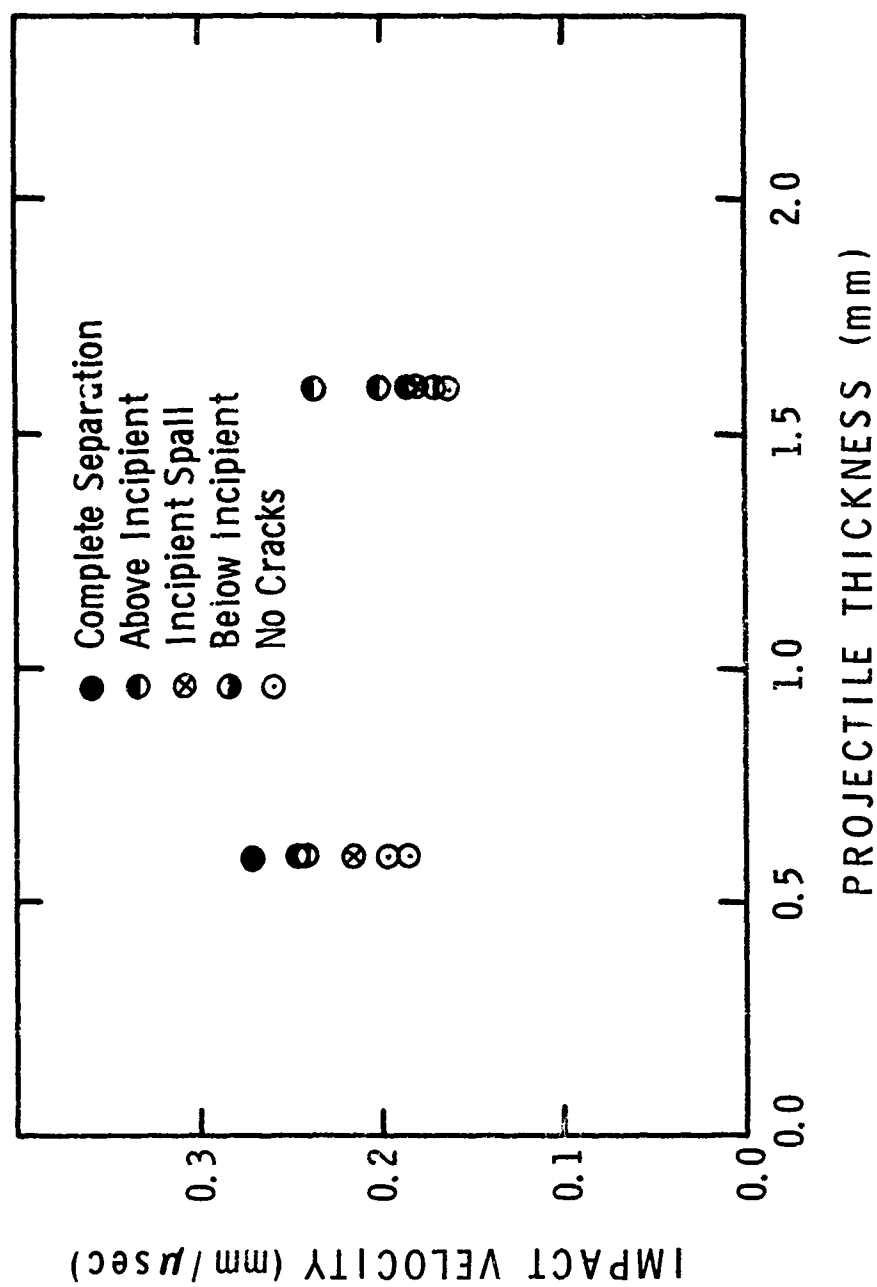


Figure 42 Spall Results for 2014-T6 Aluminum

MSL-70-12

### 3. Hugoniot

Results of four hugoniot shots are shown in Figure 43 and 44.

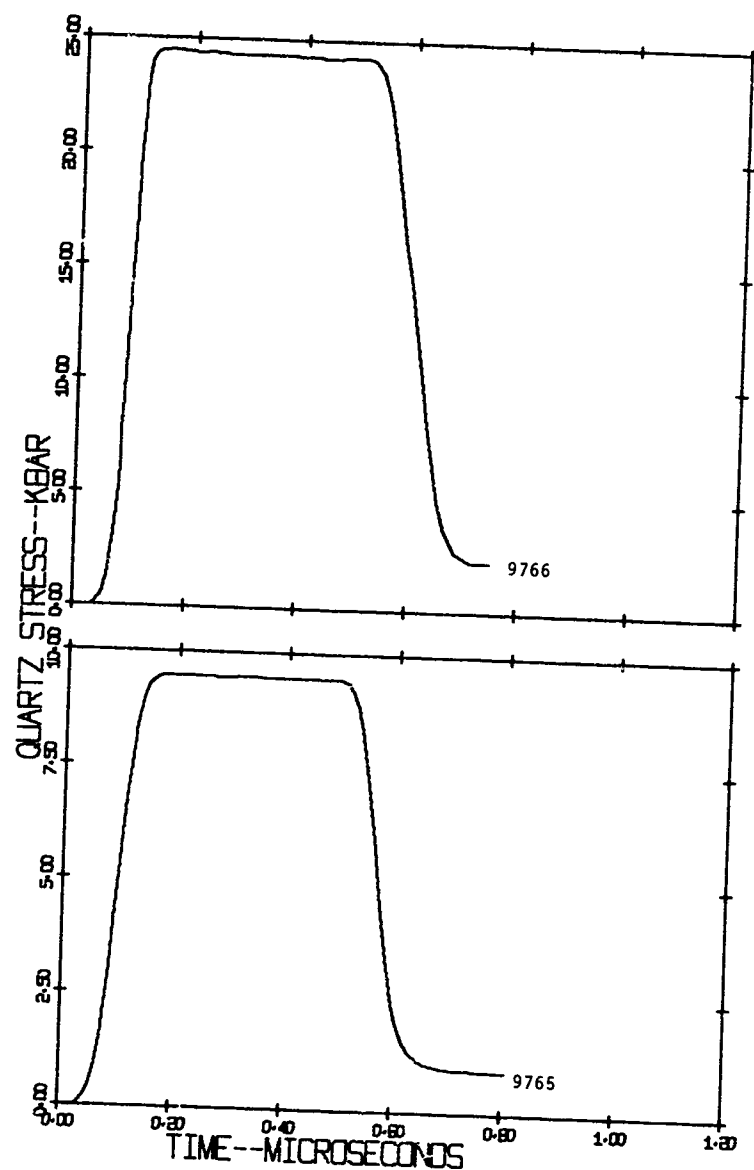


Figure 43 Results from Direct Impact Shots

MSL-70-12

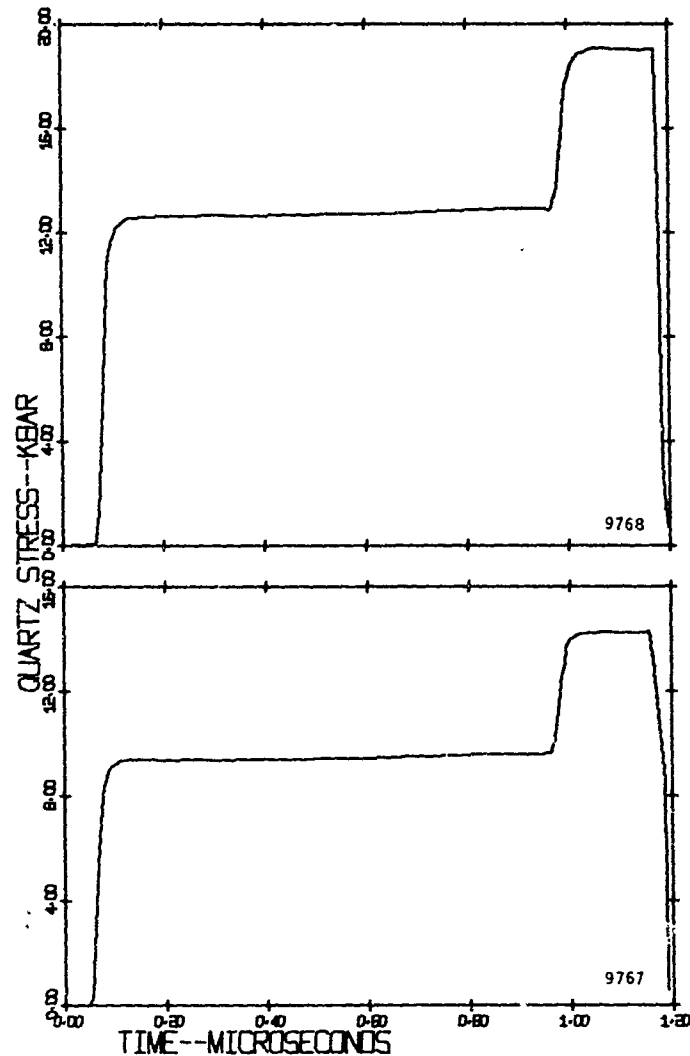


Figure 44 Results from Buffered Direct Impact Shots

Film records from these shots, along with two other quartz gauge records discussed in the wave profile section which follows, were reduced to quartz stress-time using "QZ", a program for quartz gauge analysis.<sup>(25)</sup> Hugoniot points were then computed using appropriate quartz stresses and impact velocities for shots presented in Figures 43 and 44. The following equations were used for these Hugoniot computations:

MSL-70-12

Known quantities

$V_I$  = impact velocity

$\sigma_q$  = stress measured for quartz.

For direct impact

$$\sigma_{Al} = \sigma_q \quad (\text{III-23})$$

$$u_{Al} = V_I - \frac{\sigma_q}{Z_q} \quad (\text{III-24})$$

For buffered direct impact

$$\sigma_{Al} = 1/2 [\sigma_q + Z_b u_q] \quad (\text{III-25})$$

$$u_{Al} = V_I - \frac{\sigma_q + Z_b u_q}{2Z_b} \quad (\text{III-26})$$

where

$\sigma_{Al}$  = stress at hugoniot point

$u_{Al}$  = particle velocity at hugoniot point

$$Z_q = \rho_q U_q$$

$$\rho_q = 2.65 \text{ g/cm}^3$$

$$u_q = A + B\sigma_q$$

$$A = 5.74 \frac{\text{mm}}{\mu\text{sec}}$$

$$B = -0.00092 \frac{\text{mm}}{\mu\text{sec-kbar}}$$

$$Z_b = \rho_b C_b$$

$$\rho_b = 14.9 \text{ g/cm}^3$$

$$C_b = 6.92 \text{ mm}/\mu\text{sec}$$

$$\sigma_q < 25 \text{ kilobars}$$

tungsten carbide

MSL-70-12

Results of the above computations are listed in Table V.

TABLE V  
HUGONIOT DATA FOR 2014-T6 ALUMINUM

Shot No.	Impact Velocity (mm/μsec)	Quartz σ (kbar)	2014-T6 Al	
			σ (kbar)	u (mm/μsec)
9765	0.117	9.2	9.2	0.056
9766	0.311	24.5	24.5	0.149
9767	0.261	9.4	36.6	0.225
9768	0.349	12.5	48.7	0.302

Probable error is 2% for direct impact results and 3% for buffered direct impact results. This is computed as follows:

Direct Impact

$$\frac{\Delta \sigma_{Al}}{\sigma_{Al}} = \frac{\Delta \sigma_q}{\sigma_q} = 0.01$$

$$\frac{\Delta u_{Al}}{u_{Al}} = \sqrt{\left(\frac{V_I}{u_{Al}}\right)^2 \left(\frac{\Delta V_I}{V_I}\right)^2 + \left(\frac{\sigma_q}{\sigma_{Al}}\right)^2 \left[\left(\frac{\Delta \sigma_q}{\sigma_q}\right)^2 + \left(\frac{\Delta u_q}{u_q}\right)^2\right]}$$

$$\frac{\Delta u_{Al}}{u_{Al}} \sim \sqrt{(2)^2 (.005)^2 + (1)^2 [(.002)^2 + (.01)^2]} = 0.014$$

$$\text{Probable Error} = \left[ \sqrt{(.01)^2 + (.014)^2} \right] \times 100 = 1.7\%$$

MSL-70-12

## Buffered Direct Impact

$$\frac{\Delta\sigma_{A1}}{\sigma_{A1}} = \sqrt{\left(\frac{\sigma_q}{\sigma_{A1}}\right)^2 \left(\frac{\Delta\sigma_q}{\sigma_q}\right)^2 + \left(\frac{z_b u_q}{\sigma_{A1}}\right)^2 \left[\left(\frac{\Delta z_b}{z_b}\right)^2 + \left(\frac{\Delta u_q}{u_q}\right)^2\right]}$$

$$\frac{\Delta\sigma_{A1}}{\sigma_{A1}} \sim \sqrt{(1)^2 (.01)^2 + (1)^2 [(.02)^2 + (.01)^2]} = 0.025$$

$$\frac{\Delta u_{A1}}{u_{A1}} = \sqrt{\left(\frac{v_I}{u_{A1}}\right)^2 \left(\frac{\Delta v_I}{v_I}\right)^2 + \left(\frac{\sigma_q}{2z_b u_{A1}}\right)^2 \left[\left(\frac{\Delta\sigma_q}{\sigma_q}\right)^2 + \left(\frac{\Delta z_b}{z_b}\right)^2\right] + \frac{\left(\frac{u_q}{2u_{A1}}\right)^2 \left(\frac{\Delta u_q}{u_q}\right)^2}{\left(\frac{u_q}{2u_{A1}}\right)^2 \left(\frac{\Delta u_q}{u_q}\right)^2}}$$

$$\frac{\Delta u_{A1}}{u_{A1}} \sim \sqrt{(2)^2 (.005)^2 + (.25)^2 [(.01)^2 + (.02)^2] + (1)^2 (.01)^2} = 0.015$$

$$\text{Probable error} = \left[ \sqrt{(.025)^2 + (.015)^2} \right] \times 100 = 2.9\%$$

A linear curve fit to hugoniot data on 2014-T6 aluminum results in

$$\sigma = 0.37 + 160 u \quad (\text{III-27})$$

for  $9 < \sigma < 50$  kilobars

where  $\sigma$  is hugoniot stress (kilobars), and  $u$  is particle velocity (mm/ $\mu$ sec). In Figure 45 this fit is compared to measured hugoniot data, an acoustic line given by

$$\sigma = \rho_0 C_L u = 179 u \quad (\text{III-28})$$



MSL-70-12

and a range for  $\sigma_{HEL}$  taken from Figure 50 which is discussed later.

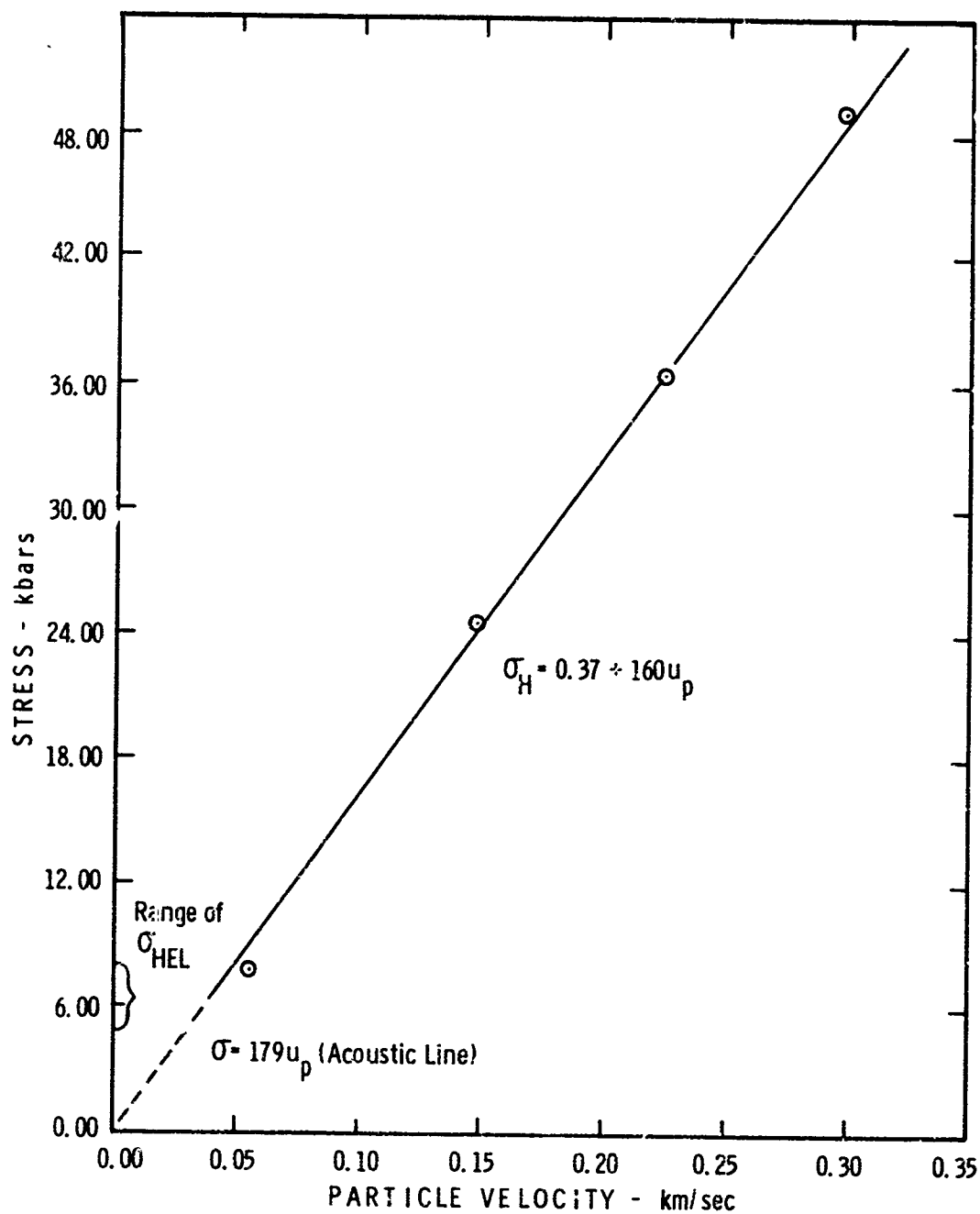


Figure 45 Hugoniot of 2014-T6 Aluminum to 50 Kilobars

This hugoniot may be compared to the hugoniot hydrostat from elastic constants (Figure 39). For an elastic-perfectly plastic material, the hugoniot will lie  $\sim 1/3 Y$  above the hydrostat in the stress-particle velocity plane, where  $Y$  is the yield stress measured under uniaxial stress conditions. Thus, this amount may be subtracted from the experimental hugoniot, above the precursor elastic limit, to obtain the hydrostat. Using appropriate values for 2014-T6 aluminum, we find that the experimental hydrostat lies  $\sim 1\%$  above the hydrostat calculated from elastic constants.

#### 4. Wave Profiles

Wave profiles were measured using both quartz transducers and the laser velocity interferometer. Quartz data was first reduced to interface stress-time between the aluminum target and the quartz gauge. Interferometer data was first reduced to interface velocity-time using an analysis similar to that reported by Barker.<sup>(22)</sup> Interface velocity and interface stress were then reduced to stress states in aluminum using standard impedance matching procedures.<sup>(26)</sup>

Transmitted wave profiles, measured using quartz, are presented in Figure 46 for a propagation distance of  $\sim 3$  mm and impact velocities of 0.125 and 0.432 mm/ $\mu$ sec. A  $\sim 1.5$  mm fused quartz impactor was used for both of these shots. The lower stress shot (9769) showed a peak stress level of  $\sim 9$  kilobars. This peak stress is just above the elastic limit,  $4.5 < \sigma_{HEL} < 10$  kilobars, and no separation of elastic and plastic waves is visible on the record; however, there is a substantial amount of ramping on top of the wave. We do not completely understand why the risetime is so poor on shot (9769),  $\sim 0.05$   $\mu$ sec. This amount is about twice the risetime that can be accounted for due to impact tilt.

MSL-70-12

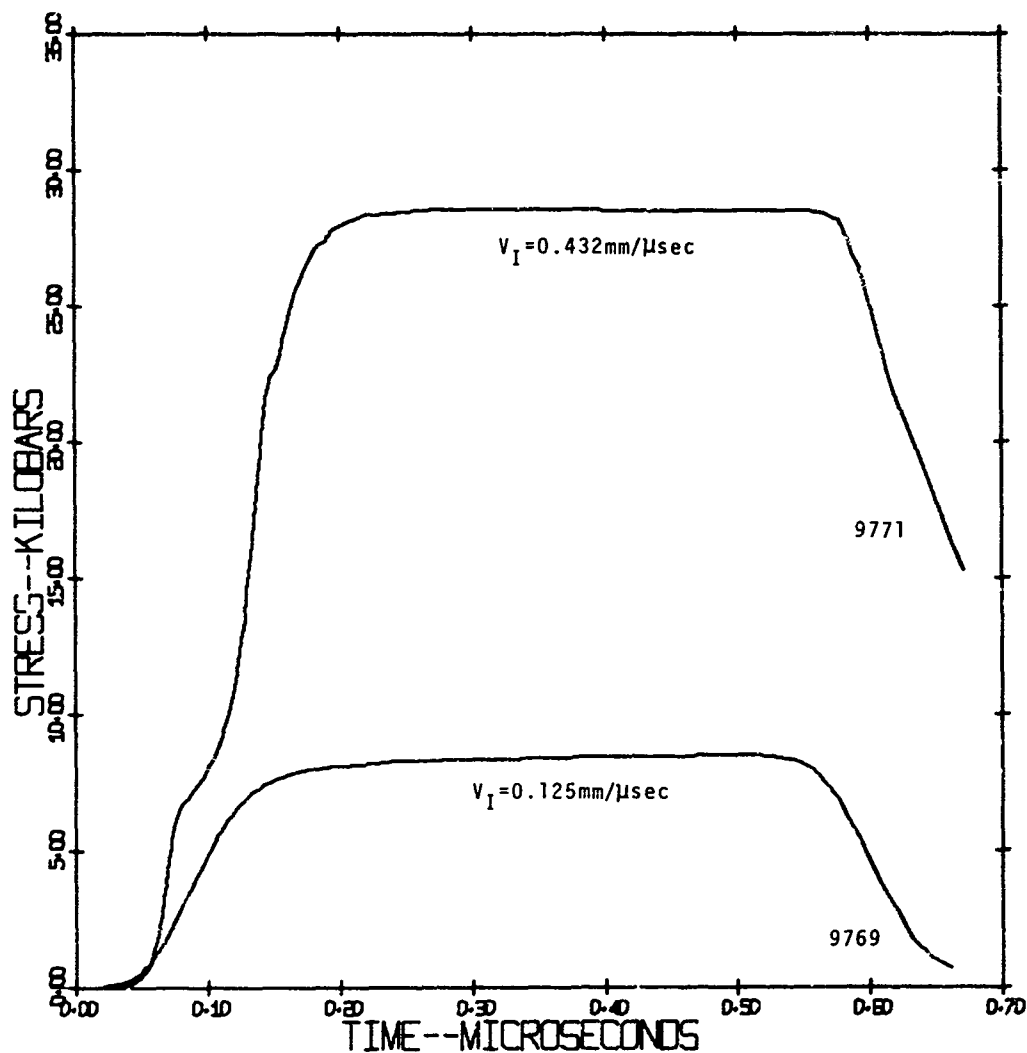


Figure 46 Wave Profiles in 2014-T6 Aluminum at a Propagation Distance of  $\sim 3$  mm (Fused Quartz Impactors)

The higher impact velocity shot (9771) does show elastic-plastic effects. The elastic wave has an amplitude of about 6 kilobars. At  $\sim 23$  kilobars there is a perturbation in the plastic wave front. This perturbation seems too high on the wave to be caused by wave interactions resulting from the impedance mismatch at the quartz gauge and at present this perturbation is not understood.

Transmitted wave profiles measured using the laser velocity interferometer are shown in Figures 47 and 49. In Figure 47 profiles are shown after propagation distances of  $\sim 1, 3, 6.5$ , and  $12$  mm for an impact stress of  $\sim 20$  kilobars. Fused quartz impactors were used for this series which shows development of elastic, plastic, and release waves in 2014-T6 aluminum with propagation distance. Several significant features may be noted: elastic precursor decay with propagation distance, spreading of the plastic wave, and spreading of the release wave.

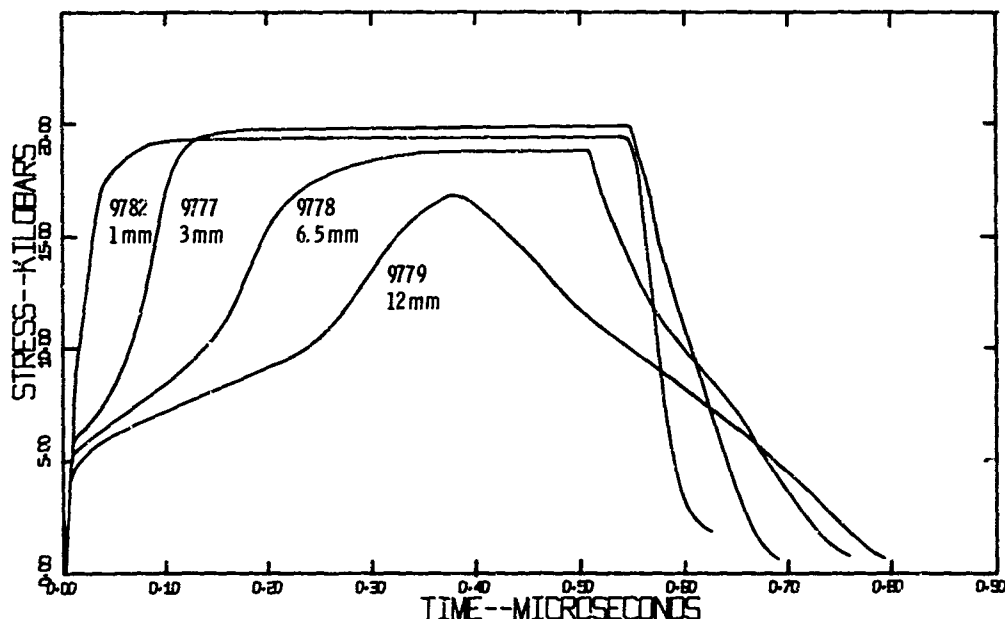


Figure 47 Wave Profiles in 2014-T6 Aluminum for an Average Impact Velocity of  $0.284$  mm/ $\mu$ sec and Propagation Distances of  $\sim 1, 3, 6.5$ , and  $12$  mm (Fused Quartz Impactors)

Wave spreading with propagation distance is best shown by plotting "phase lines", e.g., lines of constant stress in the  $x$ - $t$  plane. An  $x$ - $t$  plot, Figure 48, was constructed from pro-

MSL-70-12

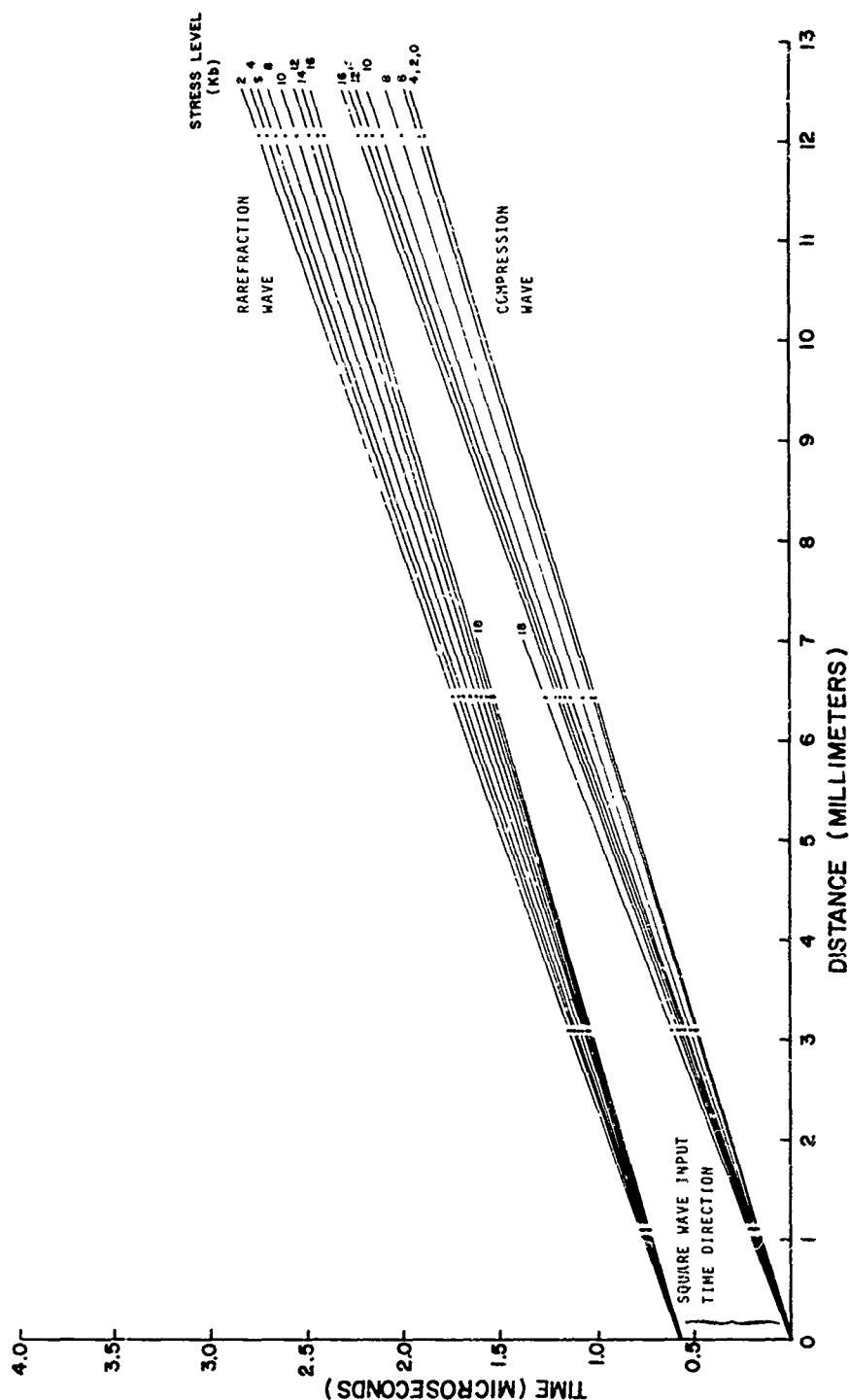


Figure 48 Compressive and Rarefaction Wave Characteristics for a Peak Stress of 20 Kilobars and ~1.5 mm (Fused Quartz Impactor)

files presented in Figure 47 for both the compression and rarefaction waves. If phase lines are straight, then wave propagation is steady-state. Note that steady-state conditions are approached after  $\sim 12$  mm for the compressive wave front as the "phase lines" become parallel, straight lines. Separation of elastic and plastic waves is clearly visible in these loading phase lines; this is shown as a gap between phase lines in the 6 to 10 kilobar range. This gap broadens with propagation distance.

In Figure 48 the rarefaction phase lines are seen to fan out from the impact surface. There is slight evidence of an elastic-plastic type release. This is visible as a broadening of phase line separation towards the middle of this release wave fan.

Although not carried out here, analytic forms of loading and unloading phase lines are very useful for predicting wave attenuation with propagation distance. Shot 9779 in Figure 47 is an example of an attenuated wave profile, which occurs when loading and release phase lines overlap in the  $x-t$  plane.

In Figure 49 the compressive wave is shown as a function of compressive stress. Note that increasing peak stress from 38 to 48 kilobars changes the precursor very little. Further, with this increase, the elastic-plastic wave separation and plastic wave risetime are changed only slightly.

Elastic precursor amplitudes are summarized in Table VI for 2014-T6 aluminum. Figure 50 is a plot of these data for  $\sim 20$  kilobar impact stress. Bars attached to these data represent the uncertainty in identifying amplitudes due to the rounded nature of the precursor.

MSL-70-12

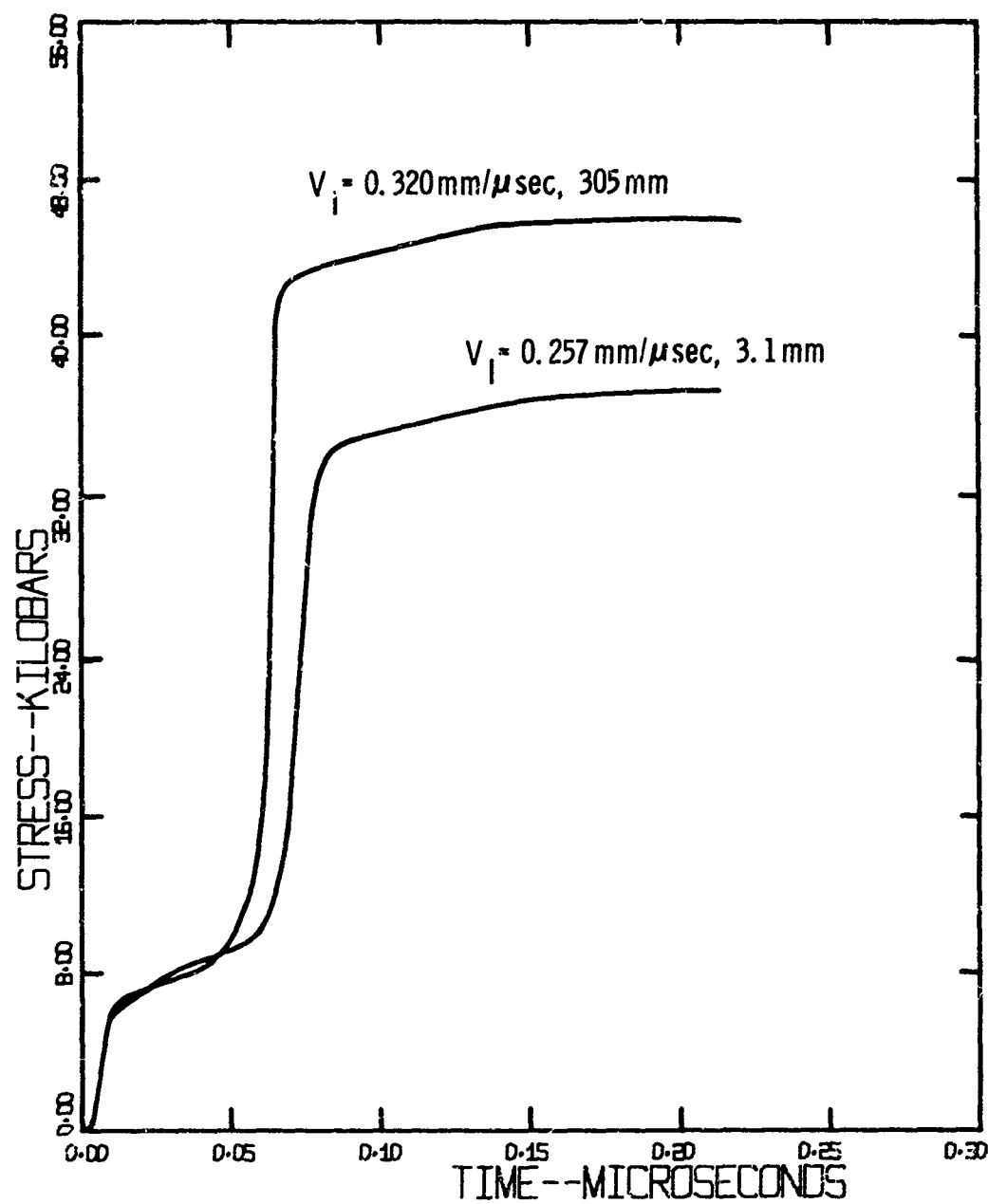


Figure 49 Wave Profiles in 2014-T6 Aluminum for a Propagation Distance of  $\sim 3 \text{ mm}$  and Two Peak Stress Levels (Tungsten Carbide Impactors)

TABLE VI  
SUMMARY OF ELASTIC PRECURSOR AMPLITUDES

Shot No.	Impact Stress (kbar)	Precursor Amplitude (kbar)	Propagation Distance (mm)
9782	20	$8.0 \pm .5$	1.11
9777	20	$6.5 \pm .5$	3.08
9778	20	$5.5 \pm .5$	6.42
9779	20	$4.5 \pm .5$	12.04
9780	38	$6.0 \pm .5$	3.10
9781	48	$6.0 \pm .5$	3.05
9771	30	$6.0 \pm .5$	3.07

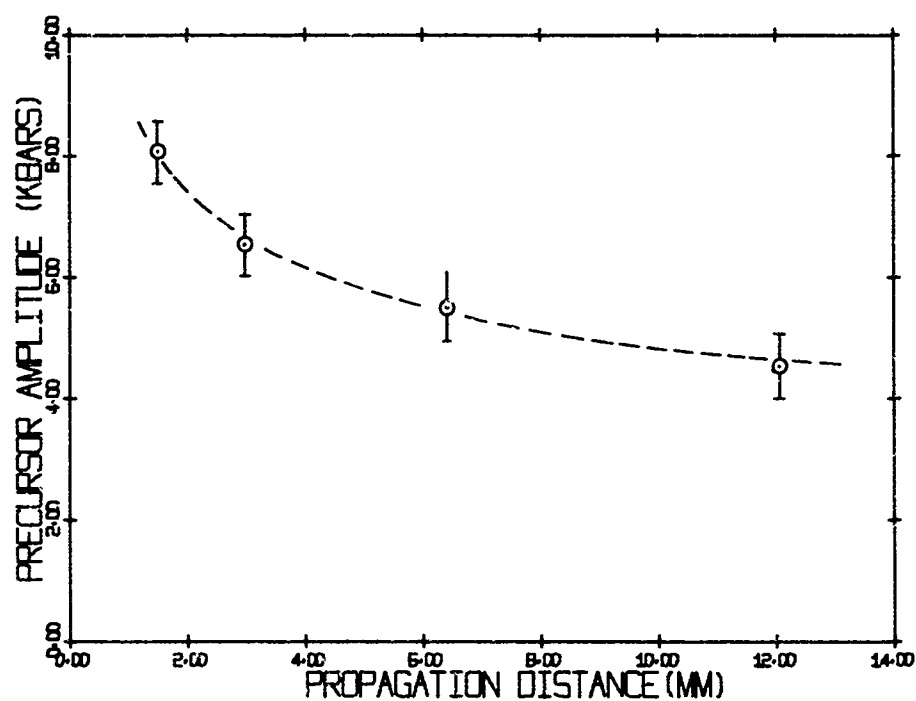


Figure 50 Elastic Precursor Decay in 2014-T6 Aluminum for a 20 Kilobar Impact Stress



MSL-70-12

## SPALLATION WAVE PROFILES

In order to explain significant features of measured wave profiles, wave interactions are first illustrated in Figure 51. Several simplifying assumptions are made. The shock is shown as a single wave rather than an elastic-plastic wave system, and small interactions between shock waves have been omitted. Fracture of the material is assumed to occur along a single surface (spall plane) rather than in a volume around this plane (Figures 40 and 41). Wave interactions at the spall plane are shown as if the material exhibits a time dependent fracture, i.e., the percentage of fractured area in the spall plane increases with time until the entire spall surface has separated. During the early stages of the fracture process, before complete separation is achieved, waves crossing the spall plane are partially transmitted and partially reflected. After complete separation has occurred, any waves trapped in the spalled piece will reverberate, giving a decaying, sinusoidal motion to the rear surface as the wave is damped by viscous forces.

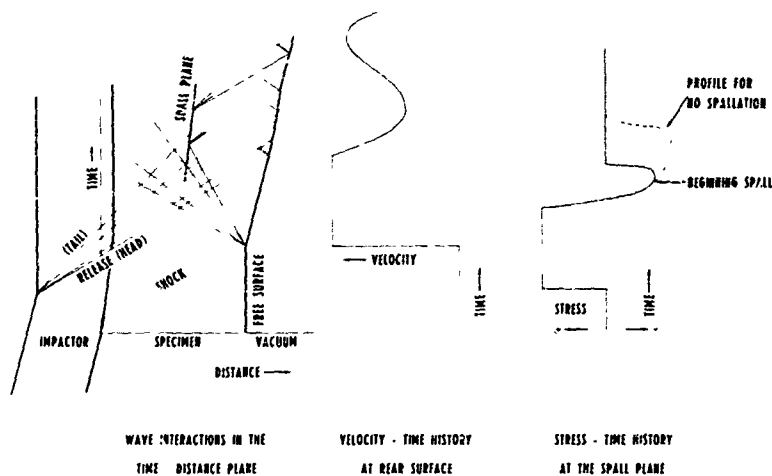


Figure 51 Wave Interactions at Spall Plane and Resultant Velocity-Time and Stress-Time Histories at Free Rear Surface

Details of the free surface motion of an aluminum impactor striking an aluminum target are shown in Figures 52 and 53. The wave front exhibits elastic-plastic flow as there is a break at about  $0.1 \text{ mm}/\mu\text{sec}$  (Figures 52 and 53). This corresponds to an elastic wave of approximately 7 kbars proceeding the plastic waves. The plastic wave ramps towards a final velocity which remains constant until rarefactions originating from the free rear surface of the impactor arrive and decrease the velocity of the surface. For tests in which no spall occurs, this decrease continues until the velocity is returned nearly to zero, e.g., lower trace in Figure 53.

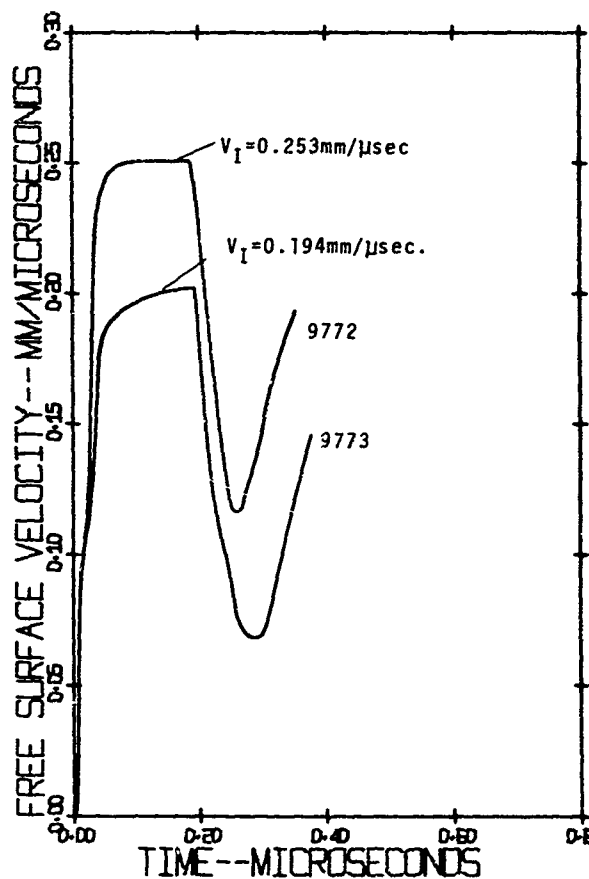


Figure 52 Spall Wave Profiles for 0.6 mm Impactor Series

MSL-70-12

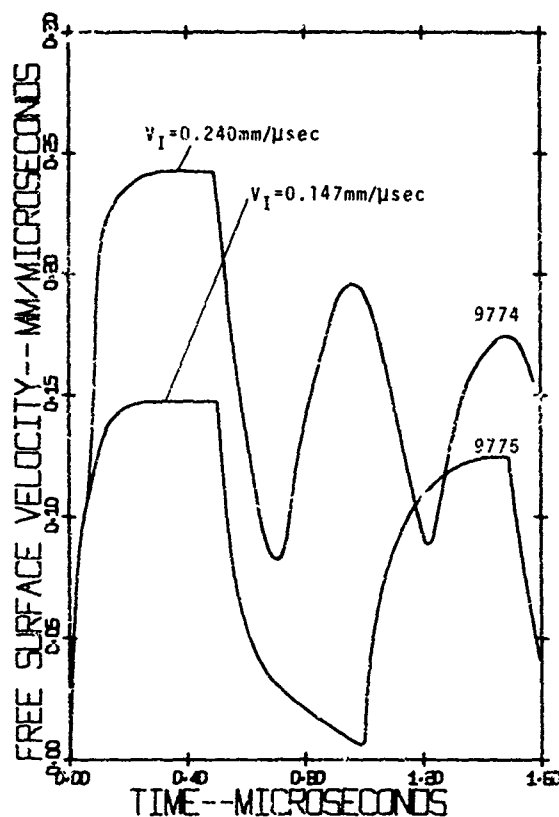


Figure 53 Spall Wave Profiles for 1.6 mm Impactor Series

Evidence of fracture in and about the spall plane is shown as a reversal in the velocity of the surface at approximately .26 microseconds in Figure 52 and .7 microseconds on the upper trace in Figure 53. Signals from fractured surfaces reach the rear surface with components of velocity opposite in sign to the rarefaction waves. As fracturing progresses, the surface is no longer "pulled back" by the release wave system, but accelerates, only to be decelerated again as the entrapped wave reverberates back and forth between the spall surface and the specimen rear surface. If it is assumed that the decrease of the free surface velocity to the point of reversal (referred

to as "pullback") is related to the maximum tensile stress at the spall plane, a quantitative measure of the negative stress required to fracture the material for a given wave shape is provided by the profile. The functional form of the relationship between the maximum tensile stress and pullback has not been firmly established, but attempts to correlate experimental results with calculations of spall plane stress have resulted in the following: (27)

$$\sigma_t = \rho C \frac{\Delta V}{2} \quad (\text{III-29})$$

where  $\sigma_t$  is maximum tensile stress at the spall plane,  $\rho$  and  $C$  are local density and dilatational wave velocity, and  $\Delta V$  is pullback.

Using this relation gives  $\sigma_t \sim 12$  kilobars for the thin impactor series and  $\sim 15$  kilobars for the thick impactor series. This behavior is backwards from results reported earlier for 6061-T6 aluminum. For 6061-T6 aluminum pullback was smallest for the thinner impactor series. Reasons for this difference are not understood at this time.

#### COMPARISON OF SHOCK PROPAGATION AND FRACTURE CHARACTERISTICS OF 2014-T6 AND 6061-T6 ALUMINUM (28,29)

##### 1. Elastic Constants

The elastic constants and derivatives of elastic constants of 2014-T6 aluminum and 6061-T6 aluminum are compared in Table VII. In Figure 54 comparison is made between the hugoniot hydrostat for these two alloys as calculated from Eqs. III-19, III-20, III-21 and III-22 using some of the values listed in Table VII. These calculated hugoniots differ by  $\sim 3\%$  at 50 kilobars.

MSL-70-12

TABLE VII  
COMPARISON OF ELASTIC CONSTANTS  
FOR 2014-T6 AND 6061-T6 ALUMINUM

PARAMETER	VALUE	
	2014-T6 Al	6061-T6 Al
$B^S$	751 kbar	728 kbar
$(\frac{\partial B^S}{\partial P})_T$	4.23	4.75
$G$	288 kbar	276 kbar
$(\frac{\partial G}{\partial P})_T$	2.25	2.25

MSL-70-12

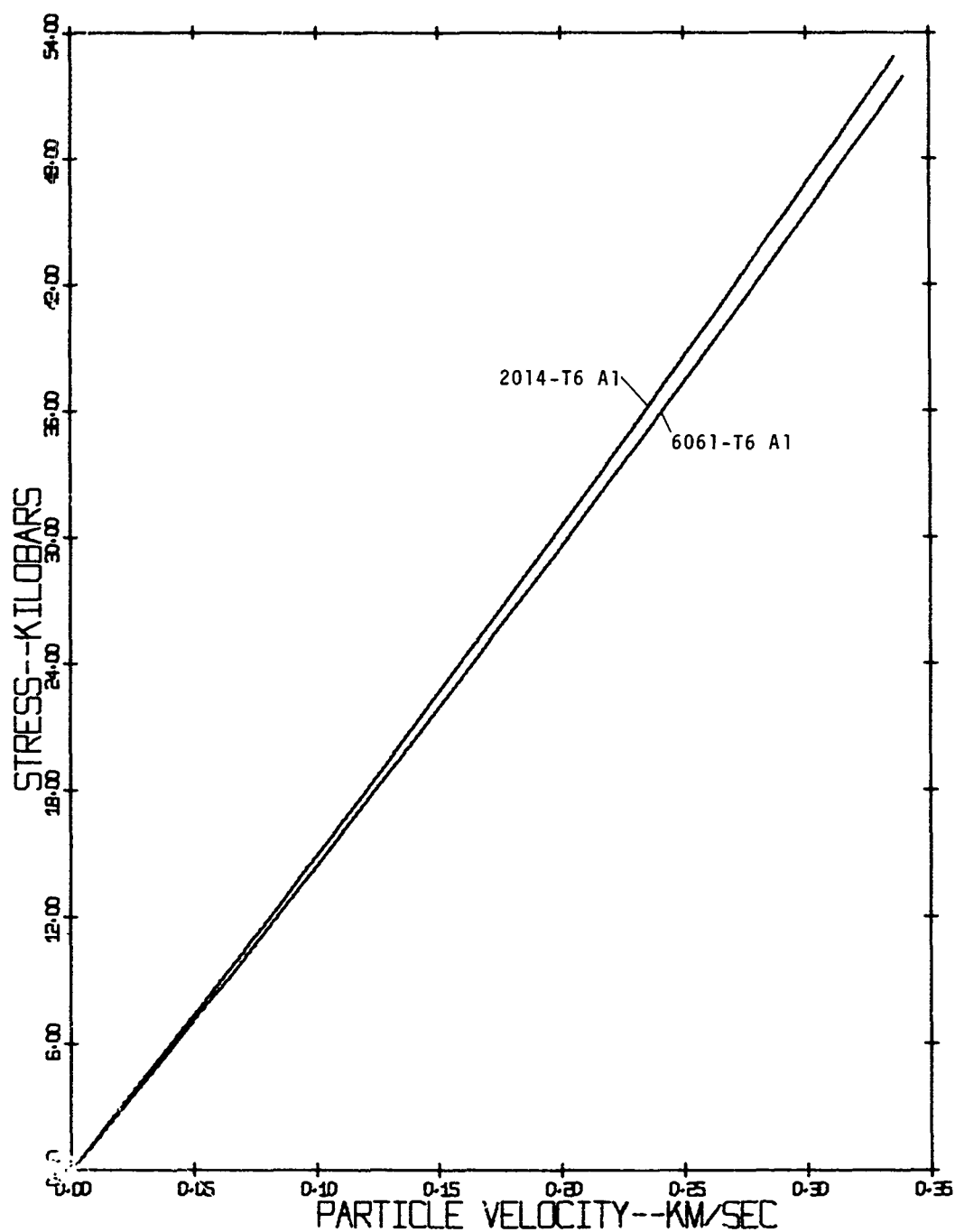


Figure 54 Hugoniot Hydrostats Calculated for 2014-T6 and 6061-T6 Aluminum Using Eqs. (III-19), (III-20), (III-21), and (III-22) (29)

MSL-70-12

## 2. Spall Threshold

Within experimental uncertainty, there is no difference between spallation data obtained by recovery tests on 2014-T6 aluminum and published results on 6061-T6 aluminum (Figure 55). Spallation data available on 6061-T6 aluminum might be used with good accuracy to predict the spallation behavior of 2014-T6 aluminum.

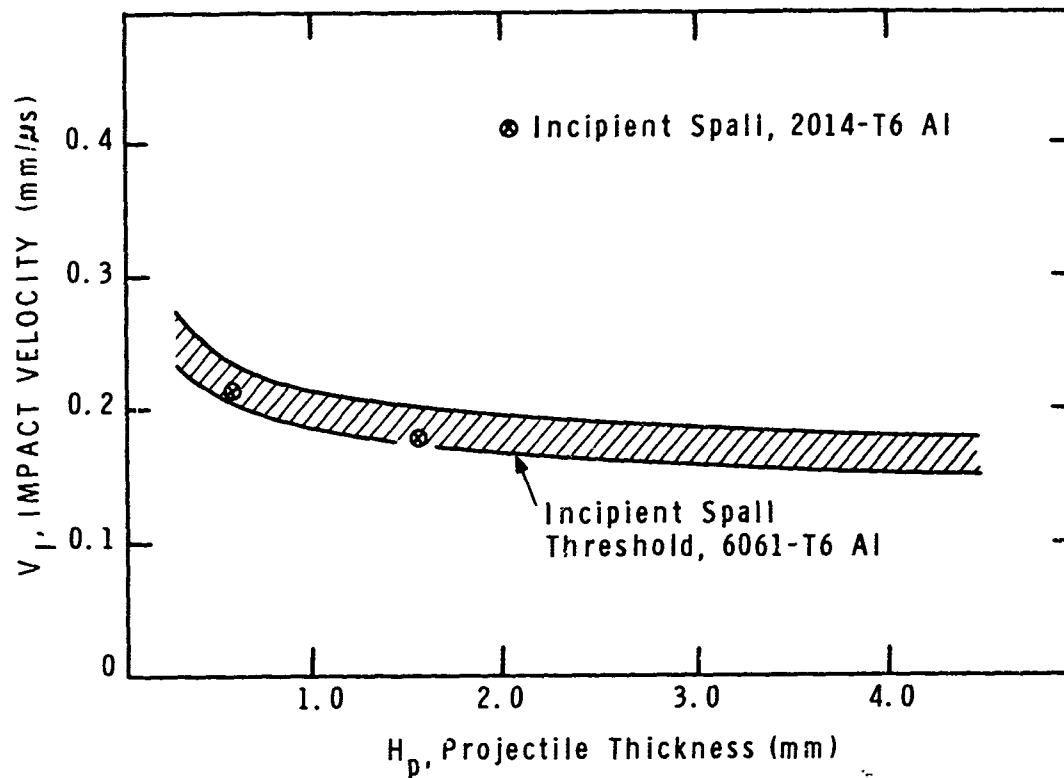


Figure 55 Spallation Threshold Results for 2014-T6 Aluminum Compared to 6061-T6 Aluminum(28)

## 3. Hugoniot

In Figure 56 experimental hugoniots for 2014 and 6061 are compared. The hugoniot for 2014 lies above the hugoniot for

MSL-70-12

6061 by about 4% at 50 kilobars. There is a 3% difference between calculated hugoniots at 50 kilobars (Figure 54). This suggests that part of the difference between experimental hugoniots is due to differences in the elastic constants and density of the two materials. Any difference in precursor amplitude would also contribute to the difference.

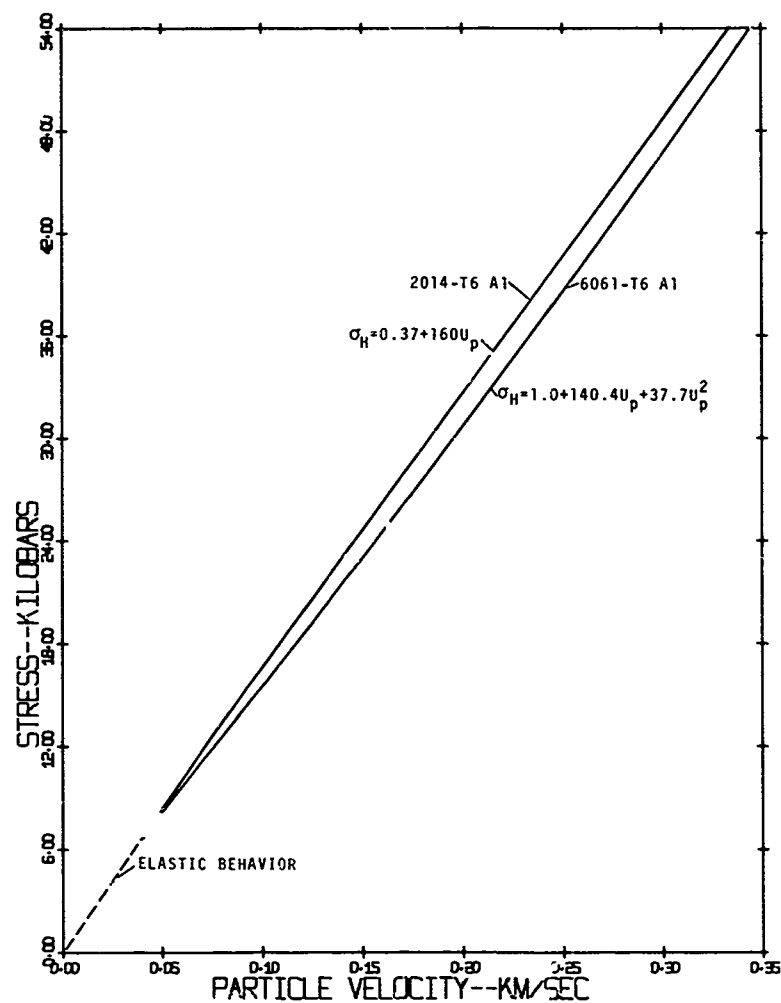


Figure 56 Hugoniot for 2014-T6 Aluminum Compared to Hugoniot for 6061-T6 Aluminum(29)



MSL-70-12

## 4. Elastic Precursor Decay

Elastic precursor decay observed for 2014-T6 aluminum is compared to 6061-T6 aluminum in Table VIII. Values listed for 6061-T6 aluminum represent averages over various plate stocks that have been studied by General Motors Corporation.<sup>(29)</sup> Precursor amplitudes and decay rates agree within the uncertainty of defining  $\sigma_{HEL}$ .

TABLE VIII

COMPARISON OF PRECURSOR AMPLITUDE FOR 2014-T6 AND 6061-T6 ALUMINUM AT  $\sim 20$  KILOBARS IMPACT STRESS<sup>(29)</sup>

Propagation Distance (mm)	Precursor Amplitude	
	2014-T6 Al* (kbar)	6061-T6 Al** (kbar)
$\sim 3$	$6.5 \pm .5$	6.5
$\sim 6.5$	$5.5 \pm .5$	5.5
$\sim 12$	$4.5 \pm .5$	4.5

\* 12.5 mm plate stock.

\*\* Average value from 3.2, 6.4 and 12.5 mm plate stocks.

MSL-70-12

## SECTION IV

### CONCLUSIONS

#### SUBSEQUENT YIELD STUDY

1. The yield surfaces are convex.
2. Cross-effects do exist.
3. There is evidence of a substantial Bauschinger effect.
4. The subsequent yield surface both expands and translates, indicating that the hardening mechanisms are more complicated than both the isotropic and kinematic hardening.
5. The general hardening theory, attributed to Hodge, best describes the subsequent yield behavior of the material.
6. No evidence of corners was found in the study; however from the definition of yield used, corners would not be expected.

#### HEATING RATE STUDY

1. At 500°F, yield and ultimate strength is most sensitive to heating rates between 1.0°F/sec and 0.01°F/second. The heating rate itself does not appear to be important; the time above the artificial aging temperature is most significant.

MSL-70-12

2. The strength at 500°F when heated to temperature in less than 30 minutes (0.25°F/sec) is approximately three times the strength as when 50 hours is required to reach temperature (0.0025°F/second).
3. Above a heating rate of 0.25°F/sec heating rate effects, if any, are lost in the data scatter and the predominant influence on strength is the test temperature.
4. Coalescence of precipitates appears to be the major mechanism influencing the change of material properties with heating rate. Therefore, different precipitation rates would influence the effect of heating rate on aluminum alloys.
5. Little effect on precipitation is observed metallographically at heating rates above 0.25°F/sec (30 minutes to reach 500°F), and the alloy strength appears to be insensitive to time except for the loss due to temperature itself (~ 30% for yield at 500°F).

#### SHOCK WAVE PROPAGATION STUDY

1. The shock wave response of 2014-T6 aluminum is elastic-plastic and nearly identical to that of 6061-T6 aluminum except for a difference between experimental hugoniot (~ 4% at 50 kilobars).
2. The elastic precursor amplitude ranged from 8 kilobars after a propagation distance of 1 mm to 4.5 kilobars after 12 mm.

MSL-70-12

3. The hugoniot for 2014-T6 aluminum may be approximated by

	<u>Stress Range</u>	<u>Accuracy</u>
$\sigma = 179 u$	$0 < \sigma < 8$	$\sim 1\%$
$\sigma = 0.37 + 160 u$	$8 < \sigma < 50$	$\sim 3\%$

where  $\sigma$  is stress in kilobars and  $u$  is particle velocity in mm/ $\mu$ sec.

4. For the Murnaghan equation of state, the hugoniot calculated from elastic constants lies above experimental mean stress hugoniot by  $\sim 3\%$  at 50 kilobars.
5. The spall threshold for 2014-T6 aluminum is dependent upon loading time. Impact velocity (aluminum impactor) necessary for incipient spall decreased from 0.216 mm/ $\mu$ sec for 0.19  $\mu$ sec pulse duration to 0.180 mm/ $\mu$ sec for 0.5  $\mu$ sec pulse duration.
6. For a peak stress of 20 kilobars the compressive wave front becomes steady after a propagation distance of  $\sim 12$  mm. For this same peak stress the release wave is a simple centered rarefaction fan with only slight evidence of elastic-plastic structure.

MSL-70-12

## APPENDIX A

## MATERIAL DESCRIPTION

Three different aluminum alloys were used in this program; 6061-T6 and 2014-T6 aluminum alloys were used for the high heating rate studies (Section II), the same 2014-T6 alloy for the shock wave study (Section III), and 2024-T3 aluminum alloy for the biaxial studies (Section I).

The 6061-T6 material was obtained in the form of 0.25 inch diameter rod. Photomicrographs of the material (Figure A-1) show elongated grains running parallel to the rod axis. The 2024-T3 alloy obtained in the form of 3.0 inch diameter rod, shows a similar structure but with grains more severely elongated (Figure A-2). Both of these materials exhibit little grain size variation across the diameter of the rod.

The 2014-T6, obtained in the form of 0.5 inch thick plate, exhibited non-uniform grain size through the thickness of the plate. The grain size decreased from the plate outer edge to the plate center (see Figure A-3).

Certified chemical composition and heat treatment of the materials are listed in Table A-I.

MSL-70-12

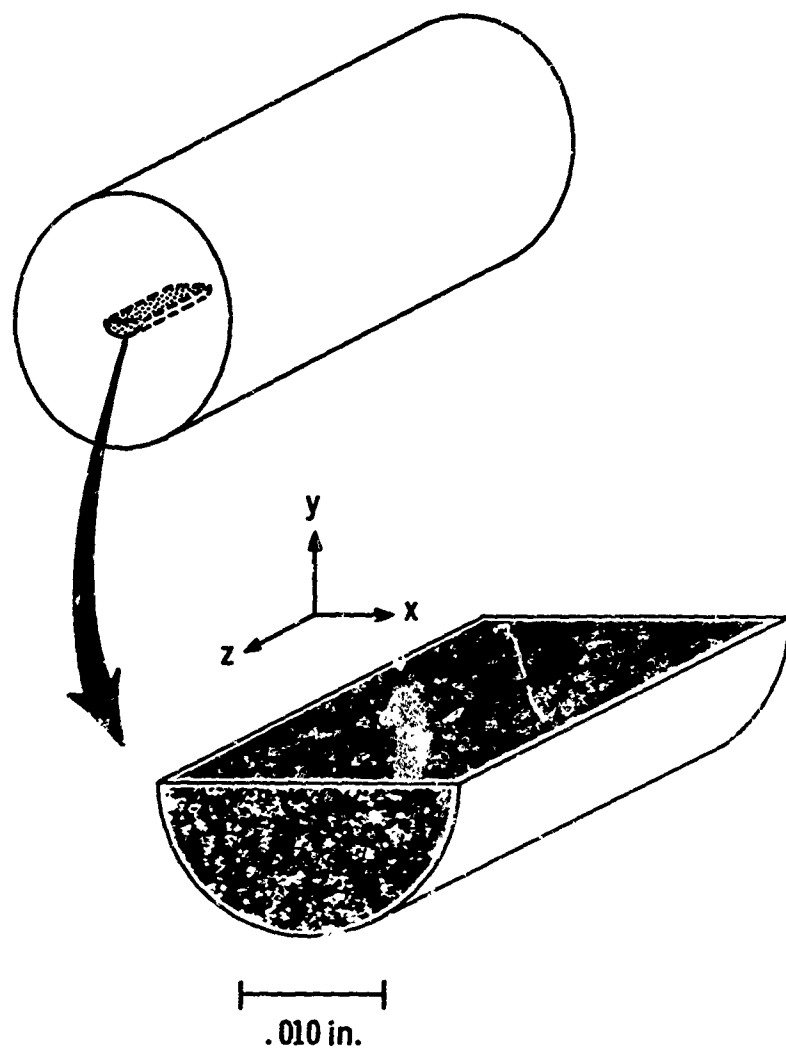


Figure A-1 Photomicrograph of 6061-T651 Aluminum  
0.25 Inch Rod Specimen Material

MSL-70-12

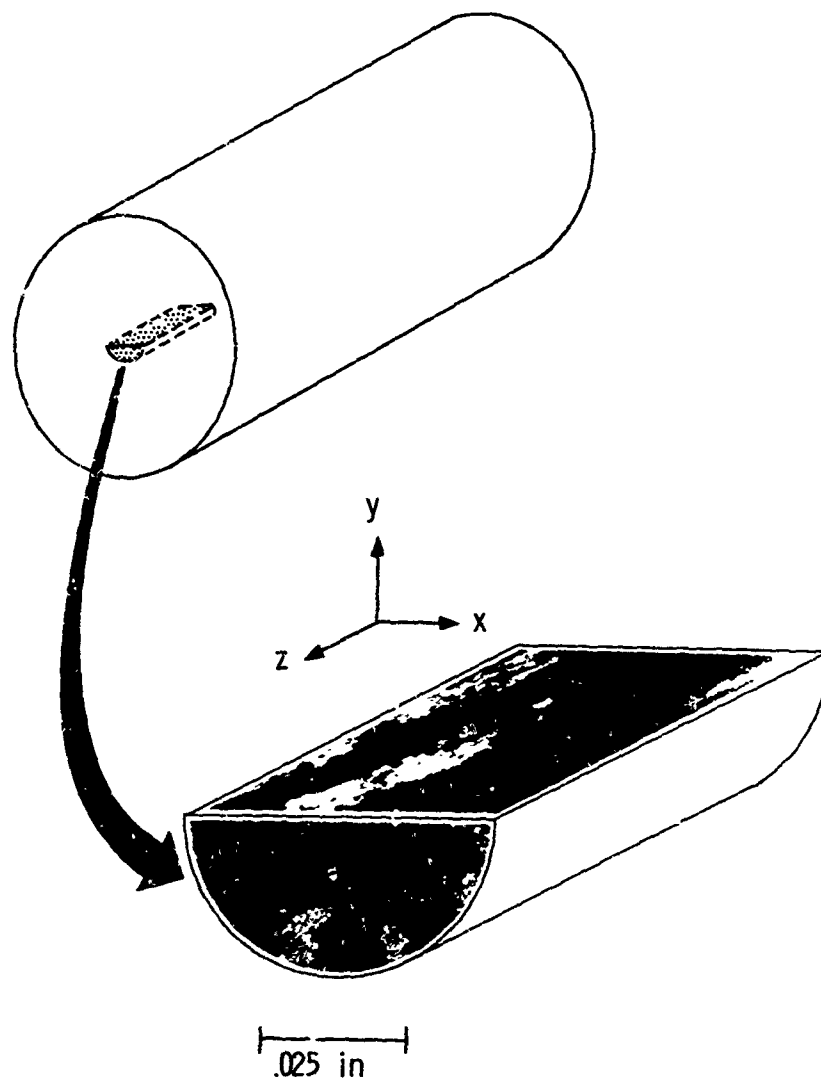


Figure A-2 Photomicrograph of 2024-T351 Aluminum  
3.0 Inch Rod Specimen Material

MSL-70-12

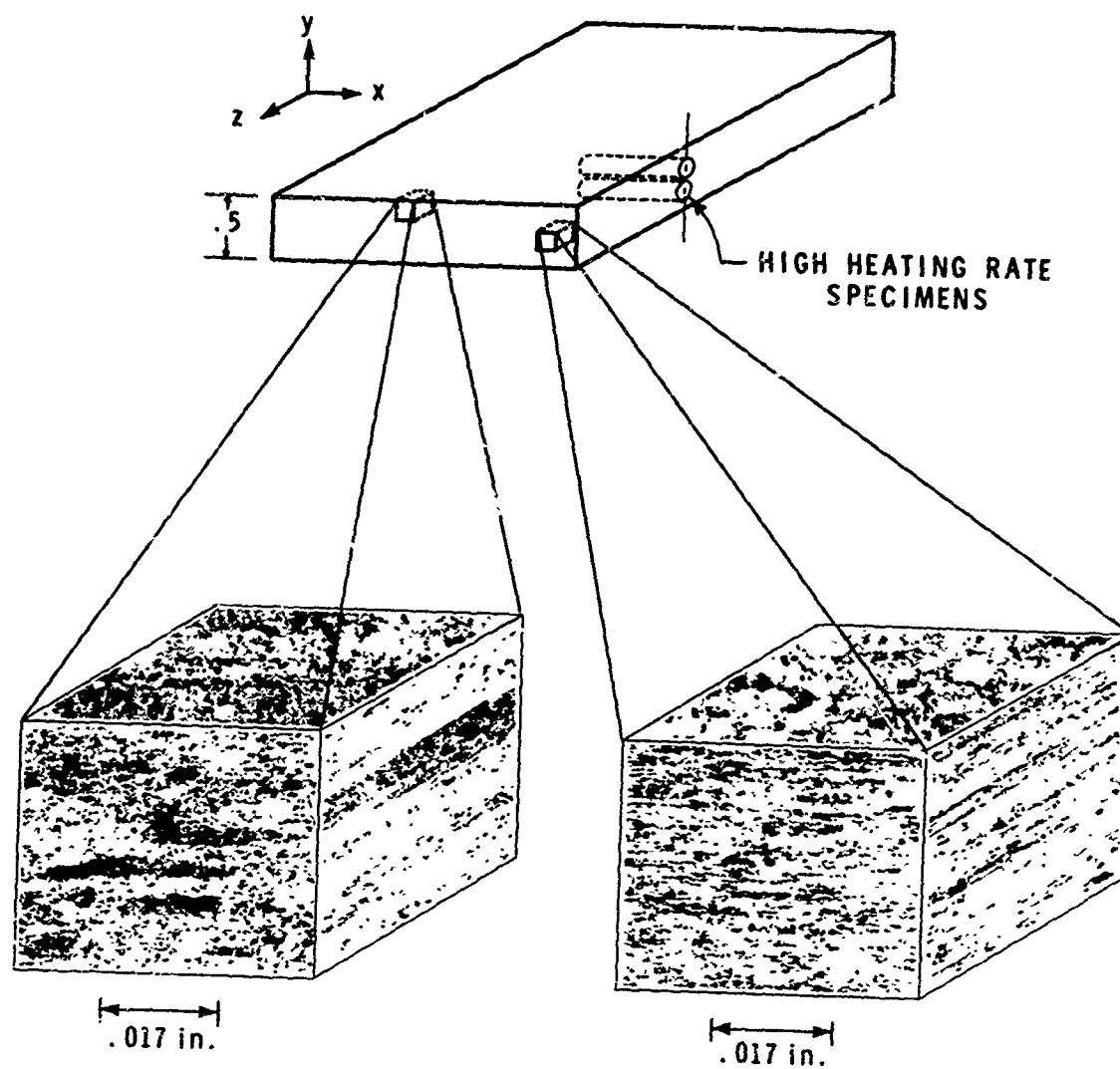


Figure A-3 Photomicrograph of 2014-T651 Aluminum  
0.5 inch Plate Specimen Material



MANUFACTURING DEVELOPMENT • GENERAL MOTORS CORPORATION

MSL-70-1

TABLE A-I  
CHEMICAL COMPOSITION

	6061-T6		2014-T6 (NOMINAL)	2024-T3	
	MIN. (%)	MAX. (%)		MIN. (%)	MAX. (%)
Si	0.4	0.8	0.8		0.50
Fe		0.7			0.50
Cu	0.15	0.40	4.4		4.9
Mn		0.15	0.8	0.3	0.9
Mg	0.8	1.2	0.5	1.2	1.8
Zn		0.25			0.25
Cr	0.15	0.35			0.1
Ti		0.15			
Other (Each)		0.05			0.05
Others (Total)		0.15			0.15
AL	REMAINDER		REMAINDER	REMAINDER	
Heat Treatment	T6-51		T6-51	T3-51	

## REFERENCES

1. Green, S. J., Leasia, J. D., Perkins, R. D. and Maiden, C. J., "Development of Multiaxial Stress High Strain-Rate Techniques", Final Report Material Response Studies, SAMSO TR-68-71, Vol. III, MSL-68-8, Vol. III, January, 1968.
2. Schierloh, F. L., Chaney, R. D. and Green, S. J., "An Application of Acquisition and Reduction of Data of Variable Short Time Tests", to be published in Experimental Mechanics.
3. Perkins, R. D., Jones, A. H., Green, S. J., Leasia, J. D. and Heimbuch, R. A., "Multiaxial Loading Behavior of Four Materials Including ATJ-S Graphite and RAD 6300 Carbon Phenolic", Final Report on Material Response Studies (MARS II) SAMSO, TR-69-393, Vol. I., MSL-69-42, Vol. I, May, 1970.
4. Hsu, T., "The Effect of the Rotation of the Stress Axes on the Yield Criterion of Prestrained Materials", Journal of Basic Engineering, Vol. 88, No. 1, P. 61, March, 1966.
5. Mair, W. M. and Pugh, H. L. D., "Effect of Pre-Strain on Yield Surfaces in Copper", Journal Mechanical Engineering Science, Vol. 6, No. 2, 1964, p. 150-163.
6. Naghdi, P. M., Essenburg, F. and Koff, W., "An Experimental Study of Initial and Subsequent Yield Surfaces in Plasticity", Journal of Applied Mechanics, 1958, Vol. 25, No. 2, p. 201-209.
7. Ivey, H. J., "Plastic Stress-Strain Relations and Yield Surfaces for Aluminum Alloys", Journal Mechanical Engineering Science, Vol. 3, No. 1, 1961, p. 15-31.
8. Szczepinski, W. and Miastkowski, J., "An Experimental Study of the Effect of the Prestraining History on the Yield Surfaces of an Aluminum Alloy", J. Mech. Phys. Solids, 1968, Vol. 16, p. 153-162.
9. Bertsch, P. K. and Findley, W. N., "An Experimental Study of Subsequent Yield Surfaces, Corners, Normality, Bauschinger, and Applied Effects", Proceedings Fourth U.S. National Congress of Applied Mechanics, 1962, Vol. 2, p. 893-907.

MSL-70-12

10. Shiratori, E. and Ikegami, K., "Experimental Study of the Subsequent Yield Surface by Using Cross-Shaped Specimens", J. Mech. Phys. Solids, 1968, Vol. 16, p. 373-394.
11. Babcock, S. G., Kumar, A. and Green, S. J., "Response of Materials to Suddenly Applied Stress Loads, Part I", General Motors Corporation, Defense Research Laboratory, Air Force Flight Dynamics Laboratory, Wright Patterson Air Force Base, Ohio, April, 1967.
12. Babcock, S. G. and Hochstein, P. A., "High Strain Rate Testing of Rapidly Heated Conductive Materials to 7000°F", Experimental Mechanics, Vol. 10, No. 5, February, 1970, p. 78.
13. Babcock, S. G., Hochstein, P. A. and Jacobs, L. J., "High Heating Rate Response of Two Materials From 72°F to 6000°F, Vol. II", Final Report for Air Force, Contract No. F04701-68-C-0161, SAMSO TR-69-393, Vol. II, March, 1970.
14. Frank, E., Electrical Measurement Analysis, McGraw Hill, 1959.
15. "Metals Handbook", Vol. 2, Heat Treating of Non Ferrous Metals, 8th. Edition, American Society for Metals, 1964.
16. "Materials Data Handbook, Aluminum Alloy 6061", Marshall Space Flight Center, TSP 69-10065.
17. Kehl, G. L., "The Principles of Metallographic Laboratory Practice", 3rd. Edition, McGraw Hill, 1949.
18. Brodie, R. N. and Hormuth, J. E., "The PUFF 66 and P PUFF 66 Computer Programs", Air Force Weapons Laboratory, AFWL-TR-66-48, May, 1966, (AD483409).
19. Bertholf, L. D. and Benzley, S. E., "TODDY II - A Computer Programs for Two Dimensional Wave Propagation", Sandia Laboratories, SC-RR-68-41, Nov., 1968.
20. McSkimmin, H. and Andreatch, P., "Analysis of the Pulse Superposition Method for Measuring Ultrasonic Wave Velocities as a Function of Temperature and Pressure", Acoust. Soc. Am. J., Vol. 34, 1962, p. 609-615.
21. Graham, R. A., Neilson, F. W. and Benedick, W. B., "Piezoelectric Current from Shock-Load Quartz --- A Submicro-second Stress Gauge", J. Appl. Phys., Vol. 36, 1965, p. 1775-1783.

22. Barker, L. M. and Hollenbach, R. E., "Interferometer Technique for Measuring the Dynamic Mechanical Properties of Materials", Rev. of Sci. Instr., Vol. 36, 1965, p. 1617-1620.
23. Lysne, P. C., Boade, R. R., Percival, C. M. and Jones, O. E., "Determination of Release Adiabats and Recentered Hugoniot Curves by Shock Reverberation Techniques", J. Appl. Phys., Vol. 40, 1969, p. 3786-3795.
24. Sessler, J. and Weiss, V., Materials Data Handbook, Aluminum Alloy 2014, Sponsored by NASA-Marshall Space Flight Center, Department of Chemical Engineering and Metallurgy, Syracuse University, April, 1966.
25. Chin, H. C., "QZ - A Computer Program to Analyze X-Cut Quartz Data Obtained from Shock Loading", General Motors Corporation, Manufacturing Development, Materials and Structures Laboratory, MSI-70-15, June, 1970.
26. "Data Analysis Methods", General Motors Corporation, Manufacturing Development, Materials and Structures Laboratory, to be published.
27. Taylor, J. W., "Stress Wave Profiles in Several Metals", Dislocation Dynamics, McGraw-Hill, New York, 1968, p. 573-589.
28. Isbell, W. M. and Christman, D. R., "Shock Propagation and Fracture in 6061-T6 Aluminum from Wave Profile Measurements", General Motors Corporation, Manufacturing Development, Materials and Structures Laboratory, MSI-69-60, DASA 2419, April, 1970.
29. Isbell, W. M., Christman, D. R., Babcock, S. G., McMillan, A. R. and Green, S. J., "Measurements of Dynamic Properties of Materials, Vol. III: 6061-T6 Aluminum", General Motors Corporation, Manufacturing Development, Materials and Structures Laboratory, DASA-2501-3, to be published.